University of Helsinki Report Series in Physics

HU-P-D155

Scattering and Refraction as Contrast Mechanisms in X-Ray Imaging

Heikki Suhonen

Laboratory of Electronic Structures
Division of Materials Physics
Department of Physics
Faculty of Science
University of Helsinki
Finland

Academic Dissertation

To be presented with the permission of the Faculty of Science of the University of Helsinki, for public criticism in the Auditorium E204 of the Department of Physics (Physicum), Gustaf Hällströminkatu 2a, on October 31st, 2008, at 12 o'clock noon

Helsinki 2008

Supervised by:

Prof. Pekka Suortti
Department of Physics
University of Helsinki
Finland

Prof. Ritva Serimaa
Department of Physics
University of Helsinki
Finland

Reviewed by:

Prof. Rob Lewis
Monash Center for Synchrotron Science
Monash University
Victoria, Australia

Prof. Jussi Timonen
Department of Physics
University of Jyväskylä
Finland

Opponent:

Prof. Franz Pfeiffer
École Polytechnique Fédéral de Lausanne
Switzerland

Report Series in Physics HU-P-D155
ISSN 0356-0961
ISBN 978-952-10-3938-6
ISBN 978-952-10-3939-3 (pdf version)
http://www.ethesis.helsinki.fi
Helsinki 2008
Helsinki University Print

Preface

This work is a part of an ongoing collaboration between the Department of Physics at University of Helsinki, Helsinki University Central Hospital, and ESRF, to utilize x-ray scattering and refraction for the detection of lesions in mammographic examinations of the breast. I've had the opportunity to work in an interesting, international research group, with some of the best experts in the field. This work was funded by the Academy of Finland.

This work would not have been possible without the contributions of many individuals. First, I would like to express my thanks to my supervisor Professor Pekka Suortti. He initially offered me the possibility to work in the interesting field of x-ray imaging, and gave me support, focus, and ideas in my work, while letting me have also a lot of freedom. I would like to thank my other supervisor, Professor Ritva Serimaa, for the encouragement in my work, as well as making sure that I had a steady place to work at the x-ray laboratory.

I would like to thank the official reviewers of this work, professors Rob Lewis and Jussi Timonen, for taking the time to thoroughly examine my work, and giving valuable input in the finalization stages of the work.

Big part of this work is based on measurements that were done in co-operation with, or entirely by other people, and would have been unachievable for just me alone. Therefore I would like to thank everyone involved in the so called 'Helsinki-Grenoble collaboration' that made it possible to bring the breast tissue samples from Helsinki to ESRF to be measured. Especially I express my gratitude to Drs. Jani Keyriläinen and Manuel Fernández for their expert work on the experimental characterization of the scattering and refraction properties of the tissue samples. Without your excellent work, I would not have had any basis on which to build my work.

Apart from this thesis my work has involved functional lung imaging studies. I would like to give big thanks to the 'Broncho Team'. Especially I would like to thank Liisa, Sam and Satu for the fun and interesting times at the beamline. I would like to thank also the colleagues at the x-ray lab for nice working atmosphere and the floorball games.

Finally I'd like to thank all my friends and my family.

Helsinki, September 2008

H. Suhonen: Scattering and Refraction as Contrast Mechanisms in X-Ray Imaging. University of Helsinki, 105 pages, *Report Series in Physics* HU-P-D155.

Abstract

Differentiation of various types of soft tissues is of high importance in medical imaging, because changes in soft tissue structure are often associated with pathologies, such as cancer. However, the densities of different soft tissues may be very similar, making it difficult to distinguish them in absorption images. This is especially true when the consideration of patient dose limits the available signal-to-noise ratio. Refraction is more sensitive than absorption to changes in the density, and small angle x-ray scattering on the other hand contains information about the macromolecular structure of the tissues. Both of these can be used as potential sources of contrast when soft tissues are imaged, but little is known about the visibility of the signals in realistic imaging situations. In this work the visibility of small-angle scattering and refraction in the context of medical imaging has been studied using computational methods.

The work focuses on the study of analyzer based imaging, where the information about the sample is recorded in the rocking curve of the analyzer crystal. Computational phantoms based on simple geometrical shapes with differing material properties are used. The objects have realistic dimensions and attenuation properties that could be encountered in real imaging situations. The scattering properties mimic various features of measured small-angle scattering curves. Ray-tracing methods are used to calculate the refraction and attenuation of the beam, and a scattering halo is accumulated, including the effect of multiple scattering. The changes in the shape of the rocking curve are analyzed with different methods, including diffraction enhanced imaging (DEI), extended DEI (E-DEI) and multiple image radiography (MIR). A wide angle DEI, called W-DEI, is introduced and its performance is compared with that of the established methods.

The results indicate that the differences in scattered intensities from healthy and malignant breast tissues are distinguishable to some extent with reasonable dose. Especially the fraction of total scattering has large enough differences that it can serve as a useful source of contrast. The peaks related to the macromolecular structure come to angles that are rather large, and have intensities that are only a small fraction of the total scattered intensity. It is found that such peaks seem to have only limited usefulness in medical imaging. It is also found that W-DEI performs rather well when most of the intensity remains in the direct beam, indicating that dark field imaging methods may produce the best results when scattering is weak. Altogether,

it is found that the analysis of scattered intensity is a viable option even in medical imaging where the patient dose is the limiting factor.

Classification (INSPEC): A4215D, A6110D, A8770E, C7320

Keywords: Analyzer based imaging, x-rays, signal-to-noise ratio, scattering, refraction, geometrical optics, ray-tracing

Contents

Abbreviations and Symbols

ABI	Analyzer Based Imaging
BM	Bending Magnet
CAT, CT	Computed Tomography
CCD	Charge-Coupled Device
DEI	Diffraction Enhanced Imaging
DQE	Detective Quantum Efficiency
E-DEI	Extended DEI, to analyze central peak broadening
ESRF	European Synchrotron Radiation Facility
FReLoN	Fast Readout Low Noise, A CCD-based 2-D detector at ESRF
FWHM	Full width at half maximum
MC	Monte Carlo
MIR	Multiple Image Radiography
PMMA	Poly(methyl methacrylate) (acrylic glass)
PSF	Point Spread Function
pV	pseudo-Voigtian
RC	Rocking curve of the analyzer
SNR	Signal to Noise Ratio
USAXS, SAXS	(Ultra) Small Angle X-ray Scattering
W-DEI	Wide angle DEI
$F(\theta_x, \theta_z)$	Scattering function
γ_{W}	Wide angle scattering paremeter from W-DEI
θ_{R}	Rocking angle of the analyzer
ξ	Fraction of the direct beam

Chapter 1

Introduction

1.1 Problem Setting and Scope

In addition to attenuation, x-rays undergo refraction and scattering when passing through a medium. Imaging methods based on these two phenomena show promise especially in medical imaging, where significant improvements of contrast to dose ratio have been demonstrated for *in vitro* samples [1–4]. The interpretation of refraction and scattering images, however, is more complicated when compared to the rather straightforward interpretation of attenuation images. Refraction and scattering are not as easily observed as attenuation, and this places rather stringent requirements on the instrumentation. In this work we study via numerical calculations the visibility of scattering and refraction in imaging.

Especially mammography may benefit from contrast improvement due to refraction, because the density variations within the soft connective tissue are rather small [5]. Furthermore, normal mammograms cannot in many cases distinguish between benign and malignant lesions, leading to high rate of unnecessary biopsies. The scattering signal from breast tissue samples has been shown to be sensitive to changes in breast tissue due to breast cancer [6]. If this signal could be utilized in imaging, the images would allow a higher rate of detection and a lower number of unnecessary biopsies. This work is a continuation of the studies on breast tissue samples [5, 6], with the aim of understanding how well the scattering signal from breast tissue samples is visible in the images.

1.2 X-Rays in Medical Imaging

Medical imaging based on tissue dependent differences in x-ray attenuation has been utilized almost ever since Wilhelm Röntgen discovered the x-rays in 1895 [7]. Medical imaging has contributed greatly to the success of modern medicine by allowing internal parts of the human body to be observed.

This has facilitated better treatment of fractures and earlier detection of many pathological conditions, and thus contributed greatly to the increasing overall quality of life. Essentially the same, century old x-ray imaging methods are still in routine use in hospitals around the world.

An important improvement to the x-ray imaging method is the computed axial tomography (CAT or CT) [8]. Instead of taking a single projection image of the patient, several projections from different angles are taken and a three-dimensional image (or a two-dimensional slice) can be reconstructed using methods based on the inverse radon transform [9]. CT is used to study in detail anatomical structures, and for example to accurately localize tumours. The use of CT increases the patient dose compared to a single projection image, and this means that in many cases a single projection image is still preferable [10].

X-ray absorption is not always sensitive enough to facilitate the differentiation of tissue types whose absorption and density are close to each other. In some cases contrast agents can be introduced to the tissue of interest to differentiate it from the surroundings. Injection of iodine or gadolinium to the blood circulation in angiography is used routinely in clinical practice [11]. Studies of using iodine to enhance the sensitivity of mammography have also been carried out [12]. Yet another application under research is the use of inhaled xenon as a contrast agent in functional studies of the lung [13, 14].

Besides x-rays, several other physical phenomena are routinely utilized in medical imaging. For example, magnetic resonance imaging (MRI) is based on nuclear magnetic resonance and offers contrast based on the local chemical environment of hydrogen atoms. Positron emission tomography (PET) is based on injection of positron emitting contrast agent. The positrons annihilate locally with electrons, and the contrast agent distribution can be three dimensionally quantified by detecting the annihilation photons. Ultrasound measurements based on speed of sound and reflection from interfaces can measure mechanical properties of tissues. The existence of different methods verifies that none of the methods is suitable for all situations, and the development of new methods continues on all fronts.

1.3 X-Ray Scattering and Refraction

The most common interactions between x-rays and material are absorption and scattering (either elastic or inelastic). Absorption gives rise to fluorescence that spreads out equally in all directions and whose energy distribution depends on the chemical composition of the sample. Inelastic scattering has a nonuniform distribution whose intensity does not appreciably depend on the sample structure. Elastic scattering produces several types of interference phenomena, depending on the atomic and molecular structure of the sample, one of them being refraction. Monochromatic and collimated in-

coming radiation is thus spread out in angular and energy ranges due to the interactions, as illustrated in figure 1.1.

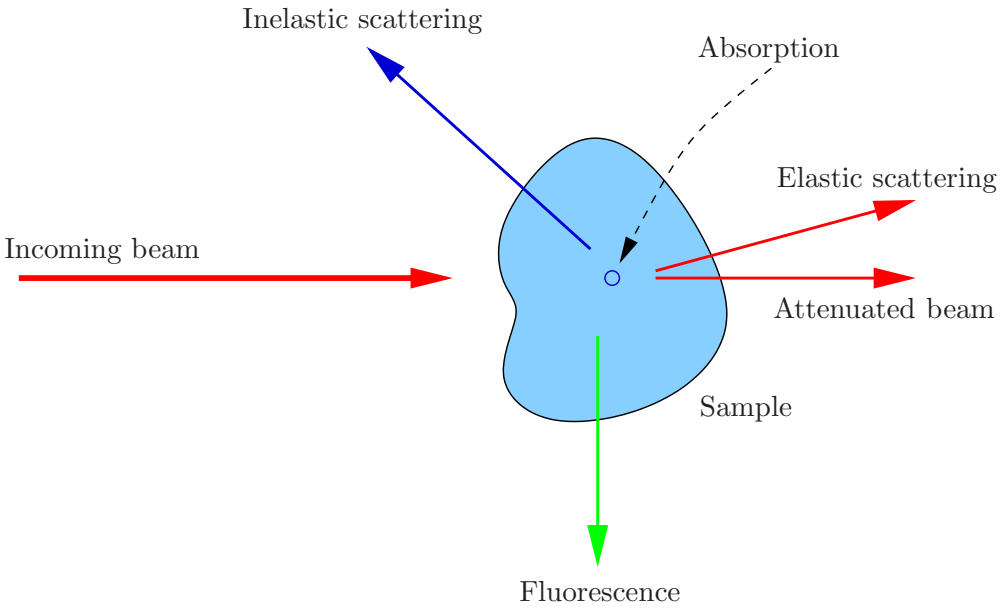

Figure 1.1: A schematic presentation of x-ray interactions.

Scattering and fluorescence are a nuisance in attenuation based imaging, since they do not contribute to the attenuation signal, but instead produce a background on the detector, which acts to reduce the visibility of details in the images. However, it is seen in dedicated scattering and fluorescence experiments that these signals contain a wealth of information about the sample. These are utilized to obtain further information of the sample, that is not available in plain attenuation images.

Several imaging methods have been developed for capturing the information contained in scattering and refraction. We concentrate in this work on the method that uses two perfect crystals for highly accurate analysis of the angular distribution of the radiation coming from the sample. This method, analyzer based imaging (ABI), is sensitive to angular changes smaller than one microradian, and is able to provide good contrast due to refraction and scattering. We simulate computationally the intensity distribution coming from the sample, including the effects of refraction and scattering, and study how these effects are visible when the intensity is recorded with the two crystal setup used in ABI.

1.4 Purpose of the Study

The motivation and background for this work comes from earlier x-ray scattering measurements [6] and analyzer based x-ray imaging experiments [5] on breast tissue samples containing breast cancer. This study is a continuation of the previous studies with the purpose of finding out more about how scattering signal could be used as a potential source of contrast in imaging.

Specifically, the purpose is to quantify how the features of the scattering patterns coming from the sample are visible in the rocking curves measured in analyzer based imaging. To this end we quantify the features of scattering patterns from tissue samples with breast cancer to see what are the typical angular ranges where the scattered signal appears, how strong the scattering can be expected to be, and how large changes in the scattering patterns can be expected (e.g. due to progression of cancer). This allows us to estimate what are the interesting angular ranges to use in analyzer based imaging, and how high a dose of incoming radiation is required in order to get sufficient counting statistics for the recorded signal.

To establish the relationship between the object visibility and the dose, we developed a simulation program based on the ray tracing method, which in addition takes into account the effects of scattering. The program calculates images simulating the analyzer based imaging setup, so that the rocking curves for different objects can be obtained. In addition the dose in the sample is calculated, giving the possibility of evaluating the visibility of objects at a given dose.

Chapter 2

X-Ray Physics and Instrumentation

2.1 Properties of X-Rays

2.1.1 Definitions and Basic Properties

X-rays are part of the electromagnetic spectrum covering the energy range from several hundred eV to a few hundred keV[a]. The wave characteristics of x-rays explain most of the observed phenomena (i.e. elastic scattering, diffraction, refraction and absorption) [15]. Explanation of inelastic scattering, however, requires that x-rays be treated as particles, i.e. photons [16]. A photon has energy $E = hf$ and momentum $p = E/c$, where $h = 6.626 \cdot 10^{-34}\,\mathrm{J \cdot s}$ is the Planck constant and $c = 299792458\,\mathrm{m/s}$ is the speed of light in vacuum.

The wavelength λ of x-rays as a function of energy E can be expressed in practical units as

$$\lambda[\mathrm{nm}] = \frac{1.24\,\mathrm{nm}}{E[\mathrm{keV}]}. \tag{2.1}$$

The frequency $f = \omega/(2\pi)$ can be correspondingly expressed as

$$f[\mathrm{Hz}] = E[\mathrm{keV}] \cdot 2.4 \cdot 10^{17}\,\mathrm{Hz}. \tag{2.2}$$

X-ray frequencies are extremely high and the magnitude of the electric field cannot be measured fast enough to reconstruct the complete signal. Equation (2.1) indicates also that interferometric techniques require a precision of the order of atomic distances.

Intensity quantifies the amount of energy arriving at a unit area in unit time. It is defined as power / area and in SI-units has the dimensions of

[a] There is no exact definition for the energies of x-rays, but usually a distinction is made between x-rays coming from electronic processes and gamma-rays coming from nuclear processes.

$\mathrm{W/m^2}$. If a source with power P emits radiation uniformly into a solid angle of α, the intensity at distance R from the source is

$$I = \frac{P}{\alpha R^2}. \tag{2.3}$$

The intensity can also be interpreted in terms of the number of photons. Let $n(E)\mathrm{d}E$ be the number of photons in the energy range $[E, E + \mathrm{d}E[$ passing through a unit area in unit time. The intensity is then

$$I = \int_{E=0}^{\infty} E\, n(E)\mathrm{d}E. \tag{2.4}$$

Especially for an almost monochromatic beam of energy E_0 and N photons per unit time, the intensity is

$$I = E_0 N. \tag{2.5}$$

In this case the number of photons can be given in practical units as a function of the intensity and beam energy,

$$N[\mathrm{phot./s/m^2}] = \frac{I[\mathrm{W/m^2}]}{E_0[\mathrm{keV}]} \cdot 6.24 \cdot 10^{15}. \tag{2.6}$$

The number of photons is important, because it sets the limit for how well small intensities can be detected from the point of view of counting statistics.

Intensity is only a partial representation of the electromagnetic wave, the phase $\phi(\mathbf{r})$ being equally important. The amplitude of the wave is

$$A(\mathbf{r}) = \sqrt{I(\mathbf{r})}\exp[-i\phi(\mathbf{r})]. \tag{2.7}$$

The phase relationships between different waves lead to interference, and the detection of changes in $\phi(\mathbf{r})$ allows phase contrast imaging.

2.1.2 Coherence

Coherence is the property of electromagnetic radiation that describes its ability to form interference patterns. No radiation field is completely coherent or completely incoherent, but the fields exhibit a varying level of partial coherence. Coherence is set by the properties of the source and the optical elements. For example, the light from a laser has a high level of coherence, whereas that from a light bulb is highly incoherent. By using careful collimation and monochromatization, the coherence level of light from a light bulb can be increased, but only at the expense of losing intensity. X-ray scattering, diffraction and refraction are based on interference, and therefore the coherence properties of the incoming x-rays have an effect on what the observed intensity looks like.

There are several types of coherence. In practice coherence is usually taken to mean first order coherence which describes how well the oscillations at certain location at two different times are correlated (temporal coherence) or how the oscillations at two different locations at a given moment are correlated (lateral coherence). Second order coherence describes how different wave packets relate to each other. Phenomena related to the second order coherence cannot in practice be observed with x-rays [17]. Therefore we limit our discussion to first order coherence, which has some practical applications in the x-ray regime as well.

Temporal (or longitudinal) coherence deals with how large path differences for the wave packet still produce observable interference. Every wave packet has a finite energy spread, and this means to that they have also a finite length. If the wave packet from the source takes two different routes to the detector (see figure 2.1), interference effects can only be observed if the path difference of these routes is smaller than the longitudinal coherence length $l_l = \lambda_0^2/\Delta\lambda$ [18, pp. 325–359]. For longer path differences interference occurs only between different wave packets, but these average to zero because time delays between wave packets are random.

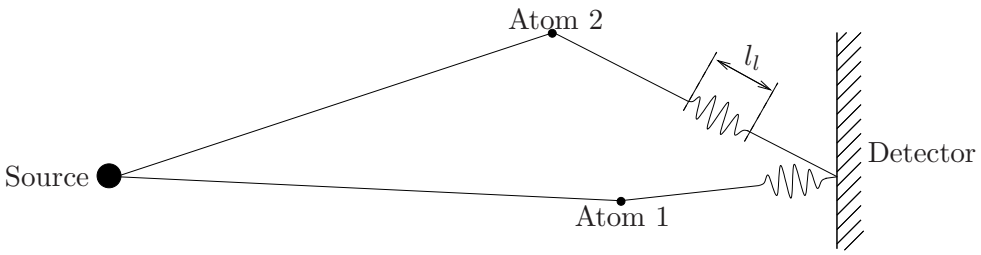

Figure 2.1: A wave packet goes to the detector via two different routes. There is no interference if the path length difference exceeds the longitudinal coherence length l_l.

Transverse (or lateral) coherence depends on the source size. For a point source, the amplitudes at any two locations are correlated, and the coherence is perfect. For an incoherent source of non-zero size, each point in the source emits radiation independently of the others, and the level of coherence of the radiation field drops as the angular size of the source increases [19]. The transverse coherence length is $l_t = \lambda L_0/d$ [20], where L_0 is the distance from the source, and d the width of the source.

In practice for 50 keV x-ray radiation, monochromatized with Si 333 reflection, $\Delta\lambda/\lambda \approx 10^{-5}$ and $\lambda = 0.0248\,\text{nm}$. Therefore $l_l \approx 2\,\mu\text{m}$. For a typical synchrotron radiation source $L_0 \approx 100\,\text{m}$ and $d \approx 100\,\mu\text{m}$ (cf. table 2.2), and therefore $l_t \approx 25\,\mu\text{m}$.

2.2 Interaction of X-Rays with Matter

There are many types of interaction mechanisms, such as absorption and scattering, by which x-rays interact with matter. The interactions are stochastic in nature and their probabilities are described by interaction cross sections, denoted with σ (cm^2/g). Cross sections for free carbon atoms for the most common interaction processes are shown in figure 2.2. In the energy range below 100 keV the most important interaction mechanisms are elastic and inelastic scattering and photoelectric absorption. The cross sections for different processes can be summed to get the total cross section

$$\sigma_{\text{total}} = \sigma_{\text{elastic}} + \sigma_{\text{inelastic}} + \sigma_{\text{photoelectric}}. \tag{2.8}$$

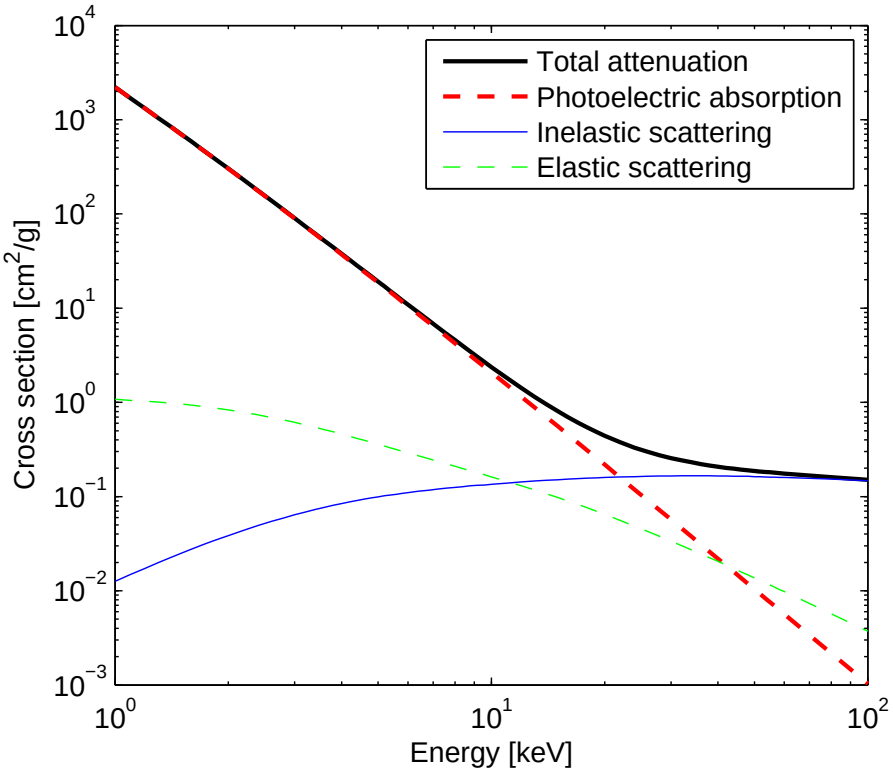

Figure 2.2: Photon cross sections for free carbon atoms as a function of energy [21].

The interpretation of cross sections is that the probability of interactions within a thin layer (thickness Δx) of material with density ρ is

$$\mathrm{d}P = \rho\sigma\Delta x. \tag{2.9}$$

From the basic properties of probability theory we find that, for a sample with thickness L, the probability of not having any interactions is

$$P\{\text{no interactions}\} = \lim_{\Delta x \to 0}(1 - \rho\sigma\Delta x)^{L/\Delta x} = \exp[-\rho\sigma L]. \tag{2.10}$$

This result is useful when simulating the interactions via a Monte-Carlo method.

Cross sections are usually measured and tabulated for free atoms [22], and to an extent cross sections are independent of the atomic arrangement. The elastic scattering cross section, however depends heavily on the particular structure in question. Other cross sections depend slightly on the neighbourhood, and can be used as probes of the surrounding of an atom, such as in x-ray absorption fine structure studies [23]. Assuming independence of the atomic structure, cross sections for a mixture or a compound can be calculated by adding the individual cross sections (σ_i) weighted by the weight fractions (w_i) of the constituents,

$$\sigma = \sum_i \sigma_i w_i. \tag{2.11}$$

Cross sections change as the energy of the photons increases. When the energy crosses an absorption edge, i.e. the energy corresponding to a binding energy of some atomic electron, the electron in question can be ionized, and the changes in the cross sections can be quite dramatic. These changes can be utilized e.g. in anomalous scattering experiments [24, 25] or in k-edge subtraction imaging [26]. In imaging, rather high x-ray energies are used ($\sim 50\,\text{keV}$) to minimize the absorbed dose, and the energy is usually much above any of the absorption edges of the elements found in the biological samples. Therefore phenomena related to absorption edges can only be utilized with the help of contrast enhancing agents.

2.2.1 Attenuation and Absorption

Attenuation of x-rays is measured by aiming a narrow beam at a material, and recording the transmitted intensity in a way that the scattered photons are completely rejected [27]. There are two factors that contribute to attenuation. Part of the x-ray energy is absorbed in the material and part of the energy is scattered away from the narrow beam that goes to the detector [28]. Figure 2.2 shows the relative importance of photoelectric absorption and inelastic scattering. The elastic scattering contribution to the attenuation can vary greatly depending on the atomic structure (e.g. complete attenuation by reflection from a perfect crystal).

Attenuation is described by mass attenuation coefficient μ/ρ, (cm^2/g). This relates the incoming intensity I_0 and outgoing intensity I by

$$I(t) = I_0 \exp\left[-\left(\frac{\mu}{\rho}\right)\rho t\right], \tag{2.12}$$

where ρ is the density of the sample, and t is its thickness. For materials with heterogeneous composition the attenuation coefficient and density may vary throughout the sample. In this case the transmitted intensity is

$$I(t) = I_0 \exp\left[-\int_{x=0}^{t} \mu(x)\mathrm{d}x\right], \tag{2.13}$$

where $\mu(x)$ is the linear attenuation coefficient at location x.

The quantity $\mu = (\mu/\rho)\rho$ is known as the linear attenuation coefficient. A useful quantity in comparing the attenuation properties of different materials is the half layer thickness $t_{1/2}$ for which $I(t_{1/2})/I_0 = 1/2$, i.e. $t_{1/2} = \ln(2)/\mu$. Table 2.1 shows half layer thicknesses for some materials of interest in medical imaging at different energies. Higher energies are transmitted better, and are thus more amenable to imaging applications, but the relative differences between the materials diminish as the energy is increased, so that there is always a compromise to be made about the energy used.

Energy / (keV)	10.00	30.00	50.00	70.00	90.00
Air	112.35	1625.85	2765.51	3272.65	3601.93
Blood	0.12	1.70	2.87	3.39	3.72
Bone	0.01	0.27	0.85	1.38	1.78
Brain	0.12	1.75	2.93	3.45	3.78
Breast tissue	0.16	2.00	3.11	3.58	3.90
Muscle	0.12	1.75	2.92	3.43	3.77
Soft tissue	0.12	1.73	2.89	3.40	3.73
Water	0.13	1.85	3.05	3.58	3.92

Table 2.1: Half thicknesses of attenuation (in cm) for various materials of interest [29]

The mass energy absorption coefficient $(\mu/\rho)_{\mathrm{en}}$ describes how much of the beam energy is absorbed in the sample

$$E_{\mathrm{abs}} = E_0(1 - \exp\left[-\left(\frac{\mu}{\rho}\right)_{\mathrm{en}}\rho t\right]). \tag{2.14}$$

Here E_{abs} is the total absorbed energy and E_0 is total amount of energy contained within the incoming beam. Similarly to attenuation, the linear absorption coefficient is defined as $\mu_{\mathrm{en}} = (\mu/\rho)_{\mathrm{en}}\rho$. Both photoelectric absorption and inelastic scattering contribute to the absorption, however attenuation is always a bit larger than energy absorption, as can be seen in figure 2.3. For energies above 10 keV the attenuation can be considerably higher than absorption due to the increased contribution of inelastic scattering.

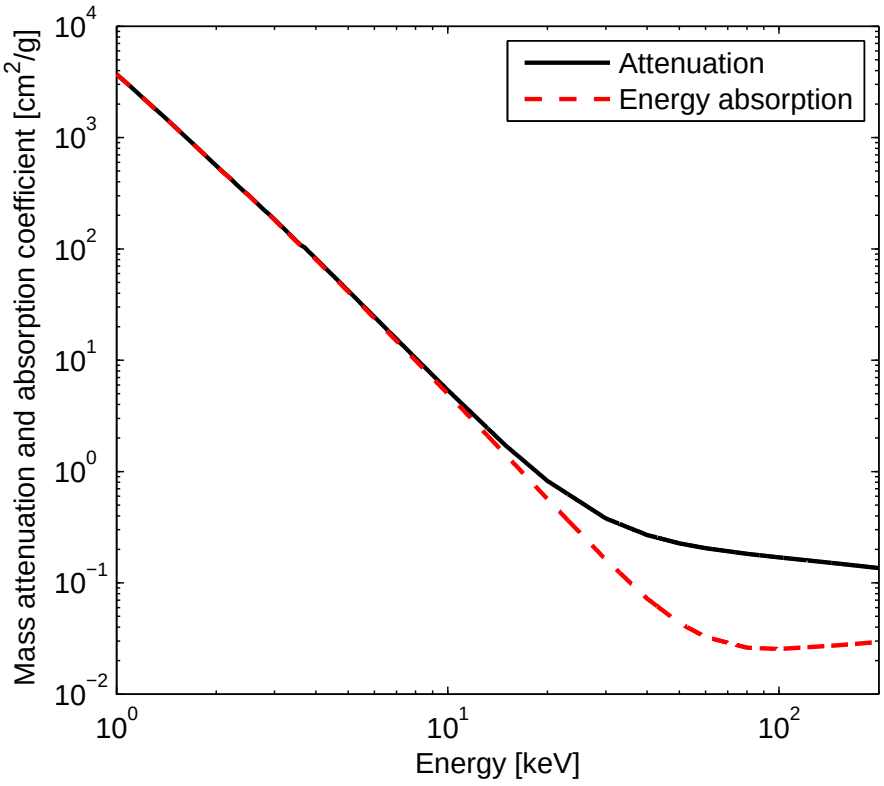

Figure 2.3: Mass energy absorption and mass attenuation coefficients for soft tissue [29].

2.2.2 Elastic Scattering

X-rays scatter mainly from electrons in the material. The differential scattering cross section for a free electron is [30, pp. 9-11]

$$\frac{\mathrm{d}\sigma}{\mathrm{d}\Omega} = \left(\frac{\mu}{4\pi}\frac{e^2}{m_e}\right)^2 \cdot (k_\perp + k_\parallel \cos 2\theta) = r_e^2(k_\perp + k_\parallel \cos 2\theta) \tag{2.15}$$

which expresses the probability of scattering into a unit solid angle. Here $r_e = 2.818\times10^{-15}$ m is the classical electron radius, μ the magnetic constant, m_e the electron mass, e the electron charge, and 2θ the scattering angle. The polarization state is generally described by the Stokes parameters [18, pp. 630–632], but in scattering from free electrons the phase relation between the two polarization components has no effect, and therefore $k_\parallel$ and $k_\perp$ (fractions of the incoming radiation with polarization in and perpendicular to the plane of scattering, respectively) suffice in describing the effect of polarization.

A note on the units convention is in order. The interpretation of $\mathrm{d}\sigma/\mathrm{d}\Omega$ is

$$\frac{\mathrm{d}\sigma}{\mathrm{d}\Omega} = \frac{\text{photons / unit time / unit solid angle}}{\text{incoming photons / unit time / unit area}},$$

so that the differential scattering cross section gives the probability of scattering into a given angle. The scattered intensities are therefore also usually expressed in power / unit solid angle, rather than power / unit area, which is the conventional unit of intensity. This is a natural convention for scattering problems because it eliminates the dependence of intensities on the distance between the sample and the detector.

Electrons in atoms form a charge distribution $\rho(\mathbf{r})$ that is of finite size, and the waves scattered from different parts of the atom interfere. Interference means that the amplitudes scattered from different points of the atom are summed taking the phase differences into account. The phase differences arise from the fact that the waves have to travel different distances when they scatter from different locations within the atom. A common way to deal with phase differences is to use wave vectors $\mathbf{s}_1$ and $\mathbf{s}_2$ for the incoming and scattered waves, respectively. Then the scattering vector is $\mathbf{s} = \mathbf{s}_2 - \mathbf{s}_1$, and its length[b] is $s = |\mathbf{s}| = 2\sin(\theta)/\lambda$, as shown in figure 2.4. The phase difference between two waves originating from points $\mathbf{r}_1$ and $\mathbf{r}_2$ is then $\Delta\phi = 2\pi\mathbf{s}\cdot(\mathbf{r}_1 - \mathbf{r}_2)$ [30]. The amplitude scattered from the atom, atomic scattering factor, in units of electron scattering is then [30, p. 15]

$$f_0(\mathbf{s}) = \int \rho(\mathbf{r}) \exp[-i2\pi\mathbf{s}\cdot\mathbf{r}]\mathrm{d}\mathbf{r}. \tag{2.16}$$

[b] The definition of the length as well as the notation for the scattering vector varies in the literature. Notations $\mathbf{q}$ and $\mathbf{k}$ are commonly used in the literature, and a common alternative to the length is $k = 4\pi\sin(\theta)/\lambda$

The scattering factor is therefore a Fourier transform of the electron density of the atom. The same method can be used, with certain restrictions, for calculating the scattered amplitude from larger structures as well (cf. chapter 4).

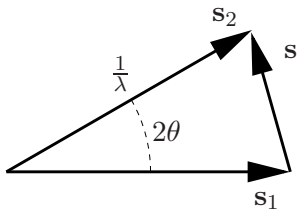

Figure 2.4: Relation between the incident ($\mathbf{s}_1$) and outgoing ($\mathbf{s}_2$) wave-vectors and the scattering vector ($\mathbf{s}$) and the scattering angle 2θ.

A classical view can explain the general properties of elastic scattering quite well. In this picture the electrons are bound to the atomic nucleus, and therefore are not completely free to respond to the driving force of the electric field [15, ch. 4], and (2.16) is not completely accurate. Instead, the electrons can be thought of as harmonic oscillators, with the natural frequencies corresponding to the binding energies. When these oscillators are driven by the electric field of the incoming radiation, there is an additional phase shift and modulus change in the scattering as compared to the case of free electrons. The amplitude scattered from an atom is therefore a complex quantity $f = (f_0 + f') + if''$. Here f_0 is obtained from (2.16), f' corresponds to an additional change in modulus, and f'' to the phase shift of $\pi/2$ [31]. Because the scattering from a plane of atoms is already $\pi/2$ behind the incident wave, the additional phase shift $\pi/2$ via f'' corresponds to absorption [15, p. 138].

Tabulations of the components of the scattering factor, based on experiments and quantum mechanical calculations, are found in the literature [31, 32]. Figure 2.5 shows the components of scattering factor for oxygen. It is seen that far above the absorption edges f' and f'' approach zero, so that the electrons behave almost as if they were free.

2.2.3 Inelastic Scattering

Inelastic scattering refers to the case where the energy of the photon changes in the scattering process. When a photon is scattered from a free stationary electron, its energy change can be deduced from the conservation of momentum. The change in photon energy is simpler to express as a change in wavelength, and in scattering to angle 2θ[c] the wavelength of the photon

[c]Normally θ is used as the scattering angle in inelastic experiments, but we use 2θ to have the same notation as in the case of elastic scattering.

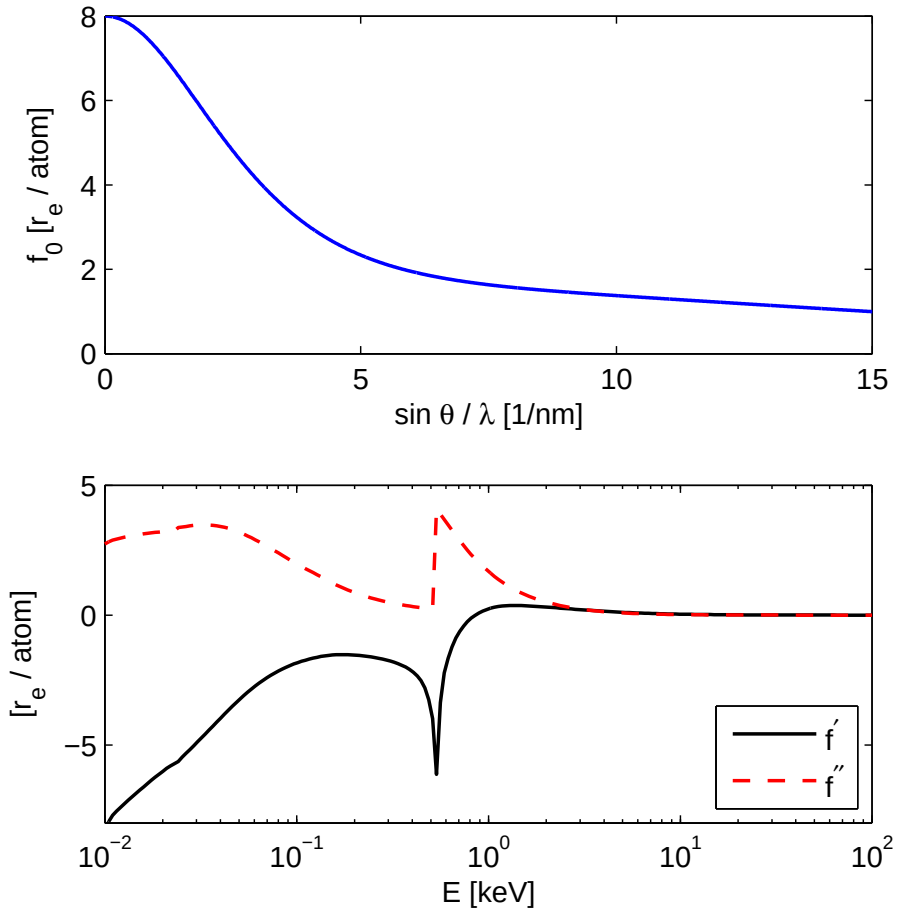

Figure 2.5: The components of the scattering factor for independent oxygen atoms [21]. The K-absorption edge is at 0.54 keV.

changes from λ to λ' according to [33, pp. 204–208]

$$\lambda' = \lambda + \lambda_c[1 - \cos(2\theta)]. \tag{2.17}$$

Here $\lambda_c = h/(m_e c)$ is the Compton wavelength.

Inelastic scattering from atoms may take place when the photon energy change corresponding to (2.17) is enough to either excite or ionize an atom. Tabulations of the total atomic cross section for inelastic scattering can be found in the literature [21, 22]. Atomic electrons are non-stationary, which broadens the photon energy spectrum seen at a given angle, and the shape of this spectrum can be used to study the electron momentum distribution in the sample [34].

The angular distribution of Compton scattering from a free electron varies with the energy as given in the formulation by Klein and Nishina [35],

$$\frac{\mathrm{d}\sigma(2\theta)}{\mathrm{d}\Omega} = \frac{r_e^2}{2}\left[\frac{1}{1+k(1-\cos 2\theta)}\right]^2 \times \left[1 + \cos^2 2\theta + \frac{k^2(1-\cos 2\theta)^2}{1+k(1-\cos 2\theta)}\right], \tag{2.18}$$

where $k = E/(m_e c^2)$. The atomic arrangement does not change the intensity distribution of Compton scattering, although it can have an observable effect on the spectrum [34].

2.2.4 Refraction and Reflection

As the x-rays are scattered their phase is altered, and thus when the scattered wave is summed with the incoming wave, there is a change in the phase velocity that depends on the scattering properties of the material. This leads to the index of refraction being different from zero, and it is generally expressed as [15, pp. 137-138,167]

$$n = 1 - \delta - i\beta, \tag{2.19}$$

where δ is the part corresponding to the change in the phase velocity, and β corresponds to absorption. For a material with N_i scatterers of type i in a unit volume,

$$\delta = \frac{r_e 2\pi(c\hbar)^2}{m_e E^2}\sum N_i(Z_i + f_i'), \tag{2.20}$$

$$\beta = \frac{r_e 2\pi(c\hbar)^2}{m_e E^2}\sum N_i f_i'', \tag{2.21}$$

where Z_i is the charge of scatterer i. The phase term δ is of the order of 10^{-7} for biological tissues at 50 keV.

The real part of the refractive index is generally slightly less than 1. This means that the phase velocity is greater than the speed of light, and refraction for a beam coming from vacuum to a material is away from the

surface normal. If absorption is weak (i.e. $\beta \approx 0$) the refractive index is $n = 1 - \delta$, and for an interface between two materials the Snell's law applies [18, pp. 39–40]

$$n_1 \sin\theta_1 = n_2 \sin\theta_2, \tag{2.22}$$

where θ_1 and θ_2 are the the angles between the surface normal and the incident and transmitted beams, respectively. Because the changes in δ are very small, the refraction angles are also small, typically of the order of 1 μrad. The real part of n being less than 1, there is a possibility for total external reflection when θ_1 is close to 90 degrees. This is used in the construction of x-ray mirrors (cf. section 2.3.2).

2.3 X-Ray Instrumentation

2.3.1 Sources of X-Rays

Several physical phenomena can be used for the production of x-rays. Those most commonly used are the relaxation of excitations in atomic electrons and acceleration of charged particles. The technical solution for generating a large flux of x-rays is usually either an x-ray tube or a synchrotron. From the imaging point of view it is important that the source is able to generate a sufficient flux of photons on the sample in a suitable energy range, so that the imaging time is not too long, and that the photon energy can be optimized to get good image quality with low dose. The related characteristics of x-rays are the total flux, the opening angle of the radiation cone, and the spectrum of the radiation. These parameters are summarized in a quantity called spectral brightness, which is expressed in units

$$\text{photons} \,/\, \text{s} \,/\, \text{mrad}^2 \,/\, (0.1\%\, \Delta E \,/\, E).$$

The size of the radiation region (the effective source size) affects the image quality by causing blur in the images. Because the angular size of the source determines the lateral coherence, the effective source size affects coherence as well. If the source size is important, then quantity called spectral brilliance is useful, and it is expressed in units

$$\text{photons} \,/\, \text{s} \,/\, \text{mm}^2 \,\text{source area} \,/\, \text{mrad}^2 \,/\, (0.1\%\, \Delta E \,/\, E).$$

Brightness is brilliance integrated over the source area.

Synchrotrons

Synchrotrons produce x-ray beams with superior properties as compared to other sources. They are used in most of the imaging experiments that utilize refraction, scattering, or coherence.

The term synchrotron refers to a specific type of circular particle accelerator, where charged particles moving at relativistic speeds are kept on stable orbits with the help of bending magnets and radio frequency cavities [36]. Synchrotron radiation is produced when the electrons undergo radial acceleration in the bending magnets, and in specially constructed insertion devices, wigglers and undulators, that consist of periodic magnetic structures. The radiation spectrum is continuous, spanning from the infrared to the hard x-rays.

Synchrotrons have a high flux and the opening angle of the radiation cone is small, typically less than 1 mrad in the vertical direction and a bit larger in the horizontal direction depending on the source type (for undulators < 1 mrad, for wigglers ~ 10 mrad, and for bending magnets ~ 100 mrad) [36]. Due to the small effective source size the beam has good lateral coherence. The high flux makes use of tunable monochromatic beams practical, and allows techniques that use multiple beams of well defined energies. The small opening angle is useful when well collimated beams or large intensities are required, but makes imaging of large samples more difficult, as a large distance between the source and the sample is needed in order to cover the whole sample.

The spectral brightness for a bending magnet on the axis of the radiation cone is [36]

$$I(\lambda) = 1.325 \times 10^{10} \left(\frac{\lambda_c}{\lambda}\right)^2 K_{2/3}^2 \left(\frac{\lambda_c}{2\lambda}\right) E^2 i_c, \tag{2.23}$$

where λ is the wavelength, $\lambda_c[\mathrm{nm}] = 1.86/(B[\mathrm{T}]E[\mathrm{GeV}]^2)$ is the characteristic wavelength of the source [37], E is the electron energy, B is the peak magnetic field, i_c is the ring current and $K_{2/3}$ is a modified Bessel function of the second kind [38]. The spectral brightness for a wiggler with N poles closely resembles that of a bending magnet, and it is obtained by multiplying (2.23) by N. Table 2.2 summarizes the characteristics of some of the beamlines that have successfully been used in analyzer based and propagation based imaging.

X-Ray Tubes

X-ray tubes are the most widely used x-ray sources. X-rays are produced by colliding electrons with a metal target (anode), where sudden deceleration of the electrons and the ionization and subsequent relaxation of target atoms give rise to continuous background (bremsstrahlung) and characteristic lines, respectively. Electron energies used typically vary between 10–200 keV. The radiation field is not well collimated so that only a small fraction of the radiation can be used in experiments. The maximum available intensity is limited by the heating of the anode material. Rotating anodes are used routinely in medical imaging to improve the available intensity by distributing the heat

Table 2.2: Typical operating parameters of three synchrotron beamlines that are used in imaging.

Beamline	ID 17 (ESRF) [39]	SYRMEP (Elettra) [40, 41]	BL20B2 (SPring-8) [42]
Source type	Wiggler	BM	BM
E [GeV]	6	2	8
Peak B [T]	0.616	1.46	0.68
λ_c [nm]	0.084	0.318	0.043
i_c [mA]	200	330	100
Number of poles	21	1	1
Source size (FWHM H×V) [μm^2]	59×8.3	135×80	114×14
Beam divergence (FWHM H×V) [$mrad^2$]	3.3×0.1	7×0.25	1.5×0.06
Sample distance [m]	150	20	200
Beam size at sample (H×V) [mm^2]	150×1	120×4	300×20
$\Delta E/E$ at sample	10^{-5}	10^{-4}	$3 \cdot 10^{-5}$
Typical photon energy E [keV]	50	20	50
Photon flux at sample [phot./s/mm^2]	$3 \cdot 10^8$	$2 \cdot 10^8$	$6 \cdot 10^7$

load over a larger area [43]. Further improvements could be achieved with the use of liquid anodes [44]. Although the brightness is much less than in synchrotrons, x-ray tubes are well suited for imaging applications where strict monochromaticity is not needed.

Compact Sources

Compact sources are sources of small size (as compared to synchrotrons), small enough to be used e.g. for imaging applications in hospitals, yet with potentially much higher intensities than conventional x-ray tubes. Currently promising progress is made using a table top synchrotron with a small target in the electron beam to generate the photons [45, 46], and sources based on inverse Compton scattering [47,48]. Especially the inverse Compton scattering promises high flux of photons (10^{10} photons/s) in 8 ps quasimonochromatic pulses (1% $\Delta E/E$) with tunability between 8 and 100 keV, with the possibility to take x-ray images with a single 8 ps long pulse [48]. These types of developments promise that in the near future many imaging techniques developed at synchrotron beamlines can be transferred to hospital use.

2.3.2 X-Ray Optics

X-ray optical elements are used to modify the beam shape, the focus and the spectrum so that these properties match the needs of the experiment in question. Optical elements are used also on the analysis side to collect and differentiate the signal coming from specific interactions with the sample. Refractive optics for x-rays exist [49], but their use is limited due to the refractive index being close to 1. Diffraction from perfect crystals and total external reflection (mirrors) are more commonly used. The angular acceptance of these types of elements is small, e.g. few microradians for perfect crystals, so that careful instrumentation and elimination of vibrations is essential. In imaging, optics are useful in selecting the desired energy bandwidth and also in separating refracted and scattered beams from the direct beam.

Crystal monochromators

Crystal monochromators are based on x-ray reflection from a perfect crystal, either in the reflection (Bragg) or transmission (Laue) geometries. The main use for crystals is to select a narrow band from the spectrum [50]. Crystals can also be used in focusing the beam (bent crystals) or changing the size of the beam (asymmetrically cut crystals) [50]. The effect of a crystal is characterized by its reflection curve that describes the part of the spectrum reflected for a well collimated broadband beam. Equivalently, the reflection curve describes how the deviation from the exact Bragg angle affects the reflectivity for a monochromatic beam.

Let the Miller indeces of the reflection be hkl and the plane spacing d_{hkl} [51, ch. 2]. For a thick perfect crystal in the reflection geometry, the reflectivity of intensity for an incoming plane wave is [52, p. 173]

$$R(\eta) = \left|\frac{\chi_{hkl}}{\chi_{\bar{h}\bar{k}\bar{l}}}\right| \left|\eta \pm \sqrt{\eta^2 - 1}\right|^2 . \tag{2.24}$$

Here $\chi_{hkl} = -r_\mathrm{e}\lambda^2 F_{hkl}/(\pi V)$ is the Fourier component of the crystal polarizability for reflection hkl, r_e is the classical electron radius, F_{hkl} the structure factor and V the unit cell volume [52, pp. 37–38]. The deviation parameter η determines the width of the reflectivity curve [52, p. 136],

$$\eta = \frac{\Delta\theta \sin(2\theta_\mathrm{B}) + \chi_0(1-\gamma)/2}{\sqrt{|\gamma|}|C|\sqrt{\chi_{hkl}\chi_{\bar{h}\bar{k}\bar{l}}}}. \tag{2.25}$$

The asymmetry factor $\gamma = -1$ for a symmetric reflection and the polarization factor $C = 1$ for the σ-polarized radiation (electric field in the plane of the crystal) and $C = \cos 2\theta_\mathrm{B}$ for the π-polarizated radiation (electric vector in the plane of diffraction). Angular deviation $\Delta\theta$ expresses the difference of crystal orientation from the exact Bragg angle θ_B. Plots illustrating the

behaviour of the reflectivity, calculated from (2.24) and (2.25) are shown in figure 2.6.

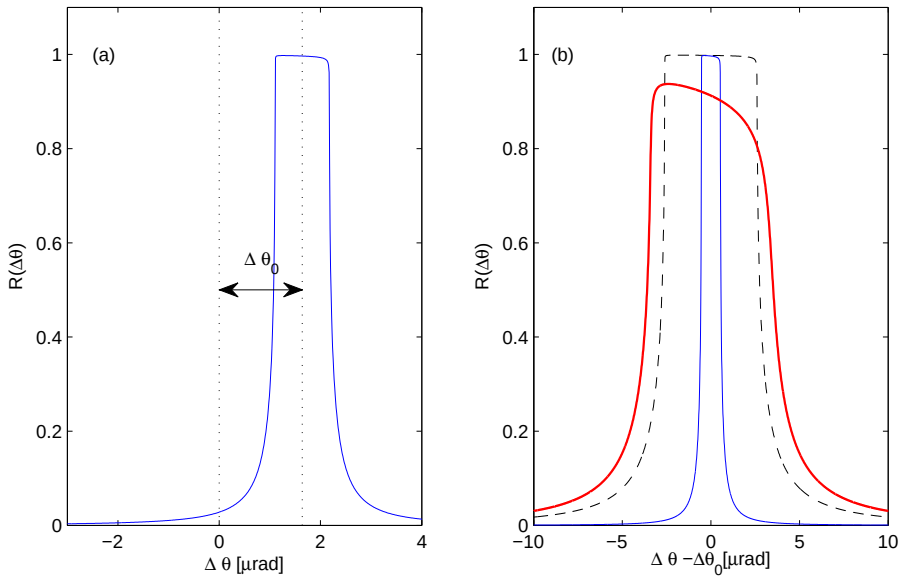

Figure 2.6: Calculated reflectivity for Si 333 at 50 keV (a). The deviation (due to refraction) from the geometrical Bragg angle is marked with $\Delta\theta_0$. Reflectivity (centered at 0) for Si 333 at 50 keV (thin solid line), Si 111 at 50 keV (dashed line) and Si 333 at 10 keV (thick solid line) (b).

The bandpass of a crystal for a symmetric reflection is [50, pp. 272–273]

$$\frac{\Delta E}{E} = \frac{4r_e d_{hkl}}{\pi V}|C||F_{hkl}|\exp(-M), \tag{2.26}$$

where $\exp(-M)$ is the temperature factor. As long as F_{hkl} is independent of energy so is the bandpass. For the special cases of silicon 111 and 333 reflections the bandpasses are 14.1×10^{-5} and 0.88×10^{-5}, respectively. By bending the crystal the bandpass can be further increased [53].

Monochromator crystals pass also higher harmonics of the intended radiation frequency. This can have a detrimental effect on image quality [54]. As seen in figure 2.6 the angular FWHM of the reflecting range is smaller for higher energies. Therefore using two identical crystals at slightly different orientations allows the elimination of higher harmonics while passing most of the intended frequency through [50, pp. 303–307].

Mirrors

The real part of the refractive index for x-rays (2.19) is below 1, and thus x-rays exhibit total external reflection at the interface of vacuum and matter.

For x-rays the critical angle for this reflection is

$$\theta_c[\text{mrad}] = k\lambda[\text{nm}]\sqrt{\rho[\text{g/cm}^3]}, \tag{2.27}$$

where k is a constant and is 16 for low-Z materials [55]. Typically θ_c is of the order of 0.5 mrad for x-rays of 50 keV. The rays incoming below the critical angle are well reflected, while those above this angle are highly attenuated. Although mirrors made of heavy materials have wider critical angles than those of light materials, the increased absorption of heavier elements reduces the reflectivity below the critical angle from the maximum possible value, so that a compromise has to be made.

Bent mirrors can be used to focus or widen the beam. Because decreasing the wavelength reduces θ_c as well, mirrors can be used to cut radiation above certain threshold energy. They can be used in combination with crystal monochromators to obtain almost perfect harmonics rejection [50, pp. 303–307].

2.3.3 Detection of X-Rays

X-ray detectors can be based on several different principles, but typically they are based on collecting and counting the electrons created by ionization of atoms in the detector. Photon counting detectors give an output pulse for each x-ray quantum that they detect. Integrating detectors accumulate the signal over a longer period of time, and add the signals from individual photons before passing the signal onward. Photon counting detectors usually have a low noise level and may offer the possibility for resolving the energy of the photons as well. The dead time between detection of two photons can, however, be too long for imaging purposes. Integrating detectors do not have a limit on the incoming photon flux, but they suffer from additional background noise that is not present in photon counting detectors.

Detector Characterization

The detector properties that primarily affect the image quality are the noise and the spatial blur introduced by the detector. The detector efficiency in detecting the incoming photons affects the dose that is required for getting images with certain level of photon statistics. The dynamic range of the detector defines how large signal variations can in principle be observed, although in this respect imaging is not particularly demanding.

Perhaps the most important figure of merit characterising detectors is the detective quantum efficiency (DQE) [56] expressed as

$$\text{DQE}(f) = \frac{\text{SNR}_{\text{out}}{}^2(f)}{\text{SNR}_{\text{in}}{}^2(f)}, \tag{2.28}$$

where $\mathrm{SNR_{in}}$ and $\mathrm{SNR_{out}}$ are the signal-to-noise ratios of the input and output signals of the detector and f is the spatial frequency. For a perfect detector DQE = 1 for all frequencies f. For a realistic detector DQE approaches zero above some corner frequency and is less than one at other frequencies.

The spatial blur is characterized by the point spread function (PSF). PSF is defined as the detector response to an impulse. Each detector has a different PSF, and accurate measurements require the PSF to be characterized through measurements. The PSF reduces the spatial resolution of the detector, and in high dynamic range studies the possible low intensity tails of the PSF may also be important in changing the shape of e.g. recorded scattering curves [57].

The detector that has been used for the experimental imaging results used in this work is the FReLoN detector at ESRF [58,59]. FReLoN consists of a fluorescent screen that is coupled to a CCD with an optical taper. The dimensions of the active area are 94 by 94 $\mathrm{mm^2}$, and the effective pixel size is $46 \times 46\,\mu\mathrm{m}^2$ [60, chapter 4]. At 51.5 keV energy DQE ≈ 0.4 at low spatial frequencies, and the FWHM of the PSF is around 200 μm, i.e. about 4 pixels [60].

Chapter 3

X-Ray Imaging Methods

3.1 X-Ray Imaging Principles

Imaging with hard x-rays is done in the transmission mode, where the sample is placed between the x-ray source and the detector, and the x-rays pass through the sample. In figure 3.1 this type of setup is shown schematically. The transmitted radiation arriving at the detector may be attenuated, refracted and scattered, depending on the properties of the sample. It depends on the details of the imaging setup how the effects of the different contributions can be separated.

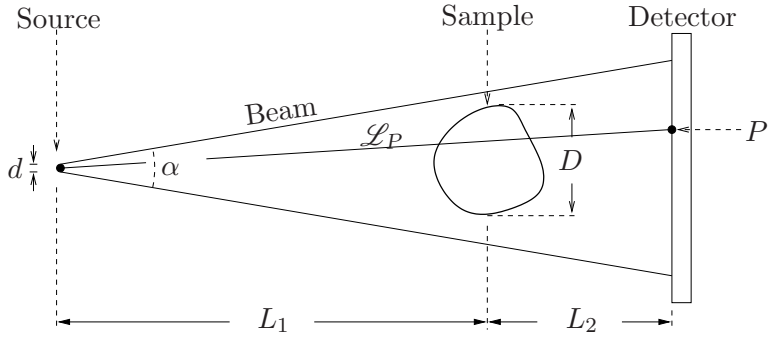

Figure 3.1: A schematic drawing of an x-ray radiography setup. α is the opening angle of the incoming beam, d is the size of the source, D is the size of the sample, and L_1 and L_2 are the distances from the source to the sample and from the sample to the detector, respectively. P is a point on the detector and $\mathscr{L}_P$ is the line from the source to the point P.

We are interested in imaging methods that are able to detect the effects of refraction and to separate the scattering from the direct beam. In general refraction and scattering depend on the phase differences occuring within the sample so that such methods are often referred to as phase contrast

imaging methods. We focus especially on elastic scattering coming in the small-angle region, because this carries information about structures whose size ranges from few nanometres to micrometres, such as typically found in biological tissues.

Phase contrast can be studied with many different methods. We focus our attention on the analyzer based imaging (ABI) method which was originally developed for imaging x-ray refractions within the sample [61]. ABI uses a monochromator and an analyzer crystal to obtain the angular distribution of the radiation coming from the sample. Different authors have used varying terminology, such as diffraction enhanced imaging (DEI) and multiple image radiography (MIR), cf. e.g. [62–69]. In addition to obtaining the refraction angle, ABI can also be used for scatter rejection and analysis of the scattering shape. ABI offers angular resolution of $0.1\,\mu$rad, and complete scatter rejection above the angular range of a few μrad.

3.2 Image Quality

Image quality is primarily described by two criteria: what is the size of the smallest visible feature (resolution) and how small differences in the features are observable (contrast). Furthermore in CT the images can be either quantitative or qualitative, depending on whether the reconstructed values have a direct correspondence to values in the sample or not. Ultimately it is the application that dictates how good an image quality is required. In medical imaging the visual assessment by an experienced radiologist is what sets the standard on what is good image quality. Here we treat the factors that affect image quality, and the mathematical ways of quantifying it.

Noise

Noise in the images is related to the counting statistics and the properties of the experimental system. When counting N events (photons) on the average, there is natural variation in the values actually recorded due to the statistical nature of the process. This phenomenon is described well by the Poisson distribution that has the standard deviation $\sqrt{N}$ [70]. For large N the distribution shape approaches a Gaussian. Counting more photons by increasing the incoming flux or the imaging time reduces the effect of photon noise, leading to a compromise between noise level and the dose on the sample.

Fluctuation in the intensity of the incoming beam may be caused e.g. by oscillations in the storage ring, or by vibrations of the monochromator optics. This type of noise is multiplicative, and its effect cannot be diminished by increasing the incoming flux, although if the fluctuations are rapid compared to the exposure time, they can be averaged out by increasing the exposure time.

Background noise due to the detector is another important factor. There are three distinct types of background signal: i) constant background independent of the exposure time or the incoming flux (read-out noise), ii) background signal proportional to the exposure time (dark current), and iii) background proportional to the incoming intensity (e.g. stray scattering inside the detector). The constant background is the limiting factor when rather low counts are recorded during a short exposure, as often is done in imaging. When the incoming intensity is low the limiting factor may be the dark current due to the required long exposure time. For images containing large dynamic range the background proportional to the intensity may mask out features in areas of low intensity.

Blur

Blur causes sharp edges to appear as gradual changes in the image. The amount of blur (i.e. the width of the gradation) is determined by the system's PSF. Due to the general properties of PSF, the system's PSF is a convolution of the PSFs of the individual components. The effect of the PSF of the detector was mentioned in section 2.3.3. Another component of PSF is the source size, which was denoted in figure 3.1 by d. Effectively each point on the source surface (source element) is an independent point-source and forms an image on the detector. The images are laterally displaced relative to each other, depending on the distance of the source element from the source center. The width of the blur caused by this is $w = dL_2/L_1$. If the detector and source PSFs are Gaussians with standard deviations σ_{det} and σ_{src}, respectively, the whole system response has a Gaussian PSF with a standard deviation of $\sigma_{\mathrm{PSF}} = \sqrt{\sigma_{\mathrm{det}}^2 + \sigma_{\mathrm{src}}^2}$.

In medical imaging patient movement is another source of blur. Heartbeat, ventilation and peristaltic motion are among the main contributors to these motion artefacts. If $\sigma_{\mathrm{PSF}} \sim 100\,\mu\mathrm{m}$, even a small patient motion during the imaging will cause visible artefacts. In CT this can lead to substantial reconstruction errors. The best way to reduce the effect of patient motion is to reduce the imaging time. Some of the motion artefacts can in principle be reduced by either pre- or post-gating to the motion (e.g. the heartbeat) or by post-processing the images by inverting the effects caused by the motion [71–75].

Contrast and Signal-to-Noise Ratio

We define the contrast for a detail in an image as (compare e.g. with [43, p. 570])

$$C = \frac{|\bar{N}_{\mathrm{bg}} - \bar{N}_{\mathrm{obj}}|}{\max\{\bar{N}_{\mathrm{bg}}, \bar{N}_{\mathrm{obj}}\}}, \tag{3.1}$$

where $\bar{N}_{\mathrm{bg}}$ and $\bar{N}_{\mathrm{obj}}$ are the average counts recorded in the area of the background and the object, respectively. With this definition C is a quantity between 0 and 1, and values close to 1 mean that the object is well visible. By definition C is independent of the incoming intensity (and hence independent of dose). It is also independent of the imaging resolution, as long as the object size remains much larger than the resolution. It is therefore a true measure of the visibility of the object in radiographs. However, by not being dependent on the dose, contrast is not suitable for estimating the visibility of objects in real imaging situations where the allowed dose is an important factor.

Signal-to-noise ratio (SNR) is another way of measuring the visibility of an object,

$$\mathrm{SNR} = \frac{\text{Power in Signal}}{\text{Power in Noise}}, \tag{3.2}$$

which relates the signal strength to the random variation in the signal. This is a suitable measure for comparing images resulting from different methods in realistic situations, because it takes into account the sources of noise (such as counting statistics) that ultimately limit the object visibility in imaging. In the rest of the work we shall use SNR as the basis for estimating object visibility under different imaging situations. For an object consisting of M pixels the SNR is [76]

$$\mathrm{SNR} = \frac{\sqrt{M}|\bar{N}_{\mathrm{obj}} - \bar{N}_{\mathrm{bg}}|}{\sqrt{\sigma_{\mathrm{obj}}^2 + \sigma_{\mathrm{bg}}^2}}, \tag{3.3}$$

where σ_{bg} and σ_{obj} are the root-mean-square deviations in the photon counts in the background and in the object, respectively. According to Rose [76], a value of about 5 in (3.3) corresponds to the threshold of object visibility. In later chapters we report SNR values for the case $M = 1$, which can then be scaled by $\sqrt{M}$ to obtain SNR for different sized objects.

For some imaging methods, such as refraction contrast in analyzer based imaging, contrast is seen primarily at the edges of objects. In these cases the edge visibility and edge SNR are useful figures of merit, and they can be defined as [3]

$$V_{\mathrm{edge}} = \frac{N_{\mathrm{max}} - N_{\mathrm{min}}}{N_{\mathrm{min}} + N_{\mathrm{max}}}, \tag{3.4}$$

$$\mathrm{SNR}_{\mathrm{edge}} = \frac{N_{\mathrm{max}} - N_{\mathrm{min}}}{\sqrt{\Delta N_{\mathrm{bg}}^2 + \Delta N_{\mathrm{bg}}^2}}. \tag{3.5}$$

Here N_{min} and N_{max} are the minimum and maximum recorded counts in the (averaged) profile perpendicular to the edge direction.

Resolution

Resolution is determined by the amount of blur, usually quantified by the maximum number of line pairs / mm (lpmm) that can be resolved. In practice the ability to resolve an object depends also on the contrast and SNR. In imaging small objects the resolution is important, and enchancement of SNR near edges from refraction contrast may improve the resolution dramatically.

It is ultimately the visual assessment of image quality that decides whether or not some detail is well visible, i.e. if the combination of SNR and resolution are good enough. From (3.3) we see that SNR is proportional to the square root of object size, and this is true as long as the object is significantly larger than the resolution limit. Figure 3.2 shows examples of details of different size at various levels of SNR.

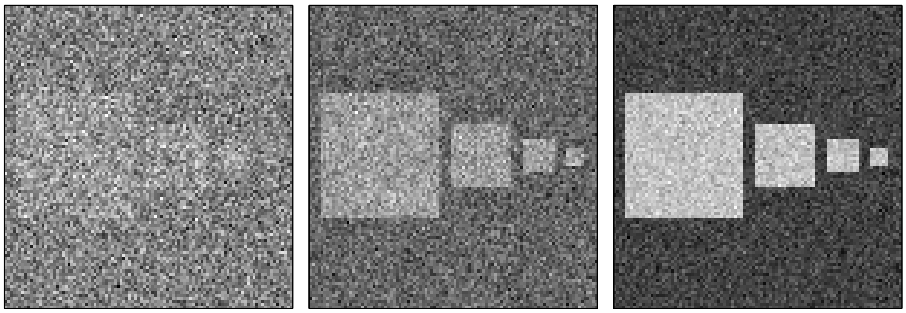

Figure 3.2: Object visibility illustrated for the case when SNR for a single pixel is 1 (a), 10 (b) and 100 (c). Four objects are present in each image, with sizes (from left to right) $\sqrt{M} = 41, 21, 11$ and 6.

3.3 Imaging Based on Attenuation

In the first approximation the sample's contribution to the intensity recorded at a point P on the detector depends only on the attenuation along the line of sight from the source to point P (see figure 3.1). X-ray imaging with attenuation is based on this assumption, and in many cases it is sufficienty good to produce quantitative images of the density of the sample. Mathematically this can be expressed as

$$I_P = I_0 \exp\left[-\int_{\mathscr{L}_P} \left(\frac{\mu}{\rho}\right)_{\mathbf{r}} \rho(\mathbf{r}) \mathrm{d}\mathbf{r}\right], \tag{3.6}$$

where I_0 is the intensity that would be recorded at the detector when there is no sample, $(\mu/\rho)_{\mathbf{r}}$ and $\rho(\mathbf{r})$ are the mass absorption coefficient and density

at point $\mathbf{r}$, respectively, and integration is carried out along the line $\mathscr{L}_P$ from the source to point P. The integrand in the exponent is the linear attenuation coefficient $\mu(\mathbf{r}) = (\mu/\rho)_{\mathbf{r}}\rho(\mathbf{r})$, and the line-integral is

$$\int_{\mathscr{L}_P} \mu(\mathbf{r})\mathrm{d}\mathbf{r} = -\log\left(\frac{I_P}{I_0}\right). \tag{3.7}$$

Variation of the attenuation for different positions of the sample gives important clues about the internal structure of the sample.

While (3.7) gives the line integral of the sample, the linear attenuation coefficient $\mu(\mathbf{r})$ cannot be solved from a single radiograph alone, except for homogeneous samples. In CT imaging the sample is rotated around the z-axis and several radiographs (projections in CT terminology) are taken at different angles of rotation ϕ, and this allows the reconstruction of $\mu(\mathbf{r})$. Figure 3.3 shows the principle of CT schematically. The collection of projections for a given z-coordinate z_0 is called a sinogram. Under the assumption that the attenuation is the only effect, the sinogram can be expressed mathematically as a Radon transform of $\mu(x, y, z_0)$ [9],

$$S(\phi, x', z_0) = \int_{-\infty}^{\infty} \mu(x'\cos\phi - y'\sin\phi, x'\sin\phi + y'\sin\phi, z_0)\mathrm{d}y'. \tag{3.8}$$

This is similar to (3.7), for any given ϕ, but now the integration route $\mathscr{L}_P$ has been explicitly written out.

There are several methods for inverting the Radon transform (3.8) so as to obtain μ [9]. We use the filtered back-projection method for calculating the tomographic images presented in this work [9, 77]

$$\begin{aligned} \hat{\mu}(x, y, z_0) &= \int_0^{\pi}\int_{-\infty}^{\infty} H(\nu)\left(\int_{-\infty}^{\infty} S(\phi, x', z_0)\exp[-2\pi i x'\nu]\mathrm{d}x'\right) \\ &\times \exp[2\pi i\nu(x\cos\phi + y\sin\phi)]\mathrm{d}\nu\mathrm{d}\phi. \end{aligned} \tag{3.9}$$

In practice we have used the reconstruction given by the software package MATLAB (macro `iradon.m`, Mathworks, Natick, Massachusetts) with linear interpolation and filter $H(\nu)$ selected to be of the Shepp-Logan form [78, ch. 10]. The transform pair (3.8) and (3.9) is valid for any property of the sample whose recorded value can be expressed as a line integral, so that in principle other quantities besides the attenuation coefficient can also be reconstructed.

The accuracy of (3.9) requires that the sinogram is sampled sufficiently densely in the angle ϕ and coordinate x'. In practical imaging situations the sampling intervals are always finite, which limits the accuracy of the reconstructed images. Methods that work better than (3.9) in the case of sparse projections (i.e. $\Delta\phi$ large) exist, making it possible to reduce the number of projections in some cases [79–84]. Reducing the number of projections reduces the dose, which in some medical imaging applications may be the limiting factor.

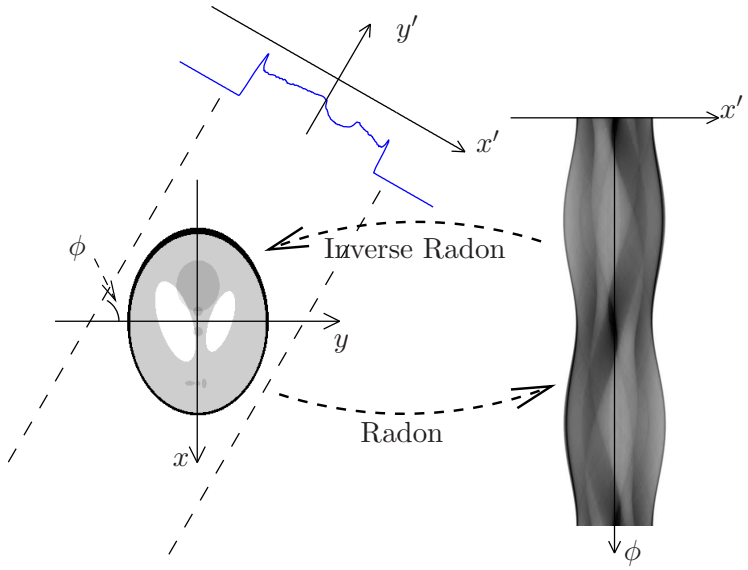

Figure 3.3: The principle of CT. On the left is shown the object (Shepp-Logan head phantom) and projection at $\phi = 60°$. On the right is shown the complete sinogram. Mathematiclly Radon and inverse Radon transforms connect the object and the sinogram.

3.4 Analyzer Based Imaging

Figure 3.4 shows the principle of ABI. From the incoming beam that is highly parallel and polychromatic a narrow energy band is selected by the monochromator. The beam is then partially reflected by the analyzer crystal (typically identical to the monochromator), depending on how well the angle of incidence matches with the angle of incidence on the monochromator. This type of setup, known as Bonse-Hart camera, is often used in small-angle scattering studies [85]. The angular width of the reflection curve of a crystal is only a few microradians (cf. section 2.3.2) so that the monochromator and analyzer have to be oriented very nearly parallel for the x-rays to pass through. The deviation of analyzer orientation from the monochromator, rocking angle, is $\theta_{\mathrm{R}} = \cos^{-1}(-\mathbf{n}_1 \cdot \mathbf{n}_2)$. When the analyzer orientation is scanned, a rocking curve (RC) is recorded, denoted by $R(\theta_{\mathrm{R}})$. Mathematically RC is the convolution of the individual rocking curves of the monochromator and the analyzer, $R_{\mathrm{m}}(\theta)$ and $R_{\mathrm{a}}(\theta)$,

$$R(\theta_{\mathrm{R}}) = R_{\mathrm{m}}(\theta) \circledast R_{\mathrm{a}}(\theta). \tag{3.10}$$

An example of a rocking curve for a setup using Si 333 analyzer and monochromator at 51.5 keV x-ray energy is shown in the inset of figure 3.4.

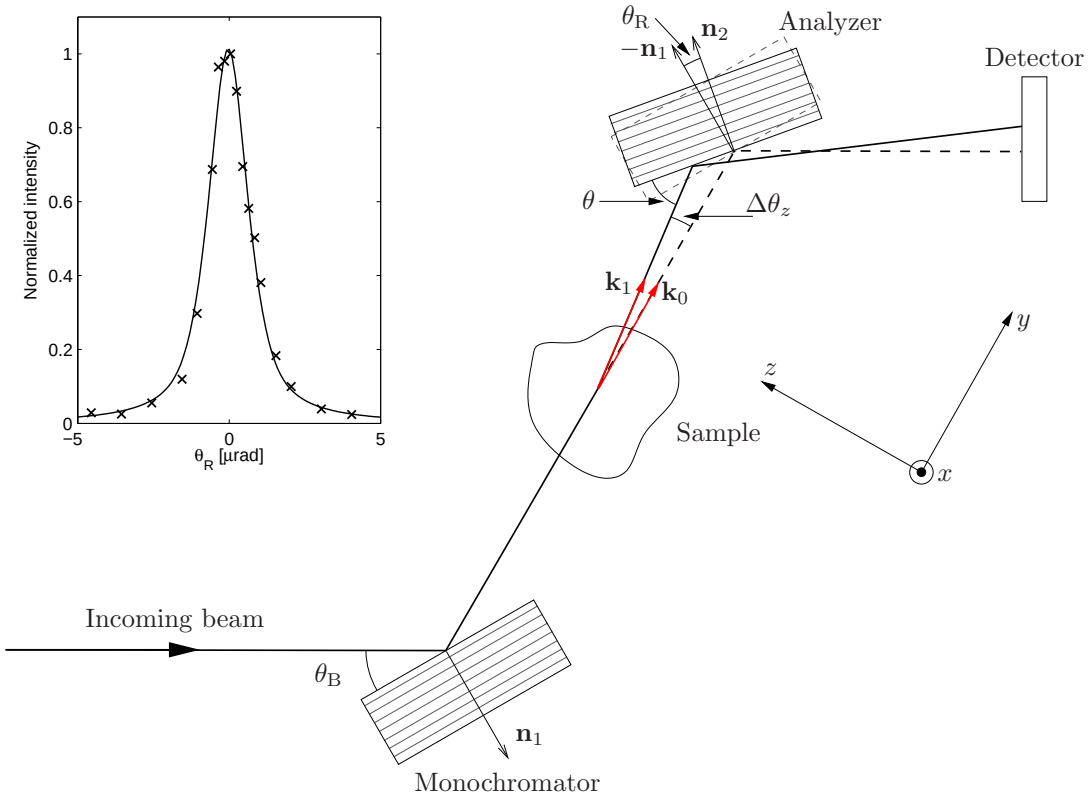

Figure 3.4: A schematic figure of the setup used in ABI imaging, showing the notation for the angles. The coordinate system convention is also shown. The inset shows an experimental rocking curve (crosses) along with a fit (line) recorded at ID17 at ESRF for a single detector pixel without a sample using the x-ray energy 51.5 keV.

The RC recorded without a sample is called the intrinsic RC, and denoted $R_{\mathrm{int}}(\theta_{\mathrm{R}})$. A sample modifies the intensity, direction and angular distribution of the beam coming to the analyzer, thus changing the shape of the RC. Examples of a possible effect of a sample on the RC are shown in figure 3.5. The intensity coming from the sample consists of the direct and the scattered beam. We denote the angular distribution of scattering by $F(\theta_x, \theta_z)$, which is normalized to unit area. The direct and the scattered beam are refracted by the angle $(\Delta\theta_x, \Delta\theta_z)$, and the absorption causes attenuation by a factor $\exp[-\mu T]$. The intensity is divided so that fraction ξ remains in the direct beam and fraction $(1-\xi)$ is scattered. The intensity coming from the sample is then

$$I(\theta_x, \theta_z) = I_0 e^{-\mu T}[\overbrace{\xi\delta(\theta_x - \Delta\theta_x, \theta_z - \Delta\theta_z)}^{\text{Direct beam}} + \overbrace{(1-\xi)F(\theta_x - \Delta\theta_x, \theta_z - \Delta\theta_z)}^{\text{Scattered beam}}]. \tag{3.11}$$

Analysis of $I(\theta_x, \theta_z)$ can reveal absorption $(e^{-\mu T})$, refraction angle $(\Delta\theta_x, \Delta\theta_z)$, fraction of scattering $(1-\xi)$, and angular distribution of the scattered intensity $(F(\theta_x, \theta_z))$. Attenuation with scatter rejection (apparent absorption) is $e^{-\mu T}\xi = e^{-\mu_{\mathrm{attn}} T}$.

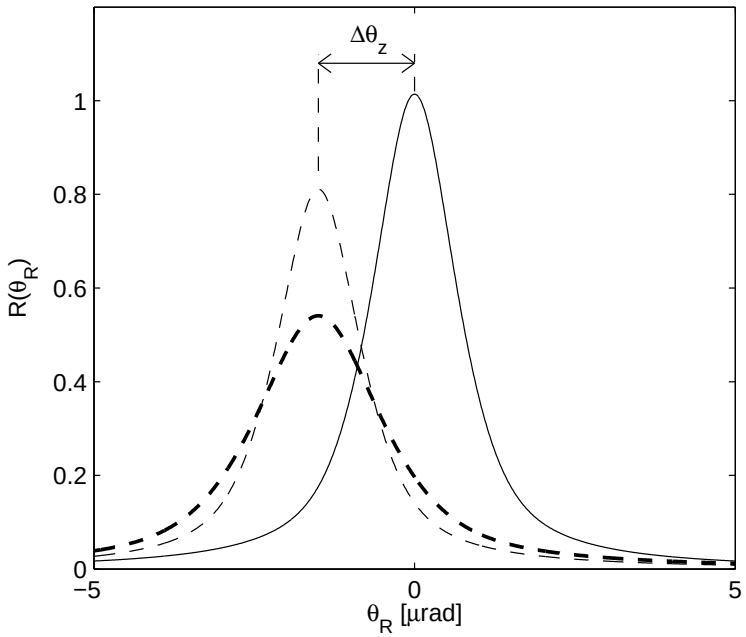

Figure 3.5: Examples of rocking curves for different cases: intrinsic curve (solid line); refraction and attenuation ($e^{-\mu T} = 0.8$), (thin dashed line); refraction, attenuation ($e^{-\mu T} = 0.8$) and scattering (thick dashed line).

The analyzer lets part of the intensity through, depending on θ_{R} and the angular distribution of intensity. Because the analyzer does not differentiate between angles in the lateral direction (θ_x), the intensity is integrated over the incoming beam width. Normalized by the incoming intensity, the RC in the presence of a sample is

$$R(\theta_{\mathrm{R}}) = \frac{1}{I_0} \int R_{\mathrm{int}}(\theta_{\mathrm{R}} - \theta_z) \left[\int I(\theta_x, \theta_z) \mathrm{d}\theta_x \right] \mathrm{d}\theta_z. \tag{3.12}$$

Integration in the lateral direction causes some information about the original intensity distribution to be lost. Especially $\Delta\theta_x$ cannot be recovered, and for the $F(\theta_x, \theta_z)$ we see only the laterally integrated profile. The other parameters ξ, $\Delta\theta_z$ and $e^{-\mu T}$, can however be recovered.

The actual measurement of the analyzer rocking curve can be done only for a finite set of angles, each with only a limited number of incoming photons, leading to sparse and noisy data, terminated at some maximum θ_{max}. These features further complicate the finding of the true shape of the incoming intensity distribution. There are several methods for analyzing the RC shape in ABI, and we will now introduce some of these methods.

3.4.1 Rocking Curve Analysis Methods

The aim is to be able to quantify the shape of the RC using measurements at as few rocking angles as possible. The shape of the intrinsic RC is known accurately from measurements without a sample, and this information is used by all the methods. Table 3.1 gives a summary of the different RC analysis methods.

RC Series Expansion

By considering the Taylor expansion of the RC several different approaches can be devised that give information on the change of peak position (refraction), peak broadening (scattering) and the total area under the RC (attenuation). The derivatives of the intrinsic RC, $R_{\mathrm{int}}^{(N)}(\theta_{\mathrm{R}})$, are known, and used in the Taylor expansion. Figure 3.6 shows a typical selection of points that are used by series expansion methods.

By considering only the linear term, $R(\theta_0 + \Delta\theta) \approx R(\theta_0) + R'(\theta_0)\Delta\theta$, the original DEI algorithm is able to resolve the refraction angle (θ_{refr}) and the attenuation ($e^{-\mu_{\mathrm{attn}} T}$) with good scatter rejection from two intensity measurements taken at angles θ_{L} and θ_{H} [61]. This method works only when the refraction angles are small enough so that the incoming angle remains in the region where the RC is approximately linear, i.e. in the region of steep slope in the RC, and that the slope of the RC does not change due to

Table 3.1: Summary of different RC analysis methods. The N analyzer angles used in some of the methods are usually evenly and symmerically distributed around the central peak of the RC. The other angle positions are illustrated in figure 3.6.

	Analyzer angles	Parameters resolved	Note
DEI	θ_{L}, θ_{H}	$\Delta\theta_z$, $e^{-\mu_{\mathrm{attn}}T}$	Assumes no scattering
E-DEI	θ_{L}, θ_{H}, θ_{TOP}	$\Delta\theta_z$, $e^{-\mu_{\mathrm{attn}}T}$, σ_{RC}	
W-DEI	θ_{L}, θ_{H}, θ_{TOP}, $-\theta_{\mathrm{W}}$, $+\theta_{\mathrm{W}}$	$\Delta\theta_z$, $e^{-\mu_{\mathrm{attn}}T}$, σ_{RC}, γ_{W}	Additional wide angle parameter γ_{W}
MIR	N	$\Delta\theta_z$, $e^{-\mu_{\mathrm{attn}}T}$, σ_{RC}	
Gaussian fit	N	$\Delta\theta_z$, $e^{-\mu_{\mathrm{attn}}T}$, σ_{scat}, ξ	Resolves scattering fraction $1-\xi$
pseudo-Voigtian fit	N	$\Delta\theta_z$, $e^{-\mu_{\mathrm{attn}}T}$, σ_{scat}, ξ	Resolves scattering fraction $1-\xi$

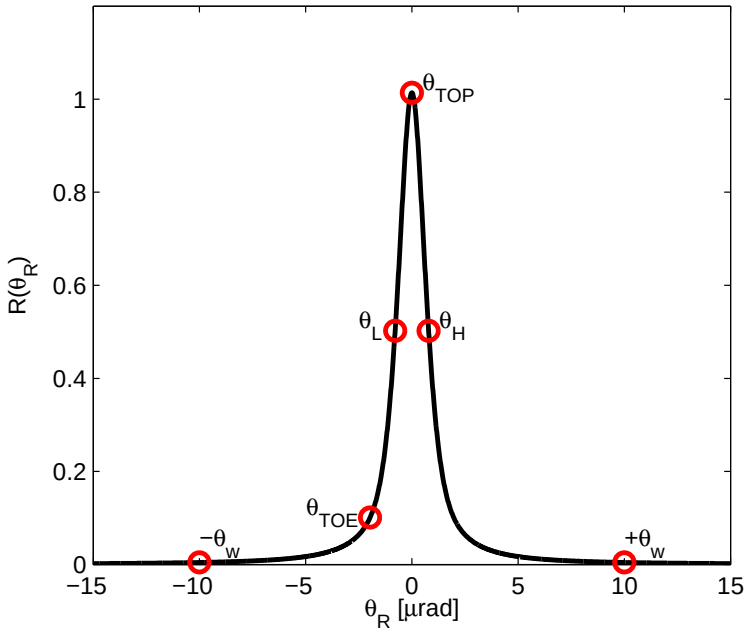

Figure 3.6: Typical points used in algorithms based on a series expansion of the RC.

scattering from the sample (i.e. $R'(\theta_{\mathrm{L}}) = R'_{\mathrm{int}}(\theta_{\mathrm{L}})$). Noise properties of the DEI algorithm have been analyzed in [86].

If there is scattering, or there are refracting objects smaller than the pixel size, the shape of the RC will change from the intrinsic one. Then additional points can be used to quantify the change in the shape and peak position. By considering points θ_{TOE} and θ_{TOP} (cf. figure 3.6) it is possible to obtain the broadening and attenuation in the case of no net refraction, i.e. $\theta_{\mathrm{refr}} = 0$ [87]. With three points (e.g. θ_{L},θ_{H} and θ_{TOP} in figure 3.6, chosen so that $R''_{\mathrm{int}}(\theta_{\mathrm{L}}) \approx 0$, $R''_{\mathrm{int}}(\theta_{\mathrm{H}}) \approx 0$ and $R'_{\mathrm{int}}(\theta_{\mathrm{TOP}}) \approx 0$) it is possible to obtain attenuation, broadening and refraction [69, 88]. This latter method is called extended DEI (E-DEI).

W-DEI

Many features of scattering patterns appear often at angles much larger than the width of the central peak, and E-DEI is not able to see these changes. We introduce a wide-angle DEI (W-DEI) to analyze specifically scattering coming at wider angles. It is based on E-DEI and uses a total of 5 analyzer angles, giving in addition the intensity change at distance θ_{W} away from the central peak. The value of θ_{W} is selected so that it is well beyond the central width of the RC and larger than any refraction angles, so that we get a true dark field image and see only the contribution of scattering. If *a priori* knowledge on the position of some scattering peak exists, θ_{W} can be selected to further match the position of the peak.

The regular E-DEI using 3 points is used to calculate the refraction angle ($\Delta\theta_z$), central peak broadening (σ_{scat}), and attenuation ($e^{-\mu_{\mathrm{attn}}T}$). To calculate RC value at distance θ_{W} from the peak position, we use the average of values measured at $-\theta_{\mathrm{W}}$ and $+\theta_{\mathrm{W}}$,

$$R(\theta_{\mathrm{W}} + \Delta\theta_z) = \frac{R(-\theta_{\mathrm{W}}) + R(+\theta_{\mathrm{W}})}{2}. \tag{3.13}$$

In this we have assumed that the RC is symmetric. When $\Delta\theta_z \neq 0$, the measured value is not exact, but an average of the values $\Delta\theta_z$ above and below the actual position θ_W, corresponding to linear interpolation from these two values.

If there is no scattering, the only change to the RC value at distance θ_{W} from the peak comes from attenuation. The fraction of scattering (compared to the central peak height) at distance θ_{W} from the peak can then be estimated by subtracting from the measured value an expected value based on the assumption that only attenuation was present. We define the wide[a] angle scattering parameter as

$$\gamma_{\mathrm{W}} = \frac{R(\theta_{\mathrm{W}} + \Delta\theta_z) - e^{-\mu_{\mathrm{attn}}T} R_{\mathrm{int}}(\theta_{\mathrm{W}})}{e^{-\mu_{\mathrm{attn}}T} R_{\mathrm{int}}(0)} \approx \frac{R(\theta_{\mathrm{W}} + \Delta\theta_z)}{e^{-\mu_{\mathrm{attn}}T} R_{\mathrm{int}}(0)}. \tag{3.14}$$

[a] Here 'wide' refers to wide in the context of RC, i.e. above a few microradians.

Here the last equality is valid if the angle θ_{W} is large so that the intrinsic intensity at that angle is negligible.

The value of γ_{W} depends on the total fraction of scattering $(1-\xi)$ and on the scattering function $F(\theta_x, \theta_z)$, so that it is sensitive to changes in both. On the other hand, via γ_{W} it is not possible to determine which of these scattering related parameters has changed. Therefore γ_{W} can be seen as a means of obtaining contrast in situations where changes in the scattering are expected, but does not give quantitative information about the scattering properties.

RC Central Moments

Another approach is to base the analysis of the RC shape on the central moments of the RC [66, 67, 89]. Measurements at multiple rocking angles around the zero position are needed, so that this method is also called multiple image radiography (MIR), which is the term we adopt to describe the method based on the central moments. The n^{th} central moment of the RC is

$$M_n = \sum_{\mathrm{i}} R(\theta_{\mathrm{i}}) \theta_{\mathrm{i}}^n \nu_{\mathrm{i}}, \tag{3.15}$$

where ν_{i} is a weighting factor that takes into account that the angles θ_{i} might not be evenly spread. From the central moments, several parameters relating to the shape of the RC can be extracted [89]

$$e^{-\mu_{\mathrm{attn}} T} = M_0 / M_{0,\mathrm{int}} \tag{3.16}$$

$$\Delta\theta_z = M_1 / M_0 \tag{3.17}$$

$$\sigma_{\mathrm{RC}} = \sqrt{M_2/M_0 - \theta_0^2}. \tag{3.18}$$

The width parameter σ_{RC} measures the width of the RC, including both the scattered component and the direct beam. Therefore the value depends on not only the scattering width, but also on the scattering fraction.

RC Parametrized Function Fits

By following (3.11) the RC can be presented as a sum of the intrinsic RC (which can be measured accurately) and a function $F(\theta)$ describing the scattered intensity after lateral integration. This allows quantification of the fraction of scattering $(1-\xi)$ and the width of scattering as separate effects. The intensity in (3.11) is convolved with the intrinsic RC to get the intensity profile seen at the detector

$$\begin{aligned} R(\theta_{\mathrm{R}}) = {} & e^{-\mu T} \xi R_{\mathrm{int}}(\theta_{\mathrm{R}} - \Delta\theta_z) + \\ & e^{-\mu T}(1-\xi) \textstyle\int_{-\infty}^{\infty} F(\theta) \times R_{\mathrm{int}}(\theta - (\theta_{\mathrm{R}} - \Delta\theta_z)) \mathrm{d}\theta. \end{aligned} \tag{3.19}$$

Here $\Delta\theta_z$ is the refraction angle in the vertical direction and θ_{R} is the rocking angle.

In the simplest case $F(\theta)$ is assumed to be Gaussian with the standard deviation σ_{scat}, so that

$$F(\theta) = \frac{1}{\sqrt{2\pi}\sigma_{\mathrm{scat}}} \exp\left[-\frac{\theta^2}{2\sigma_{\mathrm{scat}}^2}\right]. \tag{3.20}$$

By comparing (3.19) to the actual measured curve, the optimal values for the four parameters ($e^{-\mu T}, \xi, \sigma_{\mathrm{scat}}$ and $\Delta\theta_z$) are resolved by numerical optimization. It is noteworthy that in this case the resolved σ_{scat} is proportional to the width of $F(\theta)$ with the effect of scattering fraction separated to parameter ξ.

A more versatile approach is to use the sum of a Gaussian and a Lorentzian function, the so called pseudo-Voigtian (pV), for the scattering [90],

$$F(\theta) = \eta \mathrm{G}(\theta) + (1-\eta)\mathrm{L}(\theta), \tag{3.21}$$

where $\mathrm{G}(\theta)$ is a Gaussian function and $\mathrm{L}(\theta)$ is a Lorentzian. The shape of the pV is controlled by the mixing parameter η and the FWHM that sets the widths of both G and L. This type of function has the advantage that in addition to central broadening, depicted by the Gaussian, the intensity coming into higher angles can be taken into account via the Lorentzian that has long tails. Now there are five parameters ($e^{-\mu T}, \xi, \sigma_{\mathrm{scat}}, \Delta\theta_z$ and η) to resolve when (3.19) is optimized numerically. The parameter η contains information about the contribution of the tails of the RC. However, it is reported in [90] that η is rather sensitive to noise in the images.

3.4.2 Noise and Properties of W-DEI

In addition to sources of noise discussed in section 3.2 the uncertainty and oscillations in the analyzer crystal position add to the noise level in the ABI images. The effect of different types of noise on the SNR as a function of the rocking angle is illustrated in figure 3.7. The SNR is at maximum at the peak of the rocking curve, and decreases in the flanks as the photon counts decrease. A constant background has also a large effect in the flanks where the photon counts are low. Oscillations of the analyzer crystal cause larger effect near the center of the RC, where the reflectivity changes rapidly. In this section we analyze the properties of W-DEI and how the method behaves in the presence of noise.

Figure 3.8 shows how the scattering parameter γ_{W} behaves for different combinations of σ_{scat} and the scattering fraction $1-\xi$. The RC is modeled using the Gaussian approximation of scattering as in (3.20). Parameter γ_{W} clearly depends on both the scattering fraction and $F(\theta)$, so that it does not give quantitative information on either. However, γ_{W} may still give good contrast for changes in either the scattering width or the scattering fraction.

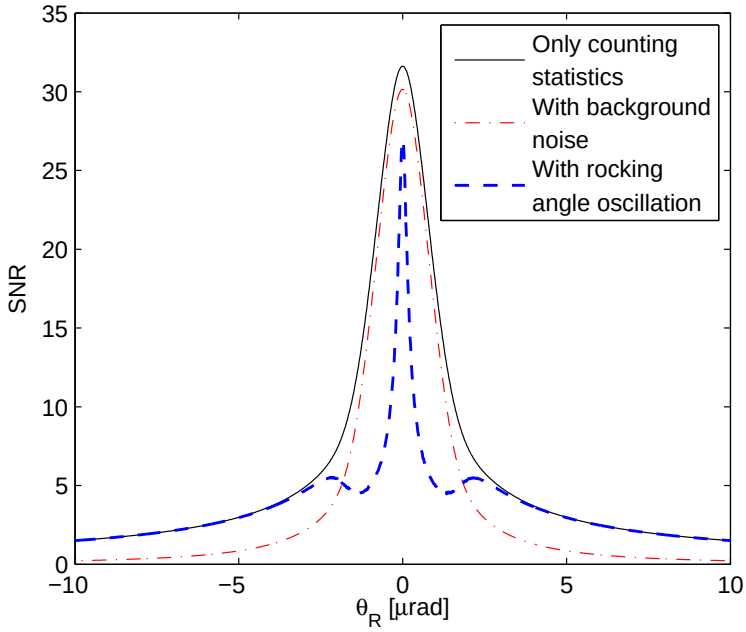

Figure 3.7: Signal-to-noise ratio at different parts of the rocking curve for a single detector pixel. The number of incoming photons per analyzer position is $N_0 = 1000$, and the average number of recorded photons at angle θ_{R} is $R(\theta_R)N_0$. The solid line corresponds to the SNR limited by photon noise. The dash-dotted curve corresponds to the case with an additional background (independent of θ_R) of 100 photons per rocking angle on the average. The dashed line corresponds to the case where crystal vibrations cause the rocking angle to have an uncertainty (Gaussian distribution, $\sigma = 0.1$ $\mu\mathrm{rad}$).

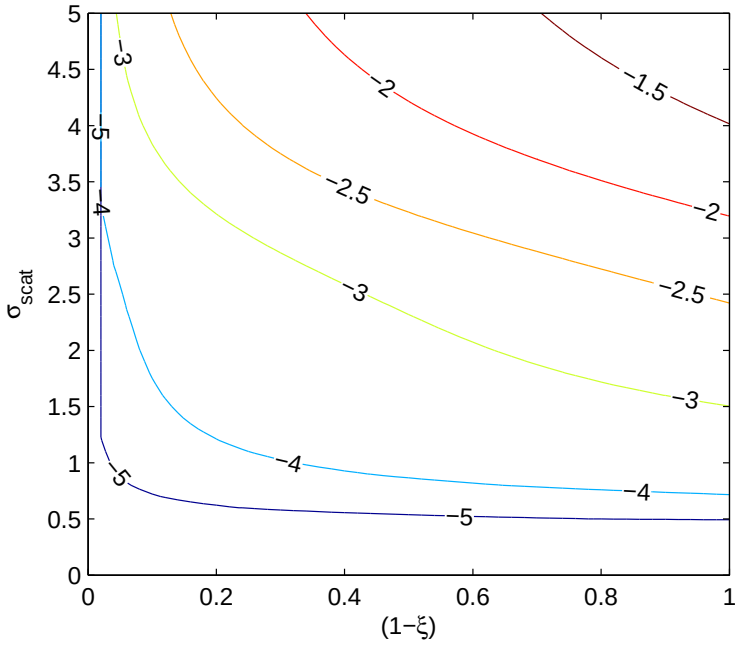

Figure 3.8: Value of $\log_{10}\gamma_{\mathrm{W}}$ as a function of σ_{scat} and ξ.

The value of γ_{W} may depend on the refraction angle because the points $-\theta_{\mathrm{W}}$ and $+\theta_{\mathrm{W}}$ sample the RC at different locations depending on how large $\Delta\theta_z$ is. The linear interpolation in (3.13) is only an approximation, and this is a source of error when $\Delta\theta_z$ is not zero. The effect of refraction angle on the determined value of γ_{W} is shown in figure 3.9 for different values of ξ for the case of Gaussian scattering with the standard deviation of 2 µrad. The effect of $\Delta\theta_z$ is rather small, indicating that γ_{W} may serve as a good indicator of scattering even in the presence of refraction.

The parameter γ_{W} in W-DEI is measured at the flanks of the RC where the intensities are low, so that the noise in the background has potentially the most severe effect from the point of view of W-DEI (cf. figure 3.7). However, the effect of counting statistics is more fundamental than the crystal vibrations or the background noise in that it cannot be eliminated even with perfect instrumentation. We analyze the situation where the background level and crystal vibrations have been essentially eliminated through careful instrumentation. Figure 3.10 shows how repeatably γ_{W} can be determined for a varying number of incoming photons. It can be seen that the variation of γ_{W} diminishes quite rapidly as the number of photons increases, and a good level of accuracy is reached with a reasonable number of incoming photons.

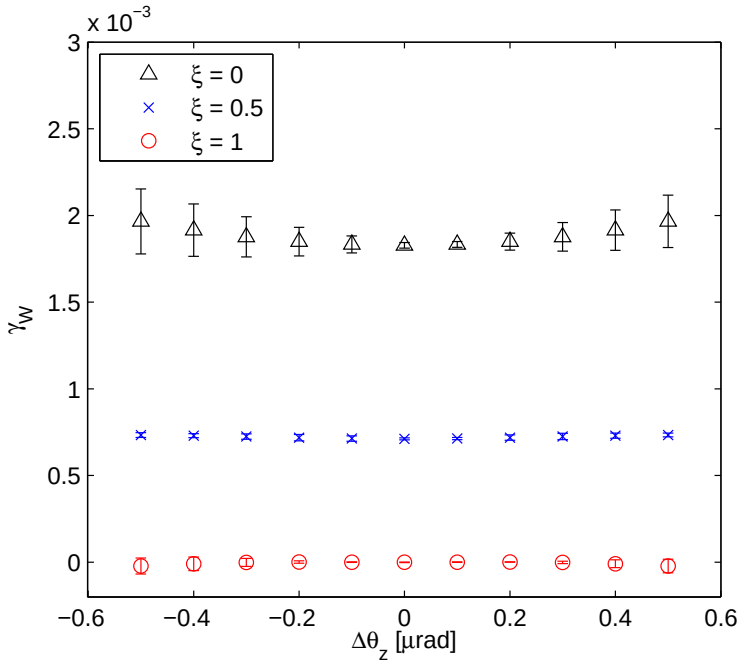

Figure 3.9: Value of γ_{W} as a function of $\Delta\theta_z$ for different values of ξ. The scattering is Gaussian with the standard deviation $\sigma_{\mathrm{scat}} = 2\,\mu\mathrm{rad}$. The error bars correspond to uncertainty of γ_W if the uncertainty of $\Delta\theta_z$ has the standard deviation of $0.3\,\mu\mathrm{rad}$.

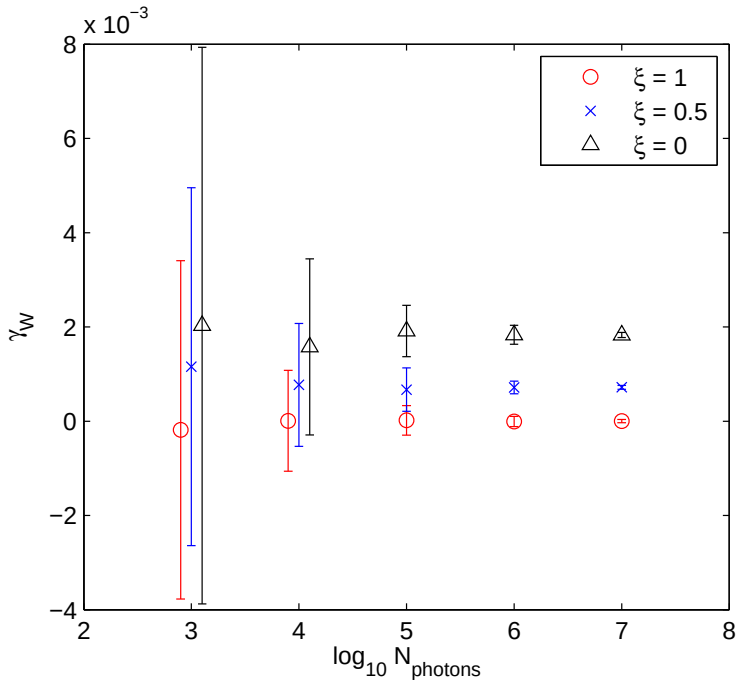

Figure 3.10: Behaviour of γ_{W} as a function of the number of incoming photons N_{photons}. For each of the 5 analyzer angles $N_{\mathrm{photons}}/5$ incoming photons were used. Some of the values have been slightly displaced horizontally for clarity. The scattering is Gaussian with the standard deviation $\sigma_{\mathrm{scat}} = 2\,\mu\mathrm{rad}$.

3.4.3 CT Reconstruction of ABI Images

As already discussed in section 3.3, CT reconstruction is possible for quantities that are line integrals of some property of the sample. Reconstructing the scattering profile for each voxel is possible if the single scattering approximation is valid, because in this case the scattering pattern is a line integral of the sample. Therefore scattering into each angle can be reconstructed independently. However, the contribution of multiple scattering is not compatible with the line integral property, because in this case the scattering into a given angle may still be scattered into some other angle, and the total scattering pattern is not simply a sum of the different scattering patterns arising along the path of the beam.

Figure 3.11 shows an example of reconstructed scattering signal for a computational phantom consisting of cylindrical background and six details. Scattering produces a wide central peak and a sharp side peak at some distance from the center. The scattering fraction, central peak width, and the side peak position differ between the details and the background. We observe that it is possible to reconstruct the scattering with reasonable accuracy. However, there is some variation in the reconstructed intensity even in the areas where the intensity should be constant, as seen in figure 3.11(c). This artefact is due to multiple scattering, and disappears when the scattering fraction is sufficiently small.

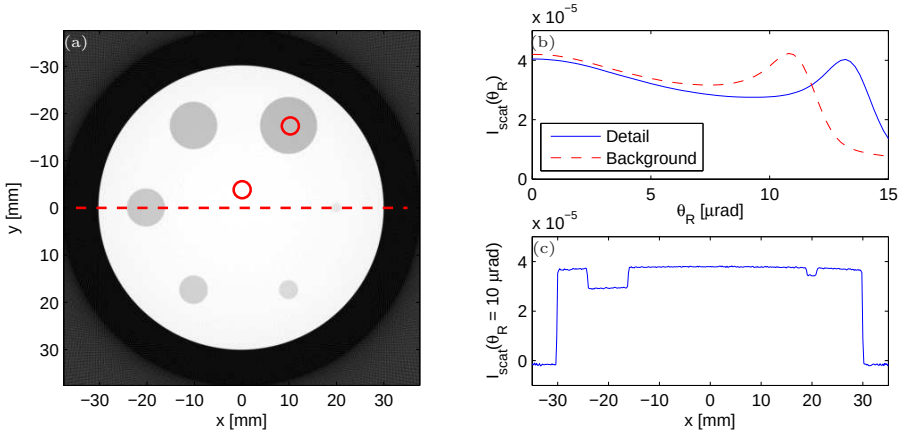

Figure 3.11: Example of reconstructed scattering into the angle $\theta_{\mathrm{R}} = 10\,\mu\mathrm{rad}$ (a). Scattering profiles from a detail and the background (b) from the positions marked with circles in (a). Intensity in the horizontal profile, dashed horizontal line in (a), at $\theta_{\mathrm{R}} = 10\,\mu\mathrm{rad}$ (c). Total scattering fraction was 16.5% at the thickest position of the background.

Instead of reconstructing the full scattering profile, it is possible to first extract some parameters of the profile, and then reconstruct the spatial

variation of these parameters. It has been shown analytically that the parameters obtained in the MIR method are to good accuracy line integrals of specific sample properties under the assumption of small angle scattering and Gaussian scattering function [67]. Therefore CT images based on these quantities can be reconstructed using standard CT algorithms, resulting in attenuation coefficient, refractive index gradient, and USAXS parameter maps. The reconstruction of such parameters is computationally more efficient than doing the reconstruction for each scattering angle separately.

Figure 3.12 shows examples of reconstructed parameters for the computational phantom. All of the parameters presented are able to differentiate the details from the background. Especially ξ and γ_{W} produce clear results. There are considerable reconstruction artefacts present in the σ_{scat} calculated with E-DEI. E-DEI considers the slope of the measured rocking curve, and when the RC is a combination of the direct and the scattered beams, the slope does not change linearly with the addition of scattering (for ξ close to 1 the slope is essentially unchanged from the intrinsic one, and for ξ close to zero the slope is determined by the scattering). The σ_{scat} calculated with MIR suffers from artefacts to a lesser extent, the main contribution coming from the fact that the scattering pattern has Lorenzian tails.

Although in many cases it could be useful to reconstruct the whole scattering signal, it may not be possible to do it in practice due to limited photon statistics arising from dose considerations. To obtain good statistics in scattering, the optimal sample should have a large scattering fraction. However, this is just the case that gives the largest artefacts in the reconstruction of the scattering signal. Therefore, extraction of parameters before the reconstruction may be the best approach in practice. Another possibility that has been suggested is to model the scattering pattern as a linear combination of a few well known basis scattering patterns, and then to reconstruct the spatial distribution of the weighting factors for the different scattering patterns [91].

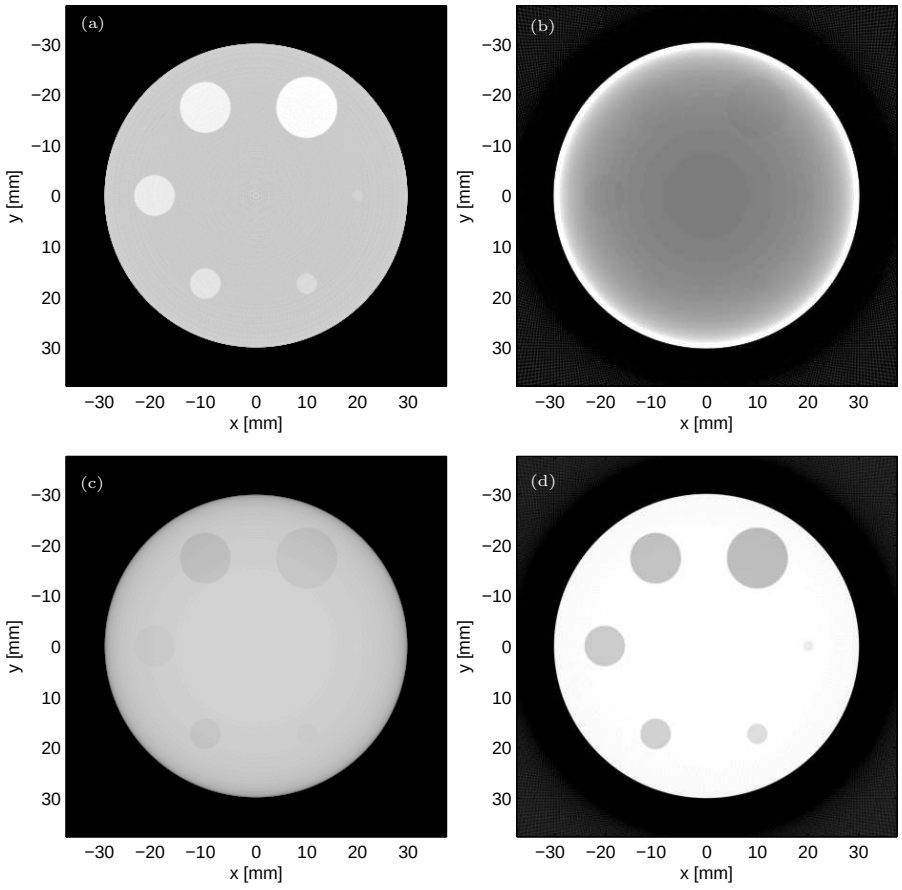

Figure 3.12: Reconstructed parameter maps for the computational phantom. Mixing parameter ξ (a), σ_{scat} from E-DEI (b), σ_{scat} from MIR (c), and γ_{W} (d). The limits for the gray scale values have been manually adjusted in order to show a good dynamic range.

Chapter 4

Elastic Small-Angle X-Ray Scattering

As seen in section 2.2.2 the atomic scattering factor is the Fourier transform of the electron density of the atom. In the single scattering approximation the same formalism can be expanded to larger structures so that the scattered amplitude from an arbitrary structure is a Fourier transform of the electron density. The electron density could then be reconstructed if the scattered amplitude and the phase could somehow be measured. In fact, only the intensity can be measured, and the electron density cannot be reconstructed by direct inverse Fourier transform. Instead, a commonly used approach for solving the structure of the scattering object is to calculate the scattered intensity for an approximation of the structure, and to iteratively refine the structure so that the calculated scattering profile resembles the measured one as closely as possible. For large objects two additional factors have to be taken into account: the finite coherence length of the beam and multiple scattering. Both of these factors tend to wash out the features of the scattering pattern, further complicating the analysis.

In this section we deal with the calculation of scattering patterns to see what types of intensity distributions can be expected at the detector and how these relate to the structure of the sample. We concentrate on small-angle x-ray scattering (SAXS), and also deal with the related phenomenon of multiple refraction. Experimental SAXS patterns from breast tissue samples are presented. The purpose is to get a realistic idea of what scattering from breast tissue looks like, so that this can be used in chapter 5 when the visibility of changes in scattering in ABI is evaluated.

4.1 Scattering Calculations

The scattered amplitudes from different parts of the sample interfere to form the scattering pattern. The observed quantity however is the intensity,

and the structure of the sample cannot in general be solved directly with the inverse Fourier transform. Using a model for the sample with a set of variable parameters allows calculated intensities to be compared with the measured intensity for the purpose of optimizing model parameters. This approach is commonly used especially for SAXS measurements. In addition to solving structures via scattering calculations, the calculations give insights into how different properties of the sample affect the scattering patterns.

4.1.1 Calculation of Phase Differences

Calculation of phase differences for waves scattered from different locations within the sample is at the heart of the scattering calculations. What approximations can be used depends somewhat on how large is the distance between the scattering object and the detector (and also the distance between the source and the sample [92]). Two different cases can be distinguished: near field scattering (Fresnel) and far field scattering (Fraunhofer). Figure 4.1 shows waves coming from points P_1 and P_2 to point D on the detector. Using the notation of figure 4.1, the path length difference for the two waves is

$$\Delta l = l_2 - l_1 = \sqrt{l_0^2 + (\Delta y + d)^2} - \sqrt{l_0^2 + \Delta y^2} \tag{4.1}$$

Expanding the square roots in Taylor series, we find that

$$\Delta l = \frac{\Delta y}{l_0} d - \frac{d^2}{2l_0} + \mathcal{O}\left(d\left(\frac{d}{l_0}\right)^3\right) + \mathcal{O}\left(\Delta y\left(\frac{\Delta y}{l_0}\right)^3\right). \tag{4.2}$$

The first term on the right hand side is the difference in path length in the Fraunhofer case, $\Delta l = d \sin 2\theta$. The second term is a correction that becomes important when the angular size, $\alpha_s = d/l_0$, of the scattering object as seen from the detector approaches or exceeds the scattering angle 2θ. The remaining terms are negligible as long as $d \ll l_0$ and $\Delta y \ll l_0$, which almost always is the case in practice. Therefore we can conclude that the Fraunhofer approximation is valid whenever $2\theta \gg d/l_0$. The phase difference is calculated from the path difference as

$$\Delta\phi = 2\pi \frac{\Delta l}{\lambda}. \tag{4.3}$$

In the x-ray regime the size of the coherently scattering volume is typically only some micrometres (cf. 2.1.2), and therefore the angular size of the coherently scattering volume as seen from the detector is typically only a few microradians. Therefore the Fraunhofer approximation is valid almost universally in x-ray experiments. However, when the scattering angle is only a few microradians we may need to calculate the phase difference more accurately using (4.1) [51, pp. 142–145]. The Fresnel approach is also

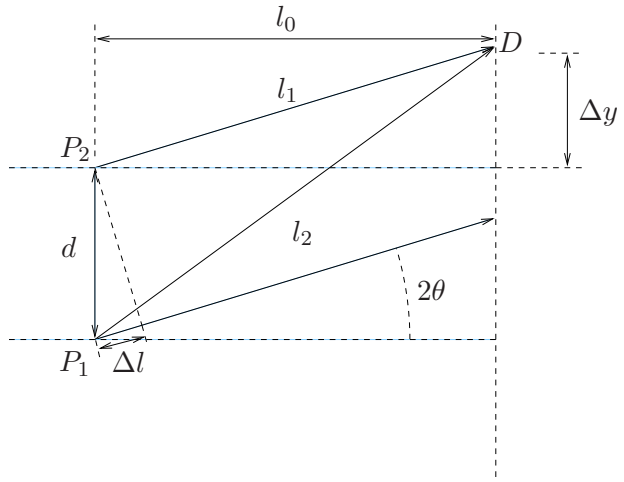

Figure 4.1: Geometry used in the phase difference calculation.

needed if the source is close to the object, but we assume this not to be the case [92, p. 188].

In the Fraunhofer case the phase difference for waves scattered from two locations in the sample, separated by vector $\mathbf{r}$, is [30]

$$\Delta\phi = 2\pi \mathbf{s} \cdot \mathbf{r}, \tag{4.4}$$

where $\mathbf{s}$ is the scattering vector (c.f. section 2.2.2). The scattering vector $\mathbf{s}$ can also be defined with angles 2θ and ϕ as shown in figure 4.2 using the identities

$$\begin{aligned} s_x &= s\cos\theta\cos\phi \\ s_y &= s\sin\theta \\ s_z &= s\cos\theta\sin\phi. \end{aligned} \tag{4.5}$$

Putting the components of $\mathbf{s}$ (4.5) into (4.4) gives

$$\Delta\phi = 2\pi s(x\cos\theta\cos\phi + y\sin\theta + z\cos\theta\sin\phi), \tag{4.6}$$

where $\mathbf{r} = (x, y, z)$. For small angles $\theta \ll 1$ we can use approximations $\cos\theta \approx 1$, $\sin\theta \approx \theta$, so that the phase becomes

$$\Delta\phi \approx 2\pi s(x\cos\phi + y\theta + z\sin\phi). \tag{4.7}$$

We see that when θ is small, the y-component of the coordinate contributes only a little to the phase, and can be ignored in most cases of small-angle scattering.

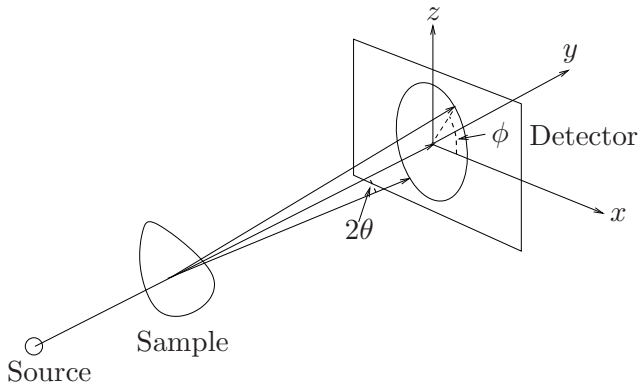

Figure 4.2: A schematic figure showing the angles used to define the direction of scattering. The choice of the coordinate system is also shown.

4.1.2 Summation of Amplitudes

When the phase $\phi(\mathbf{r}, \mathbf{s})$ and the electron density $\rho(\mathbf{r})$ for each point in the sample are known, the singly scattered amplitude for perfectly coherent incoming beam can be calculated as

$$A(\mathbf{s}) = r_e \int_V A_0(\mathbf{r})\rho(\mathbf{r}) \exp[-i\phi(\mathbf{r}, \mathbf{s})] \mathrm{d}^3\mathbf{r}. \tag{4.8}$$

Here $A_0(\mathbf{r})$ is the amplitude of the incoming beam, which from now on will be assumed to be unity except when stated otherwise. The quantity $\rho(\mathbf{r})\mathrm{d}^3\mathbf{r}$ is the amount of charge in a differential volume element around $\mathbf{r}$. The scattering amplitude (4.8) can then be understood as a sum of the individual amplitudes from these differential scattering volumes. In the case of Fraunhofer scattering, the phase is $2\pi\mathbf{s} \cdot \mathbf{r}$, and the calculated amplitude is the Fourier transform of the electron density.

Integration of equation (4.8) analytically is only possible for some special types of the electron density $\rho(\mathbf{r})$, usually simple geometrical shapes, and even then only when the Fraunhofer approximation is valid [93]. In other cases, (4.8) has to be integrated numerically. One approach is to sample the electron density at a discrete set of points $\mathbf{r}_\mathrm{j}$, e.g. on a cubic lattice or randomly selected points, and sum the scattered amplitudes from each point,

$$A(\mathbf{s}) = r_e \sum_\mathrm{j} \rho(\mathbf{r}_\mathrm{j}) \exp[-i\phi(\mathbf{r}_\mathrm{j}, \mathbf{s})] \Delta V, \tag{4.9}$$

where $\Delta V = V/N$ is the volume of the scattering element, V is the volume of the sample, and N is the number of discrete scattering elements. When ΔV is small enough, the result approaches that of (4.8).

For small scattering angles $\phi(\mathbf{r}_\mathrm{j}, \mathbf{s})$ changes slowly as a function of $\mathbf{r}_\mathrm{j}$ and therefore rather large ΔV can be used. Especially, for $|\mathbf{s}| \to 0$ only

the average electron density contributes to the signal. For larger scattering angles $\phi(\mathbf{r}_\mathrm{j}, \mathbf{s})$ oscillates faster, and a smaller ΔV needs to be used. For large scattering angles, however, the oscillations from large distances are so rapid that they are washed out by the detector PSF or lack of coherence (cf. 4.1.3), and a smaller V can be used. This allows the possibility that the scattering patterns can be calculated by keeping a constant N and varying ΔV and V as a function of s.

In the Fraunhofer case in the SAXS regime, the y-component of the coordinate contributes only a little to the phase as was already mentioned. It is then possible to ignore the variation of phase with y, and use projection of the electron density. Using (4.7) the scattered amplitude (4.8) then becomes

$$A(s,\phi) = r_e \int_{-\infty}^{\infty}\int_{-\infty}^{\infty} \rho_y(x,z)\exp[-i2\pi s(x\cos\phi + z\sin\phi)]\mathrm{d}x\mathrm{d}z, \quad (4.10)$$

where

$$\rho_y(x,z) = \int_{-\infty}^{\infty} \rho(x,y,z)\mathrm{d}y. \quad (4.11)$$

The projection method is useful because it allows integration in the y-direction to be independent of s, therefore speeding the calculation when done numerically, e.g. using (4.9).

In some cases we can divide the scattering object to sub-objects that are large enough to have some structure in their scattering patterns in the angular regime of interest. For an object composed of N sub-objects having amplitudes $A_\mathrm{j}(\mathbf{s})$ and positions $\mathbf{r}_\mathrm{j}$ the scattered amplitude is

$$A(\mathbf{s}) = \sum_{j=1}^{N} A_\mathrm{j}(\mathbf{s})\exp[-i\phi(\mathbf{r}_\mathrm{j}, \mathbf{s})]. \quad (4.12)$$

As a special case of (4.12) when $A_\mathrm{j}(\mathbf{s}) = A_\mathrm{i}(\mathbf{s}), \forall \mathrm{i},\mathrm{j}$ we can divide the amplitude to be a product of the amplitude from a single object and the interference term resulting from the packing

$$A(\mathbf{s}) = A_1(\mathbf{s}) \overbrace{\sum_{j=0}^{N} \exp[-i\phi(\mathbf{r}_\mathrm{j}, \mathbf{s})]}^{\text{interference}}. \quad (4.13)$$

This can be used to test different packings when the structure of the objects is well known, but their packing is unclear.

4.1.3 Termination, Coherence and Speckle

When the scattering amplitudes (and from there the intensities) are calculated using e.g. (4.12), there will be rapid oscillations in the results corresponding to the largest interparticle distances in the sample. In real experiments these rapid oscillations are not usually seen even though the sample size may be quite large.

Because all detectors have a PSF of finite width, they will average the intensity over a small spatial region, causing averaging in the s-space. Rapid oscillations of intensity disappear in this averaging process. Therefore it is impossible to observe oscillations from objects placed far enough from each other. The observed intensity from such objects is just the sum of the individual intensities. Figure 4.3 shows the interference from two objects placed at different distances from each other and how the interferences disappear when averaged in the s-space. We see that at small R the oscillations are not much affected, but at larger R they are greatly diminished. It is important to note that the averaged quantity here is the intensity, not the amplitude.

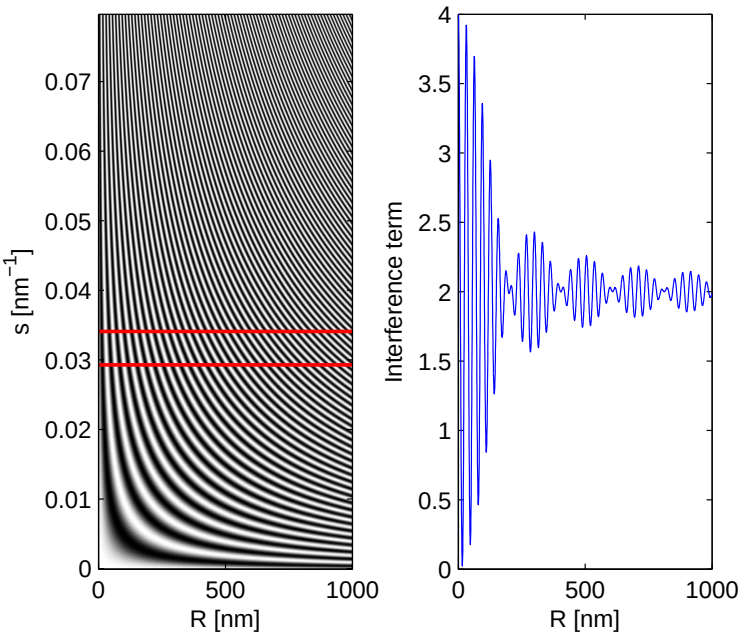

Figure 4.3: Interference from two objects at different distance R from each other (left). On the right an example of the oscillations when averaged in s-space between 0.030 $\mathrm{nm}^{-1}$and 0.035 nm^{-1}(shown as the horizontal lines in the left panel). This averaging correspond to the detector having a square PSF with the width of 0.6 mm at 1 m distance from the sample, when using 10 keV radiation.

The coherence of the beam, i.e. the apparent source size and the energy bandwidth, affect also how well the interferences between different scatterers are visible. Both of these factors cause averaging in the s-space (much like the PSF), and therefore wash out rapid oscillations, i.e. interferences from objects at large distances. The coherence of the beam and the properties of the detector can be combined to give a generalized coherence volume that describes the largest volume that still gives a good interference pattern [17].

The relative size of the coherence volume compared to the illuminated sample volume has a role in how the scattered intensity is to be calculated. Figure 4.4 shows the different possibilities of coherence and illuminated volume compared to the sample size. Each of these possibilities leads to different results in the scattering. For most of the scattering in ABI the case of small coherence volume is of interest. We however start from dealing with the completely coherent case to see how the loss of coherence can be taken into account in the calculation of the scattering patterns.

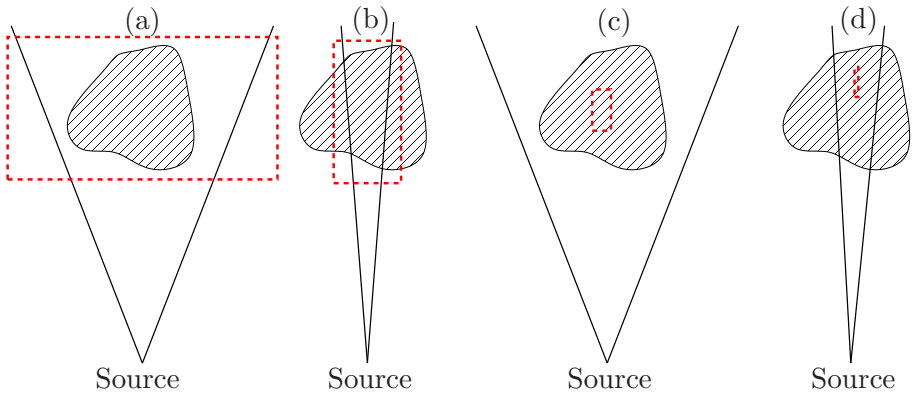

Figure 4.4: Different possibilities for the size of the irradiated volume (thick lines), sample (hatched area) and coherence volume (dashed rectangles).

The case where the sample size is small compared to both the beam size and the coherence length is the easiest one to deal with computationally. It is essentially described by (4.8) by setting $A_0(\mathbf{r}) = 1$, and shown in figure 4.4 (a). In this case scattering from all points within the sample is completely coherent, and speckle patterns can be observed. From such a speckle pattern it is possible to do complete reconstruction of the electron density of the scattering object, and to effectively solve the phase problem of x-ray scattering [20, 94–96]. Figure 4.5 shows the speckle pattern from a single object composed of spheres. The speckle pattern is seen superimposed on the concentric rings produced by the spheres.

The next case to be considered is that of fully coherent beam of finite extent (figure 4.4 (b)). This means that the incoming amplitude $A_0(\mathbf{r})$ goes to zero or diminishes significantly within the sample. In equation (4.8) the incoming amplitude multiplies the electron density $\rho(\mathbf{r})$. In the Fraunhofer case the scattered amplitude is just the Fourier transform of $A_0(\mathbf{r})\rho(\mathbf{r})$, and according to the convolution theorem [97, ch. 15.5], the result is given by the convolution of the individual Fourier transforms. Therefore the scattered amplitude becomes

$$A(\mathbf{s}) = \widetilde{A_0}(\mathbf{s}) \circledast \widetilde{A_{\text{inf}}}(\mathbf{s}), \tag{4.14}$$

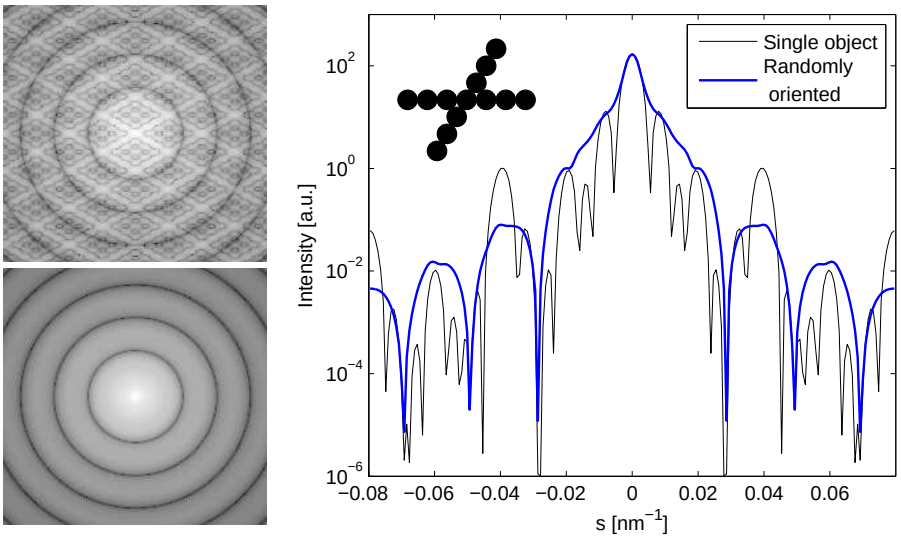

Figure 4.5: Scattering from a single object with coherent beam (top), and from multiple rotationally averaged objects where the different objects scatter independently (bottom). The right panel shows the scattering object that was used (an X composed of spheres with 50 nm diameter) and the horizontal intensity profiles going through the middle of the scattering patterns.

where $\widetilde{A_0}(\mathbf{s})$ is the Fourier transform of the incoming amplitude, and $\widetilde{A_{\mathrm{inf}}}(\mathbf{s})$ is the scattered amplitude in the case when $A_0(\mathbf{s}) = 1$.

For a Gaussian beam with the standard deviation σ the Fourier transform is also a Gaussian with the standard deviation $1/\sigma$. For an aperture limited beam the beam profile is a box-function with the width L_b, and the Fourier transform is a sinc-function with the period length $2/L_b$. Convolution with these functions smooths out the features of the scattering pattern.

In the cases shown in figure 4.4 (c) and (d), the size of the coherence volume is significantly smaller than the irradiated sample volume. This type of partial coherence is usual in x-ray experiments, and calculation of intensities requires a different approach than in the totally coherent case. Scattering coming from location at $\mathbf{r}_0$ interferes coherently only up to a certain limiting distance R_{limit}. Coherence can be described by a coherence function $\gamma(\mathbf{r})$ [19, 98, 99], which for a source with small angular size is a Gaussian with $\gamma(0) = 1$ [19]. Scattering centered on atom at $\mathbf{r}_0$ interferes with scattering only from atoms at locations $\mathbf{r}$ that are sufficiently close to $\mathbf{r}_0$ so that $\gamma(\mathbf{r} - \mathbf{r}_0) > 0$. The scattered intensity from an object can then be calculated as [19]

$$I(\mathbf{s}) = \int_{V_1}\int_{V_2} \gamma(|\mathbf{r}_1 - \mathbf{r}_2|)A(\mathbf{r}_1, \mathbf{s})A^*(\mathbf{r}_2, \mathbf{s})\mathrm{d}V_1\mathrm{d}V_2. \tag{4.15}$$

Equation (4.15) involves a double integral over the sample volume, so that calculation of intensity is essentially computationally more demanding when partial coherence is involved than in the completely coherent case.

4.1.4 Rotationally Averaged Systems

When the scattering objects are all identical, consisting of N spherically symmetric scattering units with the scattering factors f_{i}, in random orientations and scattering independently, the intensity is calculated by averaging the intensities coming from different orientations. In the method developed by Debye [100] the intensity is calculated based on the interatomic distances d_{ij} and the atomic scattering factors f_{i} as

$$I(s) = \sum_{\mathrm{i}=1}^{N}\sum_{\mathrm{j}=1}^{N} f_{\mathrm{i}}(s)f_{\mathrm{j}}^*(s)\frac{\sin sd_{\mathrm{ij}}}{sd_{\mathrm{ij}}}. \tag{4.16}$$

Being rotationally averaged, the intensity depends only on the magnitude $s = |\mathbf{s}|$ of the scattering vector and not on the direction. The scattering units do not need to be atoms, but the object can be divided to any spherical subunits, which makes possible to model the scattering object at the desired level of accuracy.

If N is large the computation of scattering profile using (4.16) becomes very time consuming, consisting of about N^2 calculations of $\sin(sd)$ for each

value of s. By discretizing the distances d_{ij} and using a distance histogram $H(d_{\mathrm{i}})$ the computational demand can be reduced considerably [101, 102]. In this case we however have to assume that the scattering factors f_{i} are identical for all the scattering units. This histogram method requires still N^2 operations for calculating the distances, but now this only has to be done once instead of separately for each value of s. The intensity can then be calculated as

$$I(s) = f(s)^2 \sum_{\mathrm{i}=1}^{N_{\mathrm{bins}}} H(d_{\mathrm{i}}) \frac{\sin sd_{\mathrm{i}}}{sd_{\mathrm{i}}}. \tag{4.17}$$

In equation (4.17) some generality has been lost compared to (4.16) because all the scatterers have to be identical. One method to overcome this difficulty is to separate the pairwise histogram into separate histograms between each different scatterer type [102]. This leads to calculation of partial structure factors, whose weighted sum is the total scattering. This works well when the number of different scatterers is small, which is often the case when modeling biological molecules at the atomic level.

In the small-angle regime the scattering factors $f_{\mathrm{i}}(s)$ can be thought to be largely independent of s. In this case instead of just storing the number of pairs in the distance range $[d_{\mathrm{i}}, d_{\mathrm{i}} + \Delta d[$ we can store the sum of $f_{\mathrm{i}} f_{\mathrm{j}}$ for all pairs whose distace is in this range. For this purpose we introduce the pairwise structure factor histogram

$$g(d_{\mathrm{i}}) = \sum_{\mathrm{m,n}} f_{\mathrm{m}} f_{\mathrm{n}} \sigma_{\mathrm{mn}}(d_{\mathrm{i}}), \tag{4.18}$$

where

$$\sigma_{\mathrm{mn}}(d_{\mathrm{i}}) = \begin{cases} 1, \text{if } d_{\mathrm{mn}} \in [d_{\mathrm{i}}, d_{\mathrm{i}} + \Delta d[\\ 0, \text{otherwise.} \end{cases} \tag{4.19}$$

From $g(d_{\mathrm{i}})$ the intensity can be calculated as

$$I(s) = \sum_{\mathrm{i}=1}^{N_{\mathrm{bins}}} g(d_{\mathrm{i}}) \frac{\sin sd_{\mathrm{i}}}{sd_{\mathrm{i}}}. \tag{4.20}$$

Equation (4.20) has advantage over (4.17) in that the scatterers do not have to be identical, but still having the same advantage over (4.16) that N^2 distances have to be calculated only once and not for each value of s. Compared to the partial structure factor method this is more practical in cases when the number of different scatterer types is large. This can be the case when the electron density is modeled as a smooth continuous function that is then discretized, rather than using discrete atoms as the scattering units.

In some cases the scattering objects are oriented along a common axis, but randomly rotated about this axis. If the scattering pattern of each

individual object is axially symmetric, and the locations of the scattering objects are $\mathbf{r}_\mathrm{i}$, scattering in the plane perpendicular to the symmetry axis (scattering plane) can be calculated as [103]

$$I_\mathrm{eq}(s) = \sum_{\mathrm{i}=1}^{\mathrm{N}} \sum_{\mathrm{j}=1}^{\mathrm{N}} f_\mathrm{i}(s) f_\mathrm{j}(s) \mathrm{J}_0(s d_\mathrm{ij}). \tag{4.21}$$

Here d_ij is the distance of the scatterers in the scattering plane and J_0 is the zeroth order Bessel function of the first kind [97, ch. 11]. Scattering in the plane perpendicular to the symmetry axis is called equatorial scattering.

The distance histogram methods work here as well, and the intensity can be calculated as

$$I_\mathrm{eq}(s) = f(s)^2 \sum_{\mathrm{i}=1}^{N_\mathrm{bins}} H(d_\mathrm{i}) J_0(s d_\mathrm{i}) \tag{4.22}$$

for identical scatterers, and as

$$I_\mathrm{eq}(s) = \sum_{\mathrm{i}=1}^{N_\mathrm{bins}} g(d_\mathrm{i}) J_0(s d_\mathrm{i}) \tag{4.23}$$

for scatterers with varying scattering power but independent of s.

As has been seen, intensity from rotationally averaged systems can be calculated based on pairwise distance histograms. Therefore this histogram is the maximal information that can be obtained from scattering patterns of such systems. This highlights the property of x-ray scattering that the results are usually averages over a large volume of the sample, rather than just an individual molecule.

4.1.5 Multiple Scattering Calculations

The single scattering approach used in equation (4.8) is a good approximation when the sample scatters only weakly. However, in some cases, especially for thick samples used in imaging, it may be necessary to consider also radiation that has scattered multiple times in the sample. One way to look at multiple scattering is that a scattering center at $\mathbf{r}$ in the sample experiences not only the incoming amplitude, but also the amplitude scattered from other parts of the sample [104]. This changes the amplitude and the phase of the wave scattered from $\mathbf{r}$. In turn, the wave emitted from $\mathbf{r}$ interacts with all the neighbouring atoms, changing their scattering. In ordered crystals the solution to this problem has been obtained through the dynamical theory of diffraction [15].

In general, multiple scattering problems are difficult to solve accurately. However, when scattering is concentrated in the forward direction, we can use simplifying approximations that make multiple scattering calculations

practical. We can then assume that the scattered beam sees the same part of the sample as the direct beam sees. If the scattering angles are less than 1 mrad, and the sample size is 0.1 m, this is a good approximation to an accuracy of 0.1 mm. In this case the sample will affect the scattered beam coming from a point within the sample in exactly the same manner as it will affect the direct beam coming from that same point. This allows the sample to be divided into thin layers, perpendicular to the beam direction, each of which has an impulse response defining the effect of scattering from that layer.

Figure 4.6 shows the sample divided into multiple layers. Multiple scattering can then be calculated by having each layer scatter the radiation coming from the previous layer. This includes the attenuated direct beam, as well as the combined scattering by the previous layers. Let $I_{n-1}(\mathbf{s})$ be the intensity coming from the previous layer to layer n and $F_n(\mathbf{s})$ be the impulse response of layer n. With these definitions it is straightforward to write the outgoing intensity from layer n as

$$I_n(\mathbf{s}) = \int_{\mathbf{s}'} I_{n-1}(\mathbf{s}')F_n(\mathbf{s}-\mathbf{s}')\mathrm{d}\mathbf{s}' = I_{n-1}(\mathbf{s}) \circledast F(\mathbf{s})\mathrm{d}. \tag{4.24}$$

In the small-angle region we can present the beam direction by two angles θ_x and θ_z, so that the impulse response of layer n becomes $F_n(\theta_x, \theta_z)$. When the intensity distribution coming to the sample is $I_0(\theta_x, \theta_z)$, and there are N layers, the intensity emerging from the sample is calculated using consecutive convolutions as

$$I(\theta_x, \theta_z) = I_0(\theta_x, \theta_z) \circledast F_1(\theta_x, \theta_z) \circledast F_2(\theta_x, \theta_z) \circledast \ldots \circledast F_N(\theta_x, \theta_z). \tag{4.25}$$

In practice the evaluation of (4.25) can be done in the Fourier-space using the Fourier-convolution theorem [97, ch. 15.5], so that the convolution is replaced by multiplication. Let there be M different types of layers in the sample, type i having a total of N_i layers. Let $\hat{F}_i = \mathscr{F}\{F_i\}$ be the Fourier transform of the impulse response of layer type i, and $\hat{I}_0 = \mathscr{F}\{I_0\}$ be the Fourier transform of the incoming intensity distribution. Then the outgoing intensity can be written as

$$I(\theta_x, \theta_z) = \mathscr{F}^{-1}\{\hat{I}_0 \underbrace{\hat{F}_1\hat{F}_1 \cdot \ldots \cdot \hat{F}_1}_{N_1 \text{ times}} \underbrace{\hat{F}_2\hat{F}_2 \cdot \ldots \cdot \hat{F}_2}_{N_2 \text{ times}} \cdot \ldots \cdot \underbrace{\hat{F}_M\hat{F}_M \cdot \ldots \cdot \hat{F}_M}_{N_M \text{ times}}\}. \tag{4.26}$$

In practice $\hat{F}_i$ for different layer types can be calculated in advance, so that M exponentiations and multiplications are enough to calculate the Fourier representation of the outgoing intensity in (4.26).

Layer thickness ΔL in this approach is selected so that only little scattering within a layer occurs, especially so that the probablity for a photon to scatter twice within a single layer is negligible. However, too small a

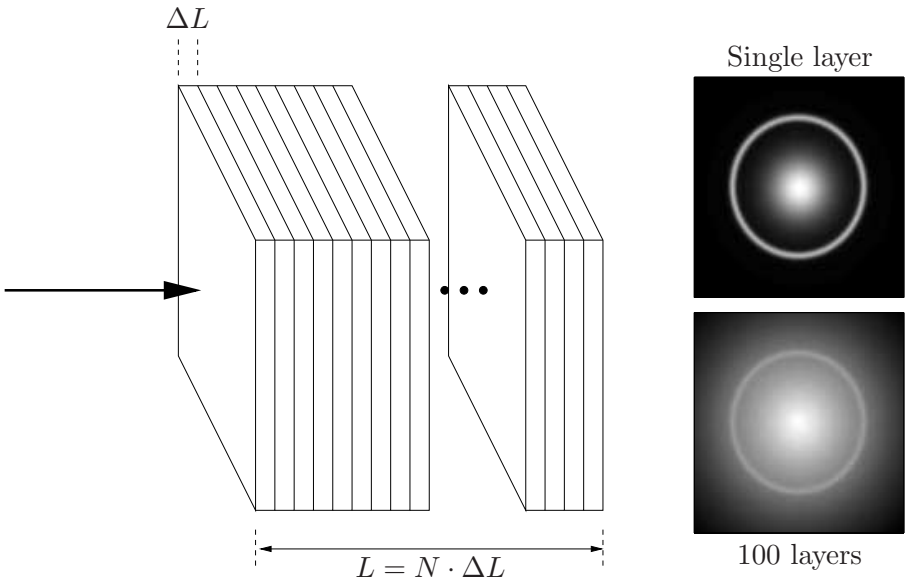

Figure 4.6: Multilayer approach for multiple scattering calculation. The scattering patterns on the right show an example on the effect of multiple scattering (the direct beam portion has been subtracted from these).

layer thickness should also be avoided, because it can increase the effect of numerical inaccuracies in the calculation. The parameter ξ is defined for a single layer to indicate the fraction of the intensity in the direct beam after the beam has passed the layer (cf. section 3.4). Therefore after passing a layer the fraction $1 - \xi$ of the outgoing intensity is scattered. After passing length L in a material composed of layers with thickness ΔL the fraction of the intensity in the scattered beam is $1 - \xi^{L/\Delta L}$. These results will be used in chapter 5 to take the effect of multiple scattering into account in the imaging simulations.

4.2 Contribution of Refraction

Usually a beam of finite extent experiences different refraction at different points of the sample. If the spatial frequency of this variation is low, the variation in refraction can be picked up e.g. in ABI as a spatial variation of intensity. However, for high spatial frequencies the variation cannot be distinguished, and the signal from refraction looks much like the signal from scattering.

The difference that can be observed between scattering and refraction is that in scattering only part of the beam gets scattered, and there is always a component of the direct beam (except for diffraction from highly ordered

materials), while in pure refraction all of the beam is refracted, and there is no direct beam component. The borderline between pure refraction and scattering is not clear, and both of these phenomena do occur simultaneously [105]. Refraction is the dominating phenomenon for particles that are large compared to the wavelength [18, pp. 116–117].

Because refraction affects the whole beam, not just a fraction like the scattering, it offers potentially a good source of contrast. Even for very small density differences the angular beam broadening may be observable. Furthermore, biological samples have structures that are in the proper size range to produce refraction, but that are so small that they cannot be seen in images as individual objects, diameter of the order of a few microns. We study here the contribution of refraction in a material containing spherical refracting particles.

4.2.1 Intensity Distribution from Spheres

Let spheres with radius R and refractive index $n_2 = 1 - \delta_2$ be embedded in a homogeneous matrix with refractive index $n_1 = 1 - \delta_1$. For a ray going through a single sphere the refraction angle depends on which part of the sphere the ray hits, and on the difference of the refractive indexes. A ray going at a perpendicular distance h from the center of the sphere (see figure 4.7) refracts with the angle

$$\Delta\theta = 2\left[\arcsin\left(\frac{n_1}{n_2}\frac{h}{R}\right) - \arcsin\left(\frac{h}{R}\right)\right]. \tag{4.27}$$

This is valid when $hn_1/(Rn_2) < 1$, and for larger values of h there is a total external reflection into angle $\Delta\theta = \pi - 2\theta_1$. For x-rays n_1/n_2 is close to 1 so that the total external reflection contributes only marginally.

The ray hits on the average N particles as it passes through the sample. If the particles are randomly packed, the ray hits each particle at a random location, and this leads to the ray experiencing a statistically similar refraction at each particle. For spheres the azimuthal angle ϕ has a symmetric distribution, and a Monte Carlo method can be used to calculate histograms of the $\Delta\theta$ distribution. Figure 4.8 shows histograms of $\Delta\theta$ for different N and $n_1/n_2 - 1$, calculated using 10^6 rays. The distributions are approximately described by the Rayleigh distribution [106], and also resemble the log-normal distribution [107]. The Rayleigh distribution would be an exact description of $\Delta\theta$ if the refraction angles in the x and z directions were normally distributed. The difference from the Rayleigh distribution seen in figure 4.8 is the result from the fact that the angular deviations in the two directions are not exactly Gaussian but have longer tails on the side of larger angles.

From the distributions of $\Delta\theta$ several key observations can be made: 1) there is no beam going to the direction of the initial incoming beam, and 2)

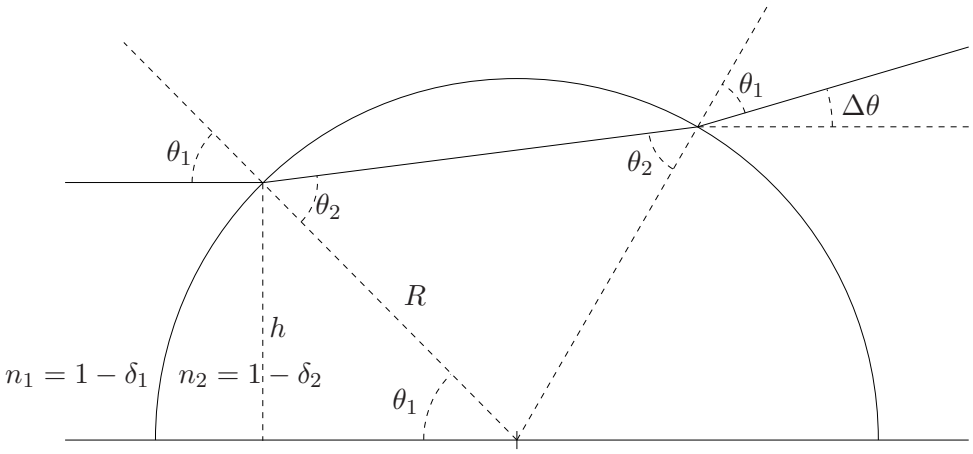

Figure 4.7: Geometry of refraction from a sphere: $\Delta\theta = 2(\theta_2 - \theta_1)$ and $n_1 \sin\theta_1 = n_2 \sin\theta_2$ from Snell's law.

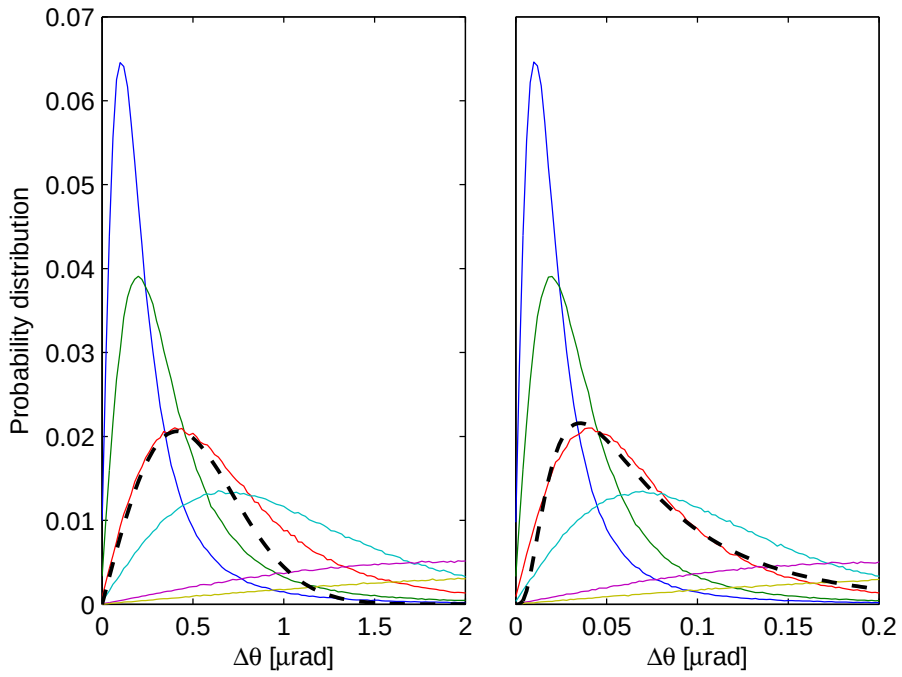

Figure 4.8: Distribution of $\Delta\theta$ for different numbers of spheres ($N = 1, 2, 5, 10, 50$, and 100 for the distributions from the narrowest to widest, respectively). In (a) $n_1/n_2 - 1 = 10^{-7}$ and in (b) $n_1/n_2 - 1 = 10^{-8}$, notice the different scales on the horizontal axis. The thick dashed curve shows in (a) a fit by a Rayleigh distribution and in (b) by a log-normal distribution.

the standard deviation and the peak position of the distribution are approximately linear with $n_1/n_2 - 1$ and $\sqrt{N}$, and 3) the broadening is significant even for small differences in the refractive index, such as $|n_1 - n_2| = 10^{-8}$, indicating that refraction broadening may serve as a good source of contrast.

4.3 Scattering Results from Breast Tissue Samples

We have studied breast tissue samples using SAXS and USAXS. Samples of connective, adipose, and necrotic tissue, about 1 mm thick with 1 cm^2 cross section were used. The scattering curves have been measured from $s = 0\,\mathrm{nm}^{-1}$ up to $s = 0.3\,\mathrm{nm}^{-1}$, the upper limit corresponding to $2\theta \approx 30\,\mathrm{mrad}$ at x-ray energy of 12.4 keV. There are clear differences in the scattering patterns coming from healthy and malignant regions [6]. Calculated scattering patterns based on a cylindrical model of collagen fibrils have been used to establish that the changes seen in the scattering patterns due to malignancy can be largely attributed to structural changes in the collagen fibrils [108]. Scattering results from various authors support the idea that different breast tissue types can at least to some extent be differentiated based on their scattering pattern [109–113].

Figure 4.9 shows the experimental scattering curves for healthy, malignant and adipose regions of one of the breast samples. The curves are displayed on the same intensity scale so that comparison of the absolute intensities is possible. The USAXS patterns have been measured with the Bonse-Hart camera, and the SAXS patterns with the pinhole camera at beamline ID02 at ESRF [114]. Scattering is weak compared to the direct beam so that near $s = 0\,\mathrm{nm}^{-1}$ scattering can not be resolved with good statistical accuracy, and thus the actual data end at around $s = 2 \cdot 10^{-4}\,\mathrm{nm}^{-1}$.

The main components that contribute to the scattering patterns appear to be collagen fibrils in the connective tissue and lipid molecules in the adipose tissue [6]. Collagen fibrils are typically 50 to 100 nm in diameter, and they have an axial period with a length of about 65 nm [115]. The former results in oscillations in the scattering patterns (Bessel peaks in figure 4.9), and the latter in rather sharp peaks (collagen peaks). The interfibrillar packing of collagen fibrils resembles a hexagonal, but loses ordering at longer distances. The average packing distance is around 100 nm [115], and the first order peak is seen in figure 4.9 while the higher order ones are washed away due to lack of long distance ordering.

4.3.1 Scattering Fraction

The fraction of intensity that is scattered is important in determining how large doses are required to get sufficient counting statistics in the scattering

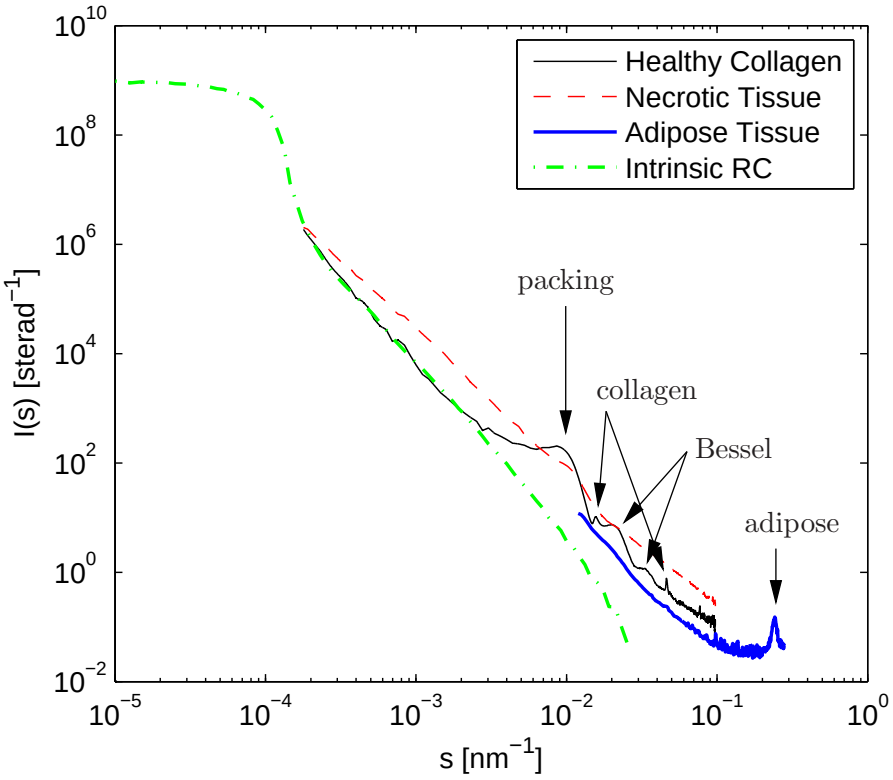

Figure 4.9: Cylindrically averaged scattering curves from various parts of a breast tissue sample from measurements made at beamline ID02 at ESRF [6]. The arrows show the peaks rising from different features of the sample. The collagen peaks are due to periodic variation of the electron density along the axis of the collagen fibrils, the Bessel maxima are from the cylindrical cross section of the fibrils (indicating a rather narrow distribution), and the packing peak is from the approximately hexagonal lateral packing of the fibrils.

signal. The scattering profiles are normalized so that $I(2\theta)$ is the scattering probability (1/steradian) for scattering into angle 2θ. The narrow ring of scattering at angle 2θ covers the solid angle

$$\Omega_0 = \mathrm{d}\theta 2\pi \sin(2\theta), \tag{4.28}$$

where $\mathrm{d}\theta$ is the width of the ring of scattering. By multiplying $I(2\theta)$ with Ω_0 we get the probability of scattering to the ring in the angular range $[2\theta, 2\theta + \mathrm{d}\theta[$.

Let $\Gamma(2\theta_0)$ be the total probability of scattering into angles above $2\theta_0$, i.e.

$$\Gamma(2\theta_0) = 2\pi \int_{\theta_0}^{\pi/2} I(2\theta) \sin(2\theta) \mathrm{d}\theta. \tag{4.29}$$

Because scattering has been measured only in a finite range, the accurate calculation of $\Gamma(0)$ is not possible, but lower bounds can be estimated based on the data. For the healthy collagen $\Gamma(0) \gtrsim 0.36\%$ and for the necrotic tissue $\Gamma(0) \gtrsim 0.76\%$. These values are obtained for the range $1.78 \cdot 10^{-4}\,\mathrm{nm}^{-1} < s < 9.75 \cdot 10^{-2}\,\mathrm{nm}^{-1}$, and at least in this range the necrotic tissue scatters about twice as much as the healthy collagen. The scattering fraction increases with sample thickness as explained in 4.1.5. Therefore when imaging real breasts there may be a considerable amount of scattering, from several to dozens of percent of the outgoing intensity.

A fraction of scattering goes to the peaks in the scattering pattern, especially the collagen peaks, the Bessel peaks and the peak from the adipose tissue. These peaks have been shown to differentiate healthy and malignant breast tissue [4, 116]. In the examples in figure 4.9 the area under the 3rd collagen peak for the healthy tissue corresponds to about 0.0005% of the intensity, and the area under the adipose peak to about 0.005% of the intensity. These are rather low fractions when compared to the total scattering fraction ($\sim 0.4\%$), and we see in chapter 5 that scatter rejection gives much better SNR than methods based on the evaluation of the scattering peaks.

4.4 Central Peak Widening

Widening of the central peak is seen in ABI measurements for some samples, such as paper and PMMA spheres [90]. For the breast tissue samples, however, there is no appreciable widening of the central peak as seen in figure 4.10. This is a consequence of the fact that the scattering fraction is very small as seen previously, and therefore near the central peak the direct beam dominates.

Central peak widening from PMMA spheres and paper (figure 4.11) can be seen as an evidence of strong scattering in the angular range of the intrinsic RC. Using analysis with pseudo-Voigtian functions [90], the RC for the PMMA sample is seen to be of nearly complete scattering, and for the

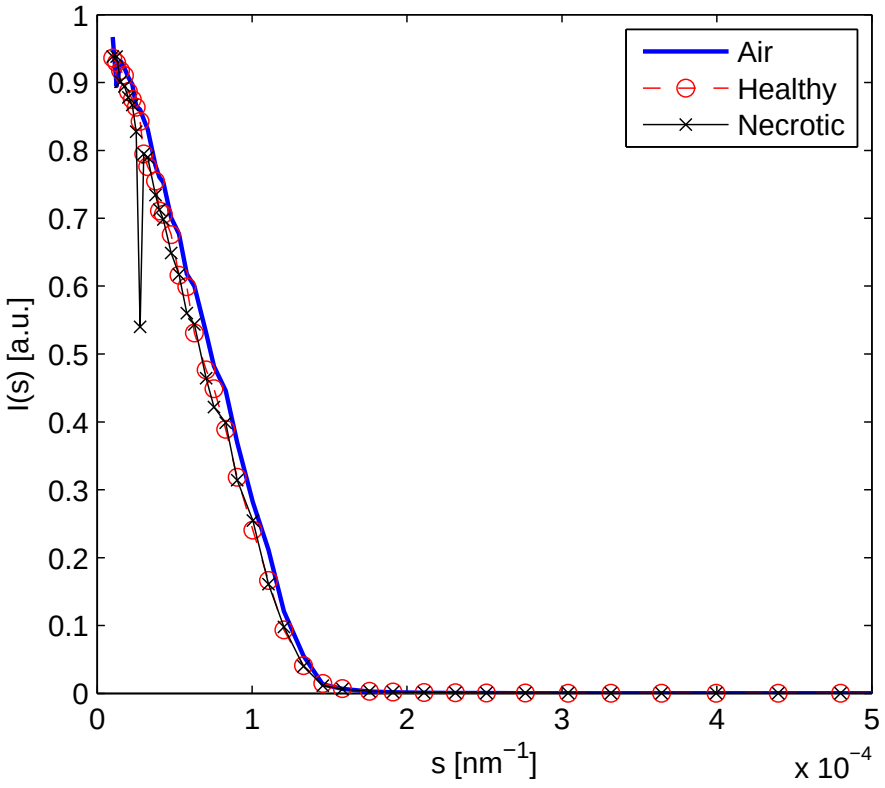

Figure 4.10: The central peak as seen for healthy and necrotic tissue.

paper sample the RC is broadened by about 40% scattering with the rest of the intensity remaining in the direct beam. For the 100% scattering from PMMA spheres the broadening may be more correctly seen as the results of multiple refractions within the sample, instead of scattering.

Two important conclusions can be drawn from these results on the central peak width. First, the width of the central peak does not reflect only the scattering width, but also the scattering fraction. This implies that the scattering width cannot always be obtained directly from the RC width (e.g. by calculating the standard deviation), and a method that separates the scattered and direct beam is preferable in this respect. A second aspect is that for some scattering samples the fraction scattered into neighbourhood of the central peak is very small, even though there is considerable scattering at larger angles. This leads to the possibility that for these types of samples the signal quite far from the central peak may give the best contrast, reminiscent of dark field imaging in optical microscopy.

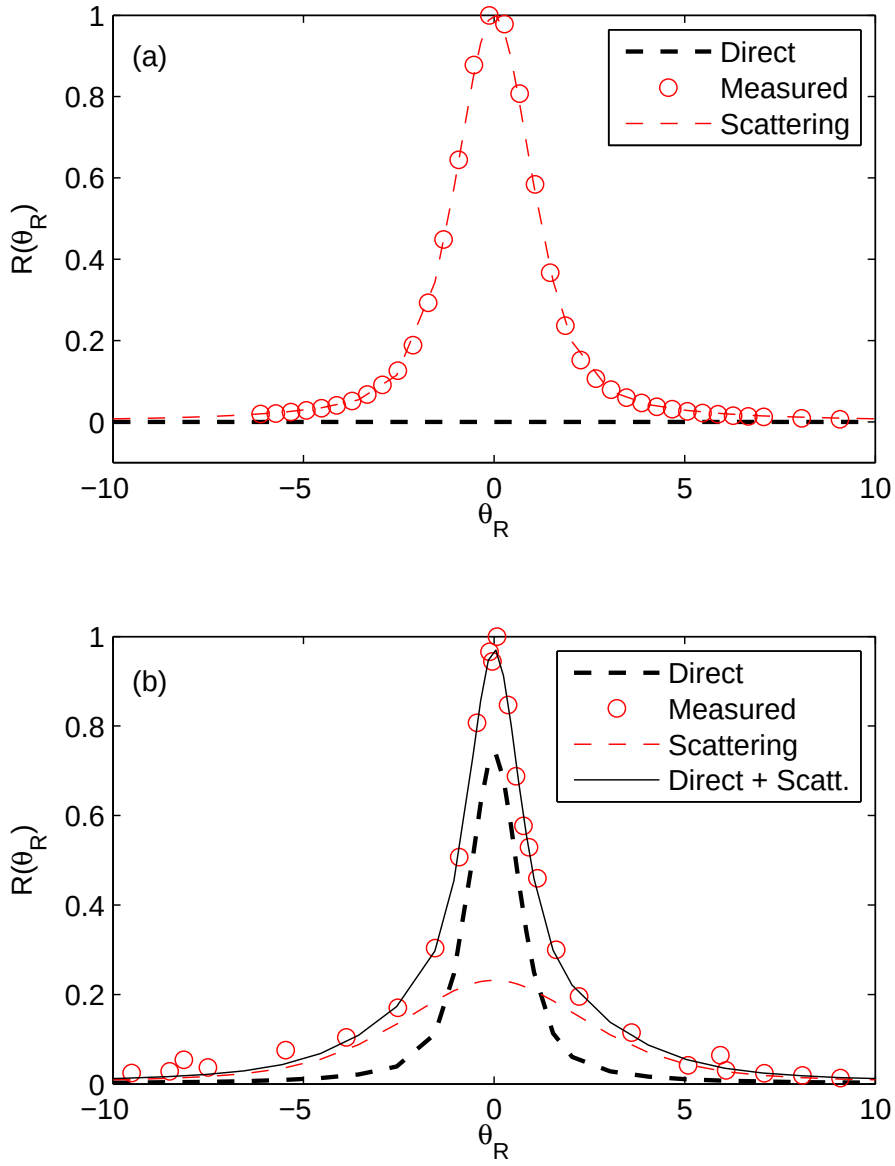

Figure 4.11: Widening of RC due to PMMA (a) and paper (b) samples. About 1 mm thick layer of 100 nm diameter PMMA spheres were used in (a), and 11 layers of paper (about 1.1 mm total thickness) were used in (b).

Chapter 5

Simulation of Analyzer Based Imaging

5.1 Overview

ABI imaging has been simulated previously from many points of view. Geometrical optics simulations on a rod have been used to show that the refraction angle SNR from DEI is better than the conventional absorption SNR [117]. Simulations based on wave-optics have been used to see the combined effect of analyzer and propagation [60, 118–120], and it was found that propagation effects do affect the ABI images, and that under certain circumstances the effects can be combined to enhance the visibility of objects. Simulations of refraction have been used to study the weak-object and geometrical optics approximations in the reconstruction of the refractive index in the case of partially coherent radiation [121], showing that strong artefacts appear near object edges if the validity conditions of the two approximations are violated.

Scattering has been used in imaging simulations, especially in the role of background scattering that reduces the SNR [122–125]. The possibility of using the scattering profiles of biological tissues in photon transport MC programs has also been demonstrated [126, 127]. In ABI imaging scattering has been simulated by convolving the RC with an approximated sample impulse response, usually a Gaussian [66, 89, 128]. The broadening of the RC has also been studied using geometric optics and sub-pixel sized refracting spheres [67], and the results confirmed that the parameters in MIR are line-integrals of the sample.

Our aim is to quantify how different forms of scattering are visible for phantoms that resemble objects in real medical imaging situations. For this purpose a ray tracing program has been developed that takes into account absorption, refraction, and the accumulated halo of SAXS as the beam travels through the sample. We simulate a typical ABI setup (figure 5.1) with

identical monochromator and analyzer crystals in the nondispersive setting. The vertical opening angle of the beam is made larger in the simulation than what it is on synchrotrons so that vertical scanning of the sample is not needed.

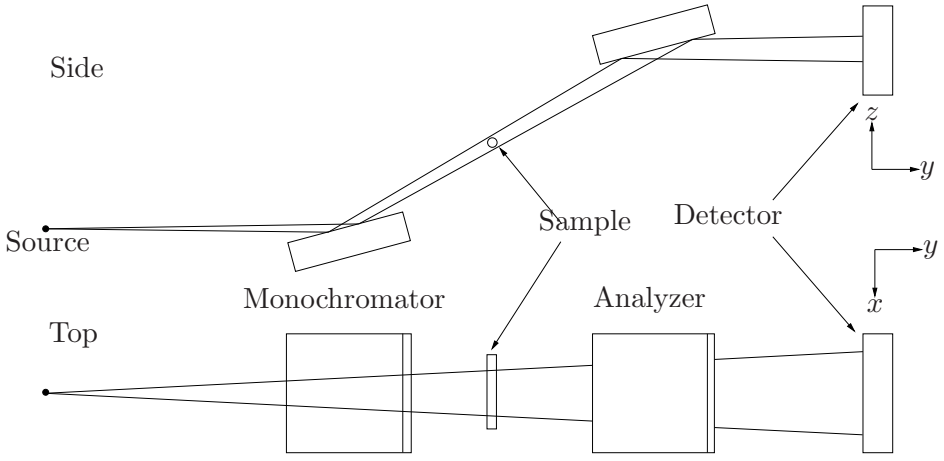

Figure 5.1: Schematic presentation of the simulated imaging system.

5.2 Ray Tracing ABI Images

In ray tracing methods the incoming beam is divided into small sub-beams, and an infinitesimally thin ray is projected through each sub-beam [129, ch. 12]. The ray is traced through the sample and the interactions with the sample are calculated. The behaviour of the ray is taken to represent the behaviour of the whole sub-beam. By its nature the ray tracing method is based on the validity of the geometrical optics approximation so that intensities from different sub-beams are added incoherently.

5.2.1 Ray Interactions With the Sample

Figure 5.2 shows an example of a ray propagating through a sample. The sample is composed of geometric objects, each with uniform material properties. The ray is traced through the sample, and at each object boundary the refraction angle is calculated. At the boundary the incoming beam direction is $\hat{\mathbf{s}}_1$, the surface normal is $\hat{\mathbf{n}}$ and the refractive indexes of the two materials are n_1 and n_2. The outgoing beam direction $\hat{\mathbf{s}}_2$ is in the plane spanned by $\hat{\mathbf{n}}$ and $\hat{\mathbf{s}}_1$ and is

$$\hat{\mathbf{s}}_2 = (\cos\delta\theta \mp b\cos\theta)\hat{\mathbf{s}}_1 \pm b\hat{\mathbf{n}}, \tag{5.1}$$

where $b = \sqrt{(1-\cos^2\delta\theta)/(1-\cos^2\theta)}$, and the upper signs are used when $n_2 < n_1$ and the lower signs otherwise. Here $\delta\theta = (n_1 - n_2)\tan\theta$ (Snell's law), and $\cos\theta = \hat{\mathbf{n}} \cdot \hat{\mathbf{s}}_1$. In this we have assumed that $\delta\theta \ll 1$ (which in practice is always the case for x-rays), so that the first order suffices.

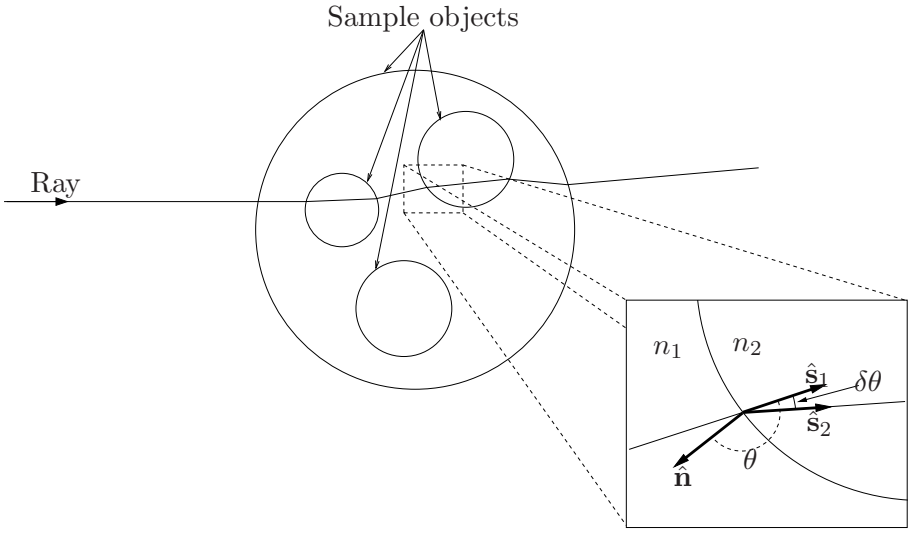

Figure 5.2: An example of a path that a ray takes when propagating through a sample.

The ray travels through N different objects, traversing length L_i in object i (possibly in discontinuous segments). Each object modifies the intensity distribution based on the object's material properties and L_i by attenuating the beam and redistributing the intensity via scattering into a halo around the central beam. The effect of object i on the intensity distribution $I'(\theta_x, \theta_z)$ is $e^{-\mu_i L_i} G_i(\theta_x, \theta_z) \circledast I'(\theta_x, \theta_z)$. When the incoming intensity distribution is $I_0(\theta_x, \theta_z)$ the intensity distribution after passing the whole sample is given by

$$I(\theta_x, \theta_z) = \overbrace{e^{-\mu_1 L_1} \cdot e^{-\mu_2 L_2} \cdot \ldots \cdot e^{-\mu_N L_N}}^{\text{Attenuation}} \times \overbrace{[G_1(\theta_x, \theta_z) \circledast G_2(\theta_x, \theta_z) \circledast \ldots G_N(\theta_x, \theta_z) \circledast I_0(\theta_x, \theta_y)]}^{\text{Redistribution of intensity via scattering}}. \quad (5.2)$$

Each object's scattering function $G_i(\theta_x, \theta_z)$ is calculated via the multiple scattering formalism developed in section 4.1.5.

In the practical implementation the impulse responses and the scattering halos are stored in two dimensional arrays of $N \times N$ elements. Typically $N = 128$ which allows rather rapid calculation and still enables the scattering patterns to be modeled with good precision. This approach is quite

general, working on all types of SAXS patterns, and allows the broadening of the scattering pattern to be taken into account, including the effects from multiple scattering.

5.2.2 Computational Phantoms

Phantoms are used in imaging as objects with known properties so that the imaging methods can be evaluated in a quantitative manner [3, 75, 122–124, 130–134]. We base our calculations on phantoms composed of geometrical objecs (ellipsoids and cylinders) with specific material properties.

Material Properties

Each object in the phantom is uniform, but different objects may have different material properties. The material properties consist of the elemental composition (in weight fraction per element), the density (in gm/cm^3), and a description of the scattering. For the material composition we use throughout the following values (Z : weight %) 1:10.2%, 6:14.3% , 7:3.4%, 8:70.2%, 11:0.2%, 15:0.3%, 16:0.3%, 17:0.2%, 19:0.3%. This corresponds to the soft tissue model found in the literature [29]. The density and scattering properties are then varied to create contrast.

The single scattering pattern for the materials is defined for a layer thickness of 0.1 mm. The scattering function $F(\theta_x, \theta_z)$ is discretized in the simulation so that we have $F(\theta_i, \theta_j)$ defined for a finite set of angles θ_i and θ_j. The single scattering is assumed to be axially symmetric, and it is described by a Gaussian central peak and a Gaussian ring around the central peak. This allows the modeling of central broadening as well as additional details at higher angles. The shape of the single scattering profile is defined by four parameters (ν, σ_1, σ_2, and s_0), see figure 5.3 for definitions. In principle any axially symmetric scattering pattern can be generated as a sum of distributions shown in figure 5.3.

5.2.3 Dividing the Beam into Sub-beams

Only a finite number of sub-beams can be used to calculate the images, and some attention has to be paid to how this division is done. The simplest strategy is to divide the bounding rectangle of the phantom into a uniform grid. In many cases this uniform sampling strategy leads however to either unnecessarily long computation times, or too large sub-beams for proper sampling of all sample details. Therefore a better strategy is to use adaptive sampling so that areas with details get smaller sub-beams than areas that are rather uniform. This type of non-uniform subdivision is commonly used in ray-tracing algorithms [129, ch. 14].

Figure 5.4 shows an example of a beam divided with two possible methods with equal resolution at places of interest. The algorithm that we use

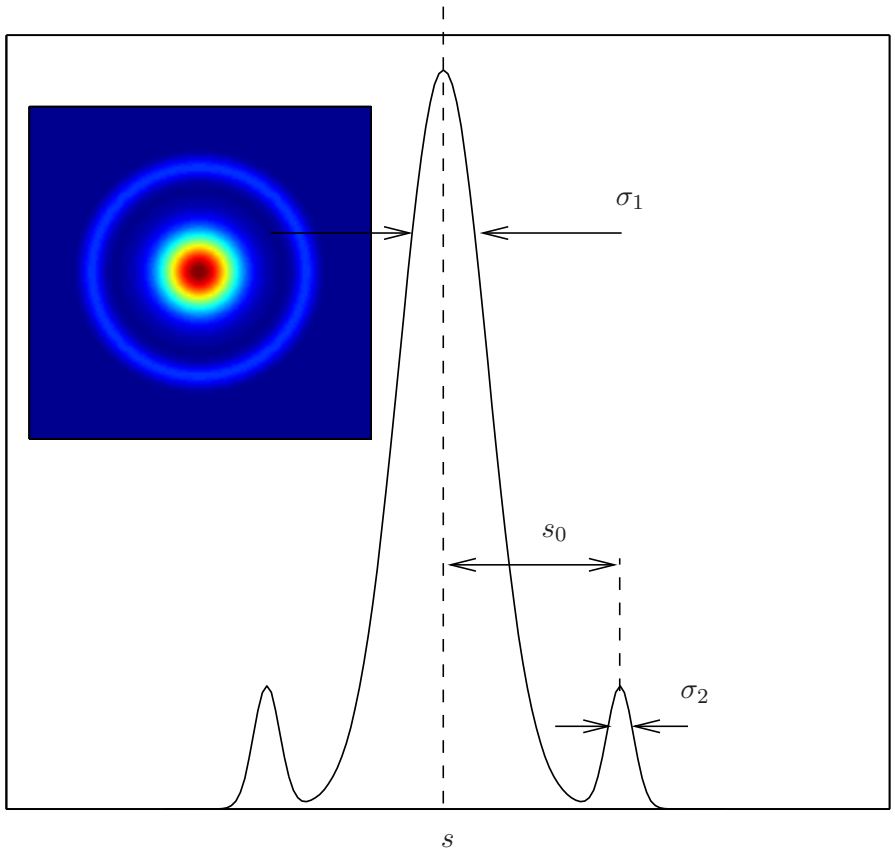

Figure 5.3: An example of a scattering profile (with the 2 dimensional version in the inset) with the parameters defining the profile shape. The central peak is defined by width σ_1, and the ring by width σ_2 and position s_0. The parameter ν is defined to be the fraction of scattering going to the central peak, so that the intensity ratio of the central peak to the ring is $\nu/(1-\nu)$.

divides the beam into four equally sized sub-beams, and recursively continues the division of each sub-beam until it is either smaller than required by the objects it intersects, or it does not intersect any of the sample objects.

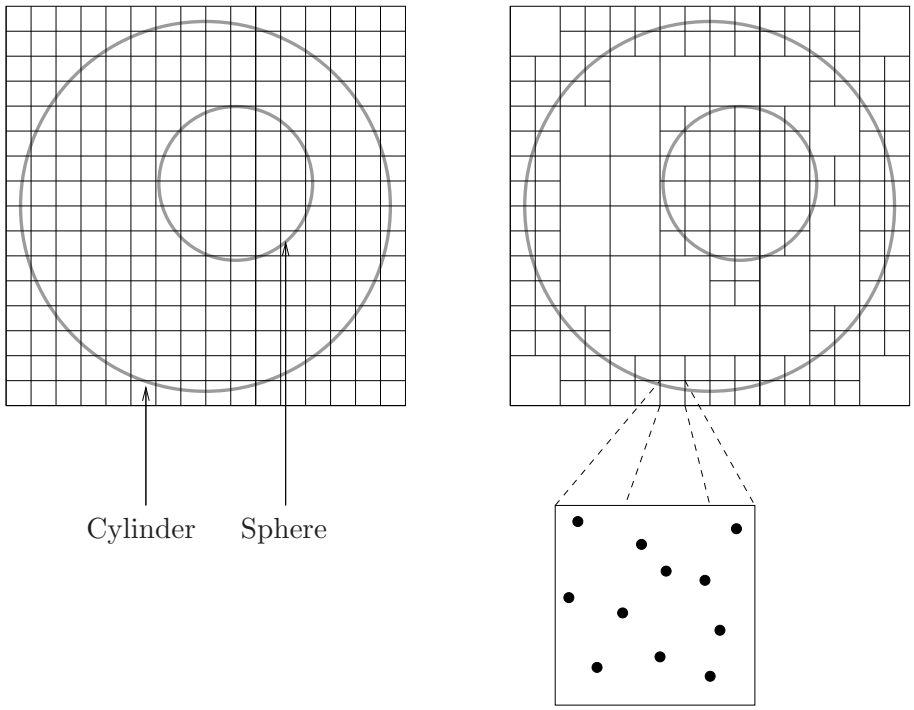

Figure 5.4: Example of uniform sampling (on the left) and adaptive sampling. The beam is sampled at the centers of the squares. The enlargement shows how a sub-beam could be sampled stochastically.

We use a simple approach for subdividing the beam that starts with a uniform subdivision. Each sub-beam is then considered separately, and subdivided further if it intersects an edge of an object. The subdivision is continued until the sub-beams do not intersect any object edges, or a predefined resolution limit is reached. This approach allows the resolution to be higher at the edges, where most of the artefacts originate, while keeping sufficiently low resolution at other areas to facilitate quick calculation.

After a suitable subdivision of the beam has been made, each sub-beam is considered separately, and one ray is sent through the center of the sub-beam rectangle to calculate attenuation and scattering. Refraction of the beam is more sensitive to artefacts near the edges of the objects than attenuation or scattering, so that sampling at a higher resolution is used for the determination of the refraction angle. For each sub-beam $N_{\text{stochastic}}$ rays whose locations within the sub-beam's rectangle are randomly selected are used to sample the possible refracted direction of the sub-beam. The median

of the resulting directions is taken, and this is used to calculate the refraction angle for the sub-beam. This type of stochastic sampling is also common in other ray-tracing methods, as complementary to the regular subdivision method [129, ch. 14].

5.2.4 Ray Interaction with the Analyzer and Detector

After the ray has gone through the sample, it is propagated to the detector via the analyzer crystal. At this point the ray propagates to direction $\hat{\mathbf{s}}_1$ and the intensity has the distribution $I(\theta_x, \theta_z)$ around the main direction. The analyzer attenuates the incoming beam according to the intrinsic RC and the angle at which the beam meets the analyzer. Here θ_x and θ_z describe the angular deviation from $\hat{\mathbf{s}}_1$ in the coordinate system of the refracted beam $(\hat{\mathbf{x}}', \hat{\mathbf{y}}', \hat{\mathbf{z}}')$, where $\hat{\mathbf{y}}'$ is parallel to $\hat{\mathbf{s}}_1$ and $\hat{\mathbf{x}}'$ is in the xy-plane.

The analyzer sees the angular changes only in the yz-plane. For the scattering component at angle (θ_x, θ_z) the angle with respect to the y-axis in the yz-plane is $\theta_{yz} = \tan^{-1}(\hat{\mathbf{s}}_1 \cdot \hat{\mathbf{z}}) + \theta_z = \Delta\theta_z + \theta_z$, where the first term is due to refraction and the second due to scattering. The reflection coefficient for this component at rocking angle θ_R is $R_\mathrm{int}(\theta_{yz} - \theta_R)$, and the intensity of the scattering component arriving at the detector is $I(\theta_x, \theta_z) R_\mathrm{int}(\theta_{yz} - \theta_R)$

For each scattering component the beam position $\mathbf{p}_1$ at the detector is calculated based on the beam position at the sample plane $\mathbf{p}_0$, distance $L_2 + L_3$, the direction of the beam ($\hat{\mathbf{s}}_1$ + the scattering angle), and the analyzer angle (which affects the z-coordinate). See figure 5.5 for an illustration. When $\mathbf{p}_1$ is known, a rectangle of size $w'_\mathrm{sub} \times h'_\mathrm{sub}$ is centered on the point, corresponding to the size of the sub-beam that was used (magnified by the factor $(L_1 + L_2 + L_3)/L_1$ from the sub-beam size at the object plane). Each detector pixel is checked for its overlap with the rectangle, and intensity is added according to the size of the overlapping area multiplied by the intensity transmitted through the analyzer. The values recorded at the pixels are therefore areas, which when multiplied by the intensity give the flux at each pixel.

5.2.5 Dose Calculation

The dose on the sample is recorded by dividing the sample into small cubic volume elements (voxels), and keeping account of the accumulated dose in each voxel. For each voxel the material properties are taken from the object that is located at the center point of the voxel. Each ray is propagated through the sample, and the absorption in each voxel is calculated. A realistic sample size is about $(100\,\mathrm{mm})^3$, and in order not to have an excessive number of voxels, a voxel size of $(0.5\,\mathrm{mm})^3$ is used. The dose is thus calculated quite roughly, and aliasing effects do occur in this approach. Therefore the actual dose images presented are further smoothed with a fil-

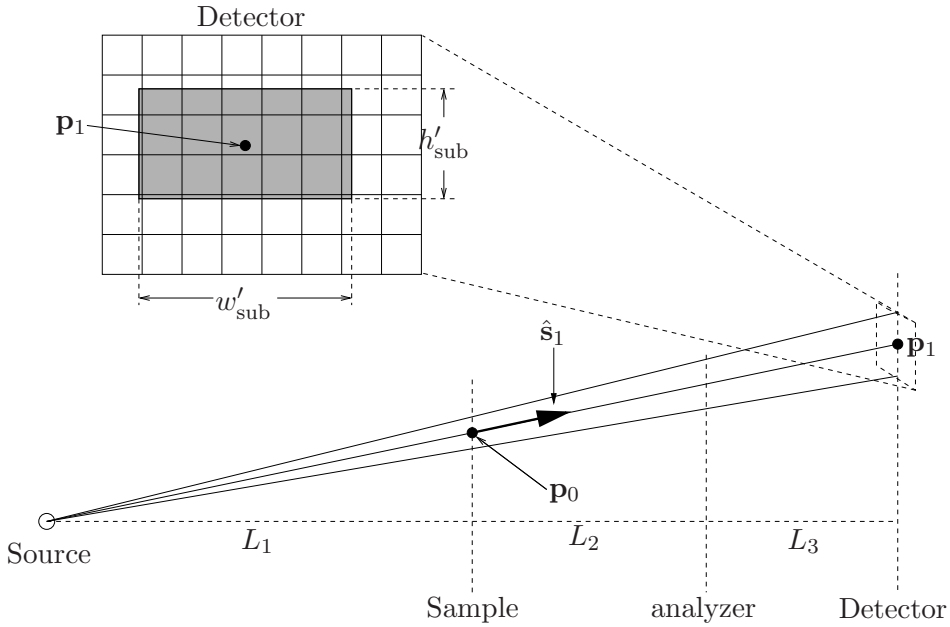

Figure 5.5: Schematic figure showing how the position of the beam at the detector is determined. The overlap of the sub-beam with the detector pixel array is shown also.

ter. An example of a calculated dose map for a phantom is shown in figure 5.6.

In the dose calculation we have not taken into account the effect of scattering. Due to scattering, especially scattering at high angles near the backscattering regime, the photons travel longer distances within the sample so that absorption increases. When calculating the entrance surface dose we have taken into account only the photons from the incoming beam. In reality there are also photons scattering from within the sample. These photons travel through the sample a longer distance than the photons going directly through, and thus the scattered photons contribute so as to increase the dose in the sample. Especially backscattering increases radically the distance traveled in the sample. At the entrance surface this typically contributes a factor of the order of about 1.1-1.6 to the dose [135]. Therefore the dose maps calculated here are not quantitative, but give qualitatively correct results to within a factor of about 1.5. We denote by D_{skin} the dose (ignoring the scattering) calculated at the entrance surface of the phantom. More precise calculations could be done via Monte Carlo simulations following the trajectories of the photons and ionized electrons [136], but for us the correct order of magnitude of the dose is enough, and the simpler simulation suffices.

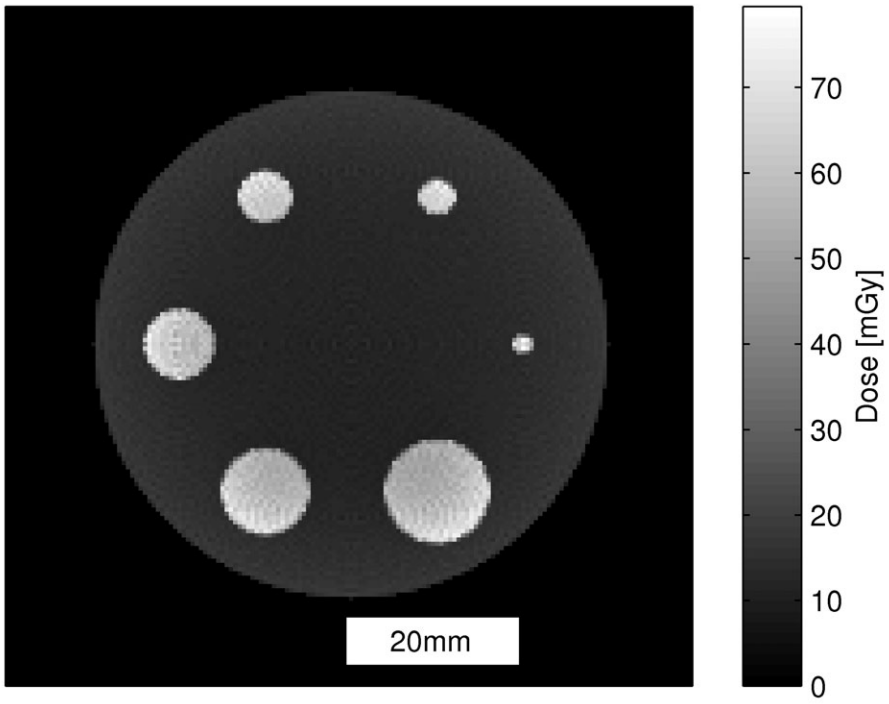

Figure 5.6: Example of a dose map for a phantom consisting of cylinder of soft tissue containing different sizes of cylinders made of bone. CT image was taken with a full 360 degree rotation with projections at 1 degree increments. The photon energy was 51.5 keV, the flux at the sample was $2.9 \times 10^8\,\mathrm{photons/s/mm^2}$, and the irradiation time was 20 ms for each projection.

5.2.6 Image Normalization and Processing

The fractional intensity I/I_0 is used in the calculations (here I_0 is the incoming intensity at the location of the sample). To convert to real photon counts the calculated values are multiplied by the actual photon flux after the monochromator [photons/m^2/s], the DQE, and the exposure time [s]. The dose maps are normalized by multiplying with the exposure time, the flux and the energy per photon.

The images are then further processed to imitate the characteristics of the imaging setup that were not taken into account in the previous steps. Convolving the results with the PSF of the imaging setup softens sharp features in the image, but also decreases the effect of artefacts that may remain from the discrete sampling with rays. Then the noise is taken into account, which is essential for the evaluation of the SNR. We assume an idealized imaging setup, so that the only source of noise is from the counting statistics, which gives a lower limit for the noise in practice. The parameters used in the simulation are shown in table 5.1.

L_1	150 m
L_2	0.1 m
L_3	0.1 m
Pixel size	47 µm
σ_{PSF}	50 µm
DQE	1
Monochromator	Si 333
Analyzer	Si 333
Photon Energy	51.5 keV
I_0	$2.9 \cdot 10^8$ phot/s/mm^2

Table 5.1: Parameters used in the imaging simulations. These correspond roughly (except L_2, L_3 and DQE) to the ones used at ID17 at ESRF (cf. table 2.2).

5.2.7 Analysis of the Simulation Method

Key Approximations in the Simulation

After passing the monochromator the beam is assumed to be completely monochromatic from the point of view of absorption, refraction, scattering and dose calculations. For Si 333 reflection $\Delta E/E \approx 10^{-5}$ at 50 keV, which results in $\Delta\mu/\mu \lesssim 10^{-5}$ and $\Delta\delta/\delta \lesssim 2 \cdot 10^{-5}$ for light elements, and $\Delta s/s \approx 10^{-5}$. As the refraction angle is proportional to δ, and the scattering angle (in the small angle regime) to s, the assumption of monochromatic beam is a good approximation.

Propagation effects are not taken into account in the geometrical optics simulation. For sufficiently spatially coherent beams with propagation distances of over 1 meter, the effects from propagation are clearly visible in ABI images, especially near the edges of objects [120, 121, 137]. Therefore the simulations corresponds to the case where either the spatial coherence of the incoming beam is very small, or the analyzer and the detector are placed immediately after the sample so that the propagation length is small, which does not yet show good propagation contrast [3]. The visibility of propagation effects requires better spatial coherence than what is required by ABI [3], so that it is possible to do ABI imaging without the propagation effects by keeping the coherence at a suitable level.

Artefacts

Due to the digital nature of calculation some artefacts remain that are not seen in real measurements. Especially, before taking into account the detector PSF, edges are seen to be accentuated by the scattering signal. This is due to the abrupt change in scattering and absorption properties at the edge. This effect is most prominently visible in the absorption image taken without the analyzer, and even there it is so small that it is washed out by smoothing with the detector PSF.

The termination of the scattering function $F(\theta_i, \theta_j)$ at some maximum angle is a potential source for artefacts. We have mostly used 128×128 values of s elements with $\Delta s = 2 \cdot 10^{-5}\,\mathrm{nm}^{-1}$. Therefore any scattering going beyond $s = 1.3 \cdot 10^{-3}\,\mathrm{nm}^{-1}$ is lost. This causes additional scatter rejection that can be seen even in the images calculated without the analyzer. This is not a problem for narrow Gaussian scattering patterns, but if a Lorentzian with long tails is used the effect may become visible. The level of this artefactual scatter rejection can be diretly estimated from the images calculated without the analyzer, and if artefacts are too large the calculation can be repeated using larger angles for the termination or larger Δs.

The size of Δs affects also how scattering is seen in the detector. If Δs corresponds to an angle that is larger than the FWHM of the intrinsic RC, then oscillations in the recorded RC are seen. Therefore we keep Δs small enough so that the oscillations do not become too large, in practice $\Delta s = 2 \cdot 10^{-5}\,\mathrm{nm}^{-1}$ or $\Delta s = 4 \cdot 10^{-5}\,\mathrm{nm}^{-1}$.

5.2.8 Scattering and Refraction Example

We use two phantom geometries (shown in figure 5.7), each consisting of a background and six embedded details. The cylinder details are used to study the effect of pure scattering contrast, and the sphere details are used to study scattering, refraction and absorption. The size of the largest detail

(1 cm) is of the same order of magnitude as the typical size of breast cancer lesion at detection [138].

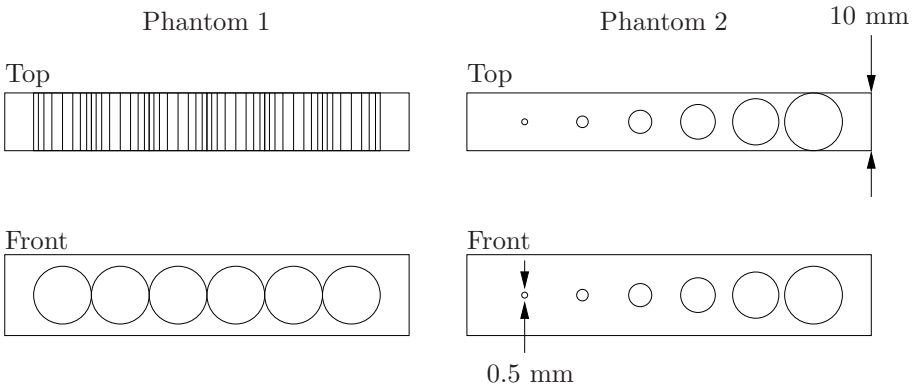

Figure 5.7: The geometry of the two phantoms used. In phantom 1 the details are cylinders, and in phantom 2 they are spheres.

At first we illustrate the general properties of various contrast mechanisms, and therefore choose material properties that give rather good contrast. For the background and the cylinder objects we use the density $\rho = 1.00\,\mathrm{g/cm^3}$, and for the spheres $\rho = 1.01\,\mathrm{g/cm^3}$. The background produces no scattering (i.e. $\xi = 1$). The details have purely central scattering with $\sigma_1 = 10^{-3}\,\mathrm{nm^{-1}}$. For the cylinder details the scattering fraction varies from 1% to 11% (due to changes in ξ), and for the spheres the scattering fraction (at the centerline of the sphere) varies from 1.2% to 11% due to changes in the sphere size.

We study the following parameters: absorption, attenuation with scatter rejection (E-DEI), $\Delta\theta_z$ (E-DEI), σ_{MIR}, and γ_{W} (W-DEI). These are shown in figure 5.8 for the cylinder details with a noise level corresponding to $D_{\mathrm{skin}} = 1\,\mathrm{mGy}$. As can be seen σ_{MIR}, γ_{W} and the scatter rejection image all show the signal from scattering, but $\Delta\theta_z$ and absorption do not. The latter confirms that the level of artefactual scatter rejection due to the termination of $F(\theta_i, \theta_j)$ is insignificant in this case. There is also difference in σ_{MIR} between different cylinders showing the effect of widening due to increased fraction of scattering (and also to a small degree due to increased multiple scattering). In this case of no scattering from background the attenuation image gives the best SNR. This is due to the fact that it contains signal from the scatter rejection, and therefore is sensitive to changes in the scattering fraction. The other scatter related parameters depend partially on the shape of the scattering and partially on the scattering fraction, and are not as sensitive to changes in the scattering fraction as the attenuation image.

For the sphere details the effect of density change appears in absorption, attenuation and $\Delta\theta_z$, as seen in figure 5.9. The scattering related parameters

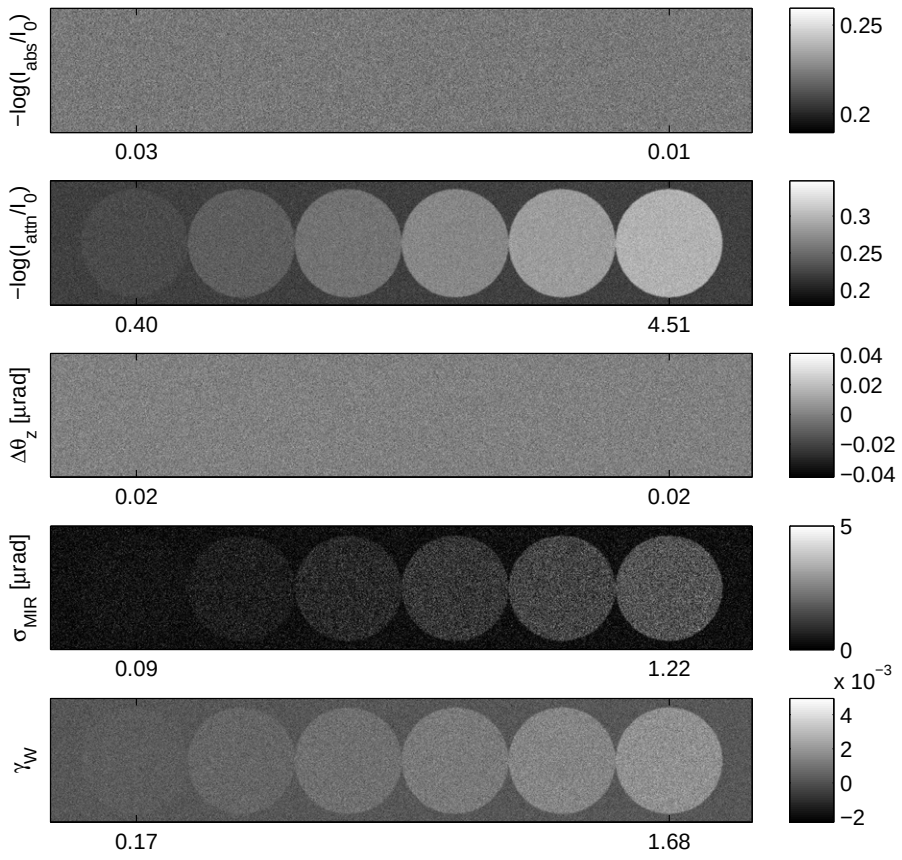

Figure 5.8: Images of the cylinder details for $D_{\mathrm{skin}} = 1\,\mathrm{mGy}$ for the case when there is no scattering from the background. The numbers on the horizontal axes indicate the SNR for the details in question.

show also contrast, but due to the smaller size of the spheres as compared to the cylinders, the signal is somewhat weaker than in the case of the cylinder details. The refraction contrast demonstrates that the SNR does not depend appreciably on the size of the sphere, because the signal comes only from the edges. The SNR for all the parameters is to a good accuracy proportional to $\sqrt{D_{\mathrm{skin}}}$, which shows that in the presence noise from counting statistics only, each method benefits equally from improved counting statistics due to increased dose.

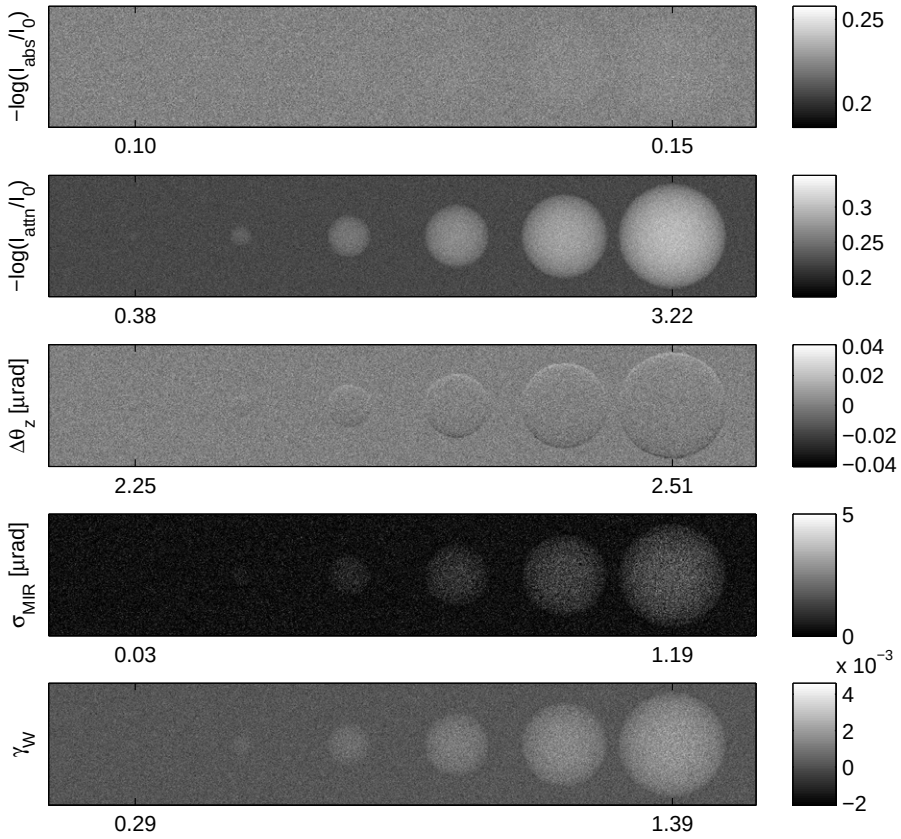

Figure 5.9: Images of the sphere details for $D_{\mathrm{skin}} = 1\,\mathrm{mGy}$ for the case when there is no scattering from the background. The numbers on the horizontal axes indicate the SNR for the details in question.

5.3 Visibility of Scattering

5.3.1 Overview

In the examples in 5.2.8 the scattering objects were embedded in a non-scattering background, which produced good contrast, especially through scatter rejection. In some cases this may be realistic, such as for bones embedded in soft tissue as has been observed with the grating interferometry technique [139]. In some other cases the differences are not so clear, and then the goal is to be able to tell apart different types of scattering from each other. There are two sources of contrast: i) the variation in the scattering fraction, and ii) the variation in the scattering shape. We consider these separately.

We consider two types of scattering patterns: i) purely central scattering where the changes appear in the central peak of the RC, and ii) scattering into an axially symmetric peak at some distance from the center. The first of these situations is more amenable to ABI imaging, as the effect of scattering is directly visible in the shape of the central peak, and is thus quantified by measurements at a few analyzer positions around the peak centre. However, from breast tissue there is only little scattering into the forward direction, and scattering into the peak at a wider angle corresponds more closely to what might be seen when imaging the breast.

Before going to the detailed simulations we illustrate how different scattering patterns are transmitted by the analyzer. As was seen in section 3.4, the analyzer crystal is sensitive to changes only in θ_z of the incoming radiation, and changes in θ_x do not affect the transmission. Figure 5.10 illustrates this. Equation (3.12) shows that the intensity is convolved with the intrinsic rocking curve, and integrated in the x-direction. For the axially symmetric scattering patterns this means that scattering coming to angle 2θ contributes to intensity recorded at all rocking angles $\theta_{\mathrm{R}} <= 2\theta$.

For some scattering shapes the effect of lateral integration is mathematically simple. For example a Gaussian scattering profile, $I(\theta_x, \theta_z) \sim \exp[-(\theta_x^2+\theta_z^2)/2\sigma]$, remains unchanged by lateral integration, and for $I(\theta_x, \theta_z) \sim 1/(\theta_x^2 + \theta_z^2)^{n/2}$, with $n > 1$, which is commonly observed in SAXS, lateral integration produces $I(\theta_R) \sim 1/\theta_R^{n-1}$ [140]. Figure 5.11 shows the effect of lateral integration for two scattering patterns. Noteworthy is that for the distribution from multiple refractions (cf. section 4.2), the integration brings considerable intensity into the forward direction as well. This underlines the fact that scattering and multiple refraction are very similar phenomena from the point of view of ABI. For the peak at high angles there is also significant intensity in the forward direction, but this appears as a rather featureless background signal.

The angular passband $\Delta\theta_{\mathrm{FWHM}}$ of the analyzer is fixed by the properties of the crystal, while the angular width of the scattering pattern, σ_{scat}, may

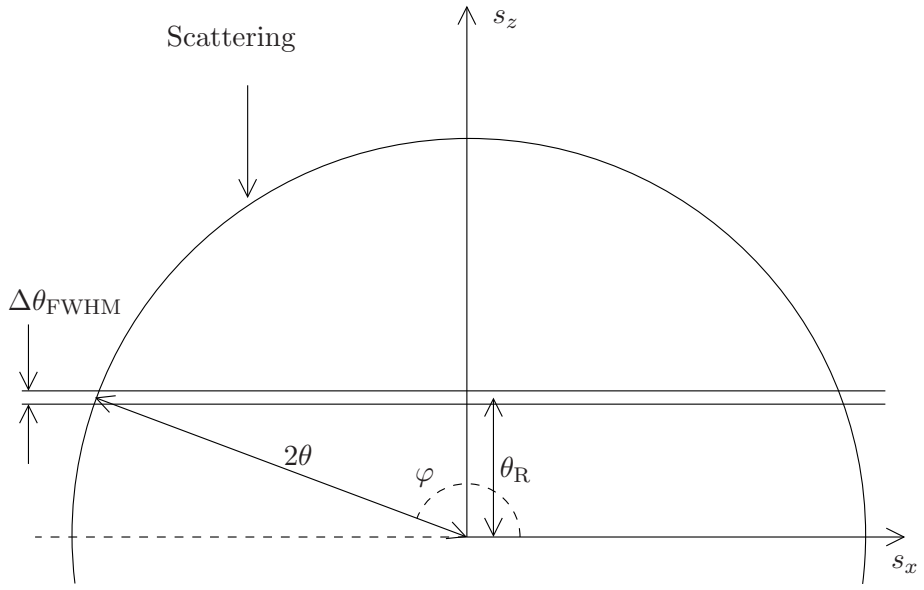

Figure 5.10: Illustration of analyzer pass-band (horizontal lines). The intensity passing the analyzer is integrated in the direction of s_x.

vary based on the properties of the sample. The fraction of scattering passing at a given analyzer angle is proportional to $\sigma_{\mathrm{scat}}/\Delta\theta_{\mathrm{FWHM}}$. Therefore scattering patterns that are wide compared to the analyzer passband give only very little intensity for any given analyzer angle, and recording them completely may result in prohibitively high dose in ABI imaging. For example, the first collagen peak in the breast tissue samples is at $s = 0.015\,\mathrm{nm}^{-1}$, which at 50 keV x-ray energy corresponds to $2\theta = 0.36\,\mathrm{mrad}$. To record the whole scattering pattern up to this angle would require the use of the order of 1000 analyzer positions, which in most cases is not practical.

5.3.2 Scattering in the Central Peak

Let the scattering be central and Gaussian with $\sigma_1 = 1.59 \cdot 10^{-4}\,\mathrm{nm}^{-1}$ in the background. In the details σ_1 is 1–6% larger than in the background. The scattering width corresponds to about 3.8 μrad at 51.5 keV x-ray energy, being therefore about three times the width of the FWHM of the intrinsic RC. This angular range corresponds to a particle size of several micrometers, and thus the origin of this central broadening is more likely due to refraction than pure scattering. The scattering fraction is 10% of the outgoing intensity for both the details and the background.

Examples of the calculated RCs are shown in figure 5.12. There are small but clear differences between the RC of the background and that of

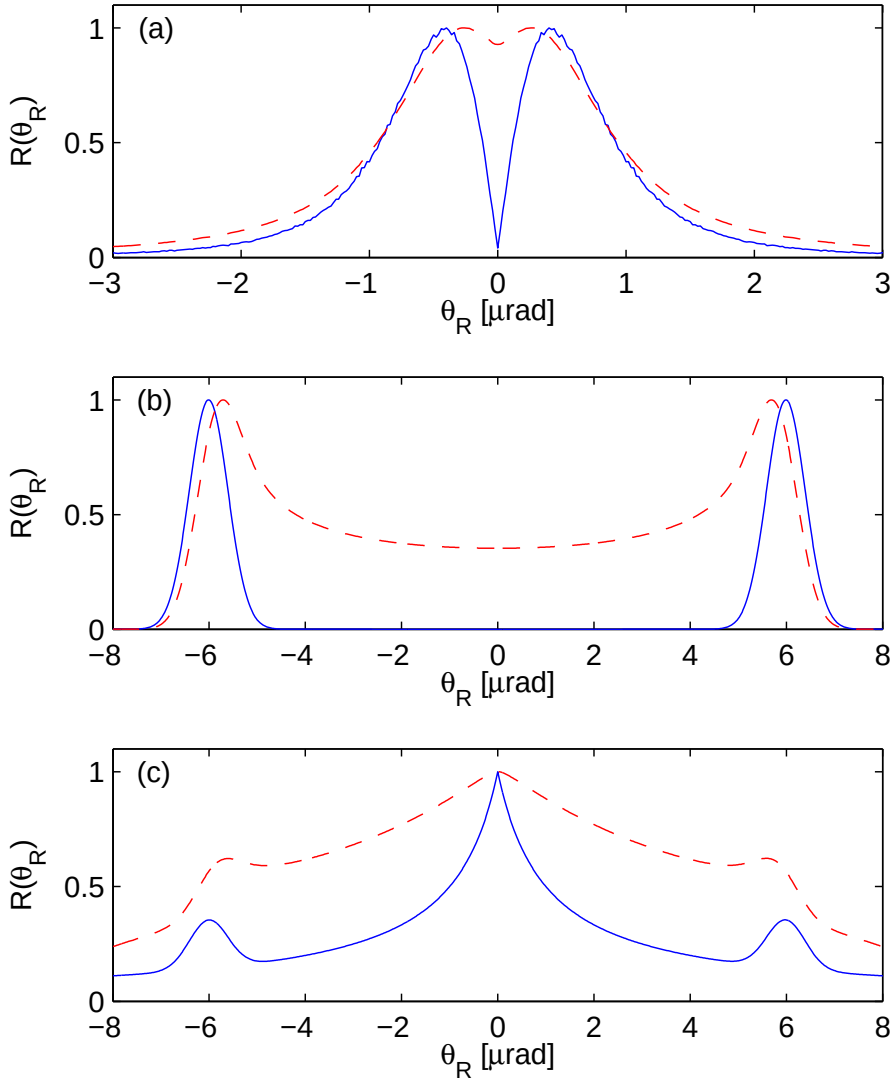

Figure 5.11: Axially symmetric scattering profiles (solid lines) and the corresponding profiles after lateral integration (dashed lines). Shown are a profile from multiple refraction (a), a strong peak at larger angles (b), and a peak on top of a $1/(s+\epsilon)$ background (c).

the detail. Even though the changes in the single scattering patterns are in the width of the central peak, there appears also differences at higher angles due to multiple scattering, indicating that the tails can also serve as a potential source of contrast.

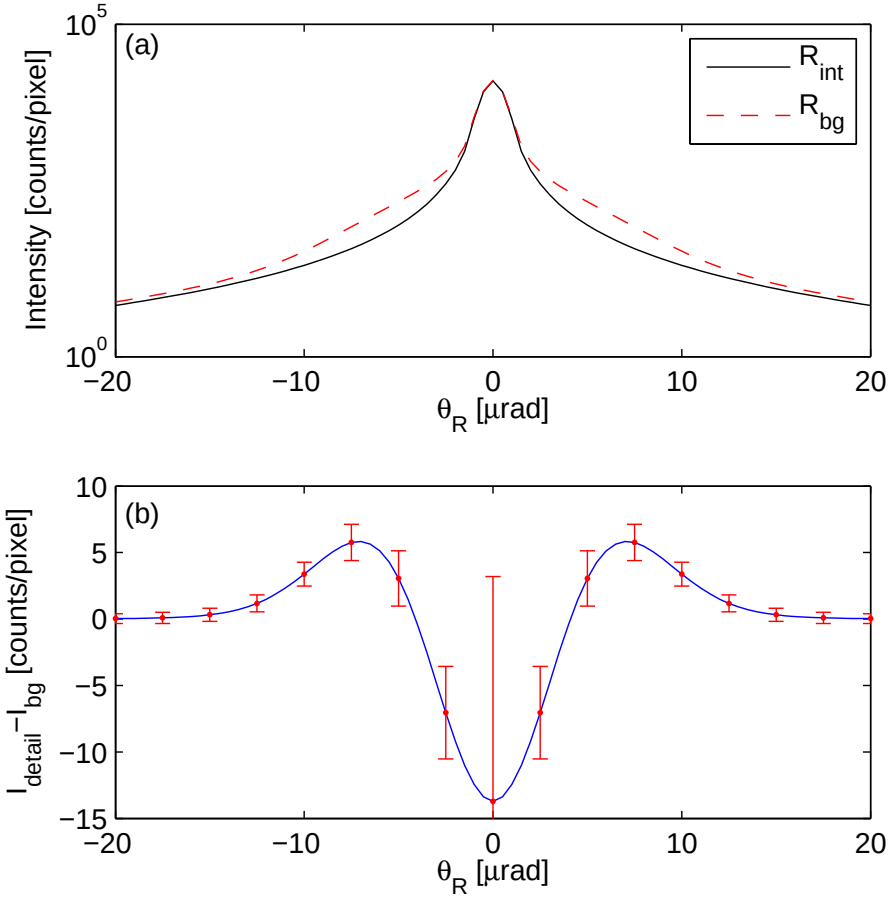

Figure 5.12: Recorded intrinsic RC (attenuated with the effect of absorption and scattering) and the RC from the background (a). Difference between RCs for the background and the detail, with the error bars showing the variation due to photon statistics (variation divided by 10 for clarity) (b). The counts are obtained for the case $D_{\text{skin}} = 1\,\text{mGy}$.

The differences in counts per pixel in figure 5.12 are quite small, and therefore the parameter maps shown in figure 5.13 for $D_{\text{skin}} = 10\,\text{mGy}$ show still rather poor SNR. Here γ_{W} shows clearly the best SNR, and σ_{MIR} and the attenuation image are rather close to each other. By looking at figure 5.12 (b) there are peaks in the difference curve quite close to the position where γ_{W} is calculated (around 10 μrad), partly explaining why γ_{W} has the

best SNR. For scattering with larger width the differences appear at higher angles, and γ_W may not be as optimal as here, although if the approximate scattering angles are known a priori, then γ_W can be based on the RC recorded at angles corresponding to maximum scattering. On the other hand, although the changes near the center are the largest, they are masked by noise due to the intensive direct beam (90% of intensity in this case). This implies that small differences in the scattering width of the central peak are difficult to quantify when the scattering signal is overwhelmed by the direct beam.

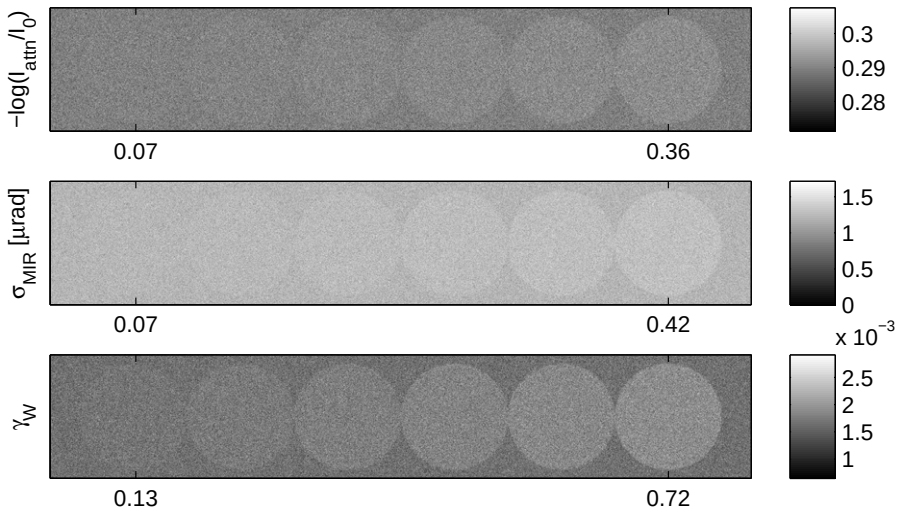

Figure 5.13: Images of the cylinder details with 10% central Gaussian scattering, and varying scattering width, 1–6% larger in the details (increasing from left to right) than in the background. The SNR values displayed on the horizontal axes are calculated for $D_{\mathrm{skin}} = 10\,\mathrm{mGy}$.

Figure 5.14 shows the parameters and SNR values obtained when the sample is similar to what was used in figure 5.13, but now with 90% of the outgoing intensity being scattered. This increase from 10% to 90% should increase the SNR of scattering related parameters by about a factor of $\sqrt{9} = 3$ based on the counting statistics of the scattered photons. The increase in SNR is considerably larger than expected, and different for the different quantities (about a factor of 11 for attenuation, 7 for σ_{MIR}, and 4 for γ_W). One reason is the broadening of the central peak due to multiple scattering, which increases the differences between the details and the background (width of the scattering pattern in the background changes from $\sigma = 3.88\,\mu\mathrm{rad}$ to $\sigma = 5.05\,\mu\mathrm{rad}$, and in the most visible detail from $\sigma = 4.11\,\mu\mathrm{rad}$ to $\sigma = 8.21\,\mu\mathrm{rad}$, i.e. the difference in width changes from 6% to 60% due to multiple scattering). Parameter γ_W does not have the

best SNR any more. This is due to the fact that γ_W utilizes only a small fraction of the RC, and now that the direct beam does not dominate, the other parameters are able to see the differences better.

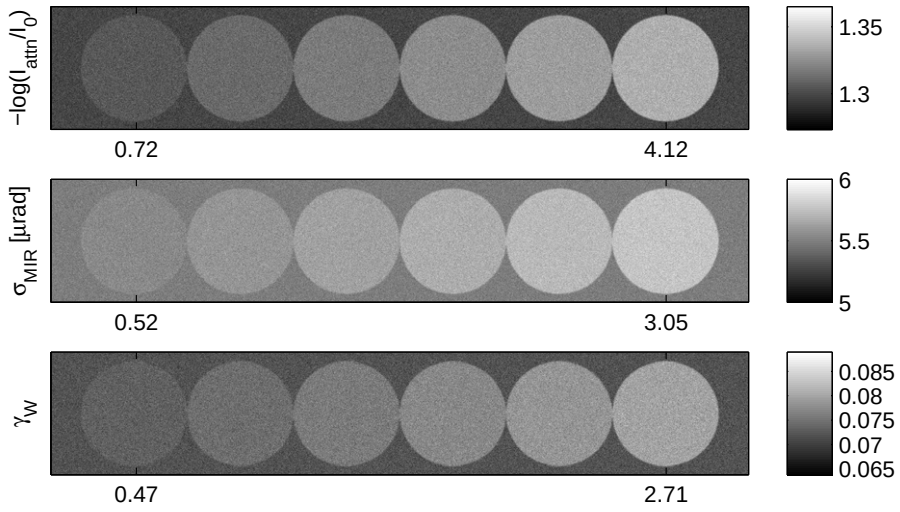

Figure 5.14: Images of the cylinder details with 90% central Gaussian scattering, and varying scattering width, 1-6% larger in the details (increasing from left to right) than in the background. The SNR values displayed on the horizontal axes are calculated for $D_{\mathrm{skin}} = 10\,\mathrm{mGy}$.

5.3.3 Scattering Detail at Higher Angles

Scattering into a peak at some distance from the center is a more realistic model for scattering from breast tissue than the broadening of the central peak as was seen in section 4.3. In a randomly oriented system a peak in the scattering profile corresponds to a ring in the 2-dimensional pattern. As an example we use a scattering pattern with $s_0 = 0.002\,\mathrm{nm}^{-1}$, and $\sigma_1 = 5{\cdot}10^{-5}\,\mathrm{nm}^{-1}$. The details have a 1–6% shift in the peak position as compared to the background. The value of s_0 corresponds to a periodic structure with 500 nm period length. This is somewhat larger than the sizes of the structures in the breast tissue samples (collagen packing ~ 100 nm), but is a compromise due to the increase in the simulation time with s_0.

Figure 5.15 shows the RCs for the background and the detail with 6% larger s_0. There is a clear difference in the RCs at the locations of the peaks, but at the center there are virtually no differences. The analysis should be based specifically on the quantification of the peak positions and shapes, and the RC should be recorded around these peaks. Recording the RC at other than the peak positions contributes mainly to the increase in dose, because

at these locations the RC is rather featureless. As was seen in section 5.3.1, the recording of the whole scattering pattern requires anyway a multitude of analyzer positions to be used, so that it is more useful to focus on some feature of the scattering pattern, which can be expected to change, rather than trying to record the whole scattering pattern.

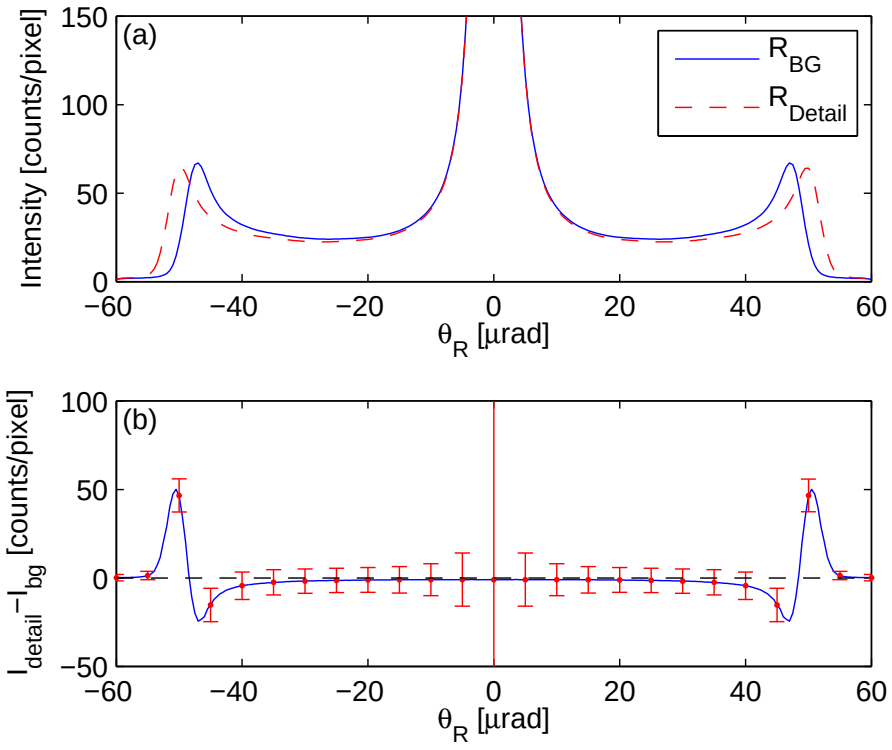

Figure 5.15: RCs for the background and the detail with a 6% larger s_0 (a), and their difference (b). The counts have been calculated allowing $D_{\mathrm{skin}} = 1\,\mathrm{mGy}$ for each rocking angle. The error bars show the variation due to photon statistics.

The peaks are asymmetric because the lateral integration contributes to the inside of the ring but not to the outside. To get the properties of the peak we fit to the recorded data the function

$$g(\theta) = \begin{cases} A\exp[-(\theta-\theta_0)^2/(2\sigma_2^2)] + B_1 & \theta < \theta_0, \\ A\exp[-(\theta-\theta_0)^2/(2\sigma_2^2)] + B_2 & \theta >= \theta_0. \end{cases} \tag{5.3}$$

Here θ_0 is the peak position, and σ_2 the peak width. The background values B_1 and B_2 are determined directly from the data so that the number of parameters to fit is 3 (σ_2, θ_0 and A). Because of the axial symmetry of the scattering pattern, the two peaks at either side of the direct beam are mirror

images of each other with respect to the central peak position, so that also the refraction angle can be determined through the positions of these two peaks.

Figure 5.16 shows how the details are visible. For the measurement of the peak positions rocking angles θ_{R} from -60 to -36 μrad and 36 to 60 μrad, with 1.5 μrad increments, were used. Dose $D_{\mathrm{skin}} = 1\,\mathrm{mGy}$ was given at each angle for a total of $D_{\mathrm{skin}} = 34\,\mathrm{mGy}$. Parameters σ_{MIR} and γ_{W} are also displayed, calculated for the same dose using the angular range from -20 to 20 μrad. It can be seen that σ_{MIR} and γ_{W} do not produce good contrast, but the peak position s_0 gives a reasonable SNR.

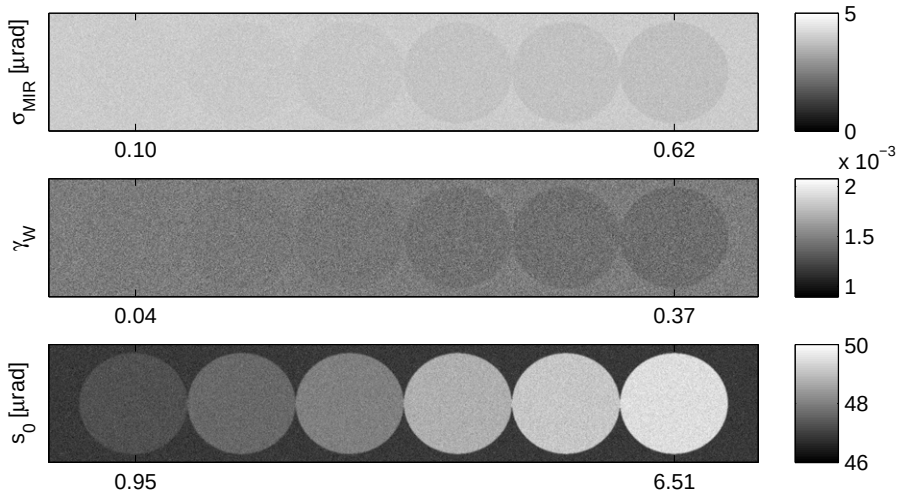

Figure 5.16: Images of the cylinder details with 10% scattering into a Gaussian ring. The ring peak in the details is at 1-6% larger s_0-values than in the background. The SNR values displayed on the horizontal axes are calculated for $D_{\mathrm{skin}} = 34\,\mathrm{mGy}$.

The extrapolation of SNR to other values of the scattering fraction and s_0 is shown in figure 5.17. The SNR is extrapolated based on its square being proportional to the number of recorded photons, $\mathrm{SNR} \sim \sqrt{N_{\mathrm{observed}}} \sim \sqrt{(1-\xi)}s_0^{-\frac{1}{4}}$. The factor $\sqrt{1-\xi}$ comes from the fact that the number of photons recorded is linearly proportional to the scattering fraction. The factor $s_0^{-\frac{1}{4}}$ comes from the fact that the fraction of the ring of scattering that is transmitted in an analyzer scan of constant length is proportional to $\sqrt{s_0}$. From the extrapolation we see that the SNR is reasonably good even at values of s_0 required for peaks from biological structures, such as the 3$^{\mathrm{rd}}$ peak from the axial periodicity of collagen structure at $s_0 \approx 0.046\,\mathrm{nm}^{-1}$. The SNR values were calculated for the case where the peak position in the detail is $\Delta s_0 = 1 \cdot 10^{-4}\,\mathrm{nm}^{-1}$ larger than in the background. At the

position of the 3rd collagen peak the relative shift in peak position ($\Delta s_0/s_0$) is about 0.26%. This is of the same order of magnitude as the difference that has been measured between healthy and malignant regions in breast tissue samples [4]. However, the fraction of scattering going to this peak in reality is rather low, and therefore it may not be well visible in practice.

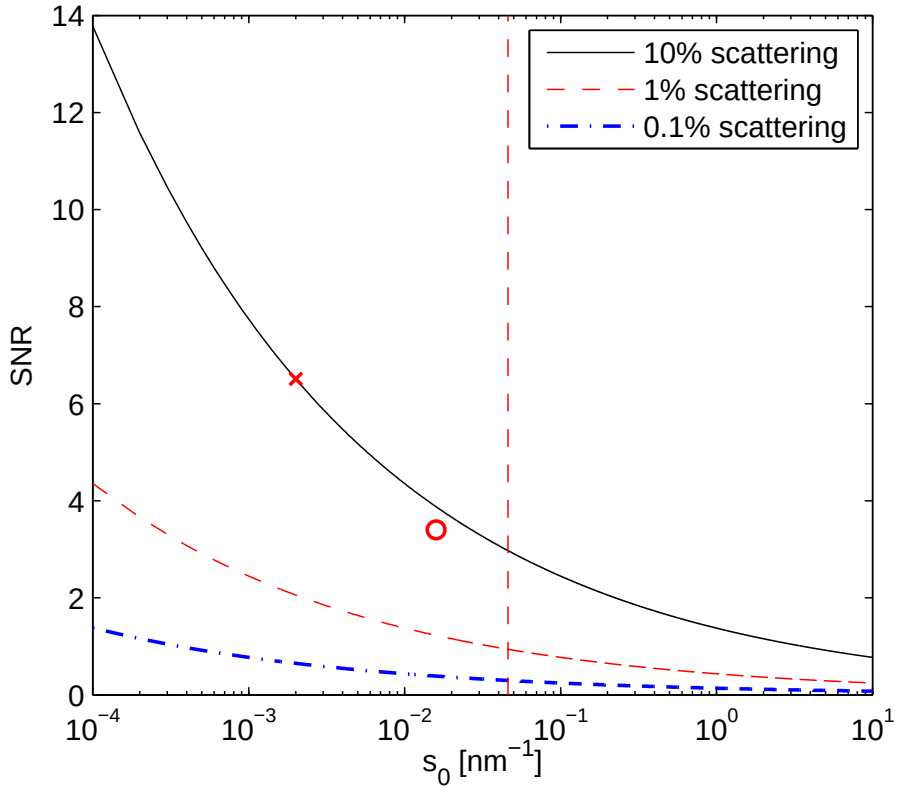

Figure 5.17: Extrapolated SNR for a scattering ring where the s_0 for the detail is $1 \cdot 10^{-4}\,\mathrm{nm}^{-1}$ larger than in the background. Skin dose is $D_{\mathrm{skin}} = 34\,\mathrm{mGy}$. The cross marks the point that was used as a basis for the extrapolation, and the ring marks another point that was calculated via the simulation. In the extrapolation the functional form of the SNR was assumed to be $\mathrm{SNR} \sim \sqrt{1-\xi}\, s_0^{-\frac{1}{4}}$. The dashed vertical line marks the position of the 3rd collagen peak.

The dose used in the calculation of the SNR curves in figure 5.17 was $D_{\mathrm{skin}} = 34\,\mathrm{mGy}$, and is rather large compared to the typical glandular dose of 2.6 mGy [141] in mammography. However, some other medical examinations, such as imaging of the spine, do involve doses that are comparable to 34 mGy [142]. Therefore in some cases the signal coming from structural changes can give a good SNR for an acceptable dose, and for strongly scat-

tering samples it may be worthwhile to use large analyzer angles, away from the direct beam, to observe this scattering.

5.3.4 Scattered Fraction

When $F(\theta_x, \theta_z)$ is essentially identical between the details and the background, or changes in a way that is not easily observable in the ABI measurements, the differences in the scattering fraction can still reveal details in the images due to scatter rejection. As seen in section 4.3 changes in breast tissue due to breast cancer cause clear changes in the scattering fractions, although there is some uncertainty in the absolute ratios due to the fact that the scattering could not be observed down to zero scattering angle.

To simulate the scatter rejection we use the phantom with spheres, and let the spheres and the background have identical densities ($\rho = 1.00\,\mathrm{g/cm^3}$). The scattering fraction for the background is 0.3% per mm (amounting to about 3% for the 10 mm thickness, with only negligible multiple scattering), and for the details 0.6% per mm. The scattering shape is Lorentzian with FWHM $= 10\,\mu\mathrm{rad}$. Figure 5.18 shows the images for $D_{\mathrm{skin}} = 10\,\mathrm{mGy}$. The details are clearly visible, and the attenuation image gives the best SNR. Even the smallest detail of 1 mm diameter can be distinguished from the images, although only barely. The σ_{MIR} and γ_{W} parameters show also rather good SNR, but this is because scattering was into rather small angles, rather than further away from the peak. This result indicates that typical differences in the scattering fraction for healthy and necrotic collagen are sufficiently large so that they can be observed in ABI imaging. However, it should be noted that changes in thickness and scatter fraction produce a similar effect, and cannot be distinguished from each other.

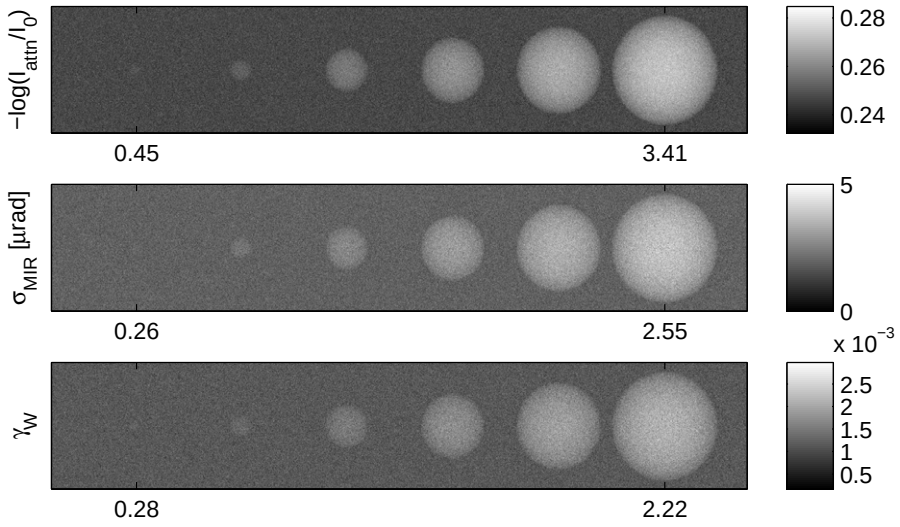

Figure 5.18: Image of the sphere details for varying scattering fraction (0.3% per mm for the background 0.6% per mm for the details). The absorption for the background and the details is identical. The diameters of the spheres are $1, 2, 4, 6, 8$ and 10 mm. The dose for the calculation of the images is $D_{\mathrm{skin}} = 10\,\mathrm{mGy}$.

Chapter 6

Conclusions and Discussion

We studied both the effect of scattering and refraction for tissue samples experimentally, and for phantoms experimentally and computationally. The computational studies were done in order to show how well scattering is visible in imaging situations, where the total dose to the sample is limited.

The measured scattering patterns from breast tissue samples show that there is only very little scattering in the forward direction, so that in the angular regime typically used in ABI (say $\pm 10\,\mu$rad) the scattering is barely visible. This is natural, as the structures producing scattering in this angular regime would be several micrometers in diameter, and the interaction would better be interpreted as refraction rather than scattering. The lack of central widening therefore indicates that the refracting structures in breast tissue samples are mostly larger than the spatial resolution, and refraction is seen as a spatial variation in the peak position of the RC rather than as a broadening of the RC.

For samples that do produce refractive broadening it has been shown that the angular regime of this broadening matches rather well the width of the analyzer RC [90]. Furthermore, refraction affects the whole portion of the beam, reducing the contribution of the direct, unaffected beam to almost zero. By observing the widening of the RC, it is possible to get a rather good contrast even when the changes in the refractive index are very small. If the contribution of the direct beam is considerable, then tuning the analyzer slightly away from the central peak can produce the best contrast by avoiding the direct beam, which dominates in the central region. This type of dark field imaging has been introduced in the form of W-DEI. For the determination of the image quality the important question is how much beyond the central peak should the images be taken. This depends largely on the shape of the scattering pattern, and therefore *a priori* knowledge of the scattering properties is essential in using W-DEI optimally.

There are several differences in the small-angle scattering patterns for healthy, malignant, and necrotic areas of the breast tissue samples, indicat-

ing structural changes in the macromolecular composition of the tissues [6]. Scattering fraction for benign and healthy tissues differed by a factor of two in the angular regime that was studied. This indicates that there are considerable changes in the structure, and the increase in intensity at larger angles can be attributed to breaking down of collagen chains [108]. The changes in scattering in the typical angular region used in ABI could not be quantified due to the low intensity of scattering in this region. The lateral integration of the scattering patterns in ABI transmits some of the intensity coming to larger angles even when the analyzer angle is 0. However, the main effect of this integration is to add a rather uniform background, and therefore the changes in the shape of the scattering patterns cannot be quantified to any degree based on ABI measurements in the very narrow region normally used.

The differences in the shape of the scattering patterns for the breast tissue samples are mainly in the position of the peak due to the axial periodicity of collagen, and in the visibility of the peak due to the cross section of the collagen fibrils. These indicate either well structured and rather uniform fibrils (healthy), disorganized and diverse fibrils (malignant), or the complete loss of fibrillar structure (necrotic). The changes in scattering are visible in the angular regime that is of the order of 1000 times larger than the angular acceptance of the analyzer crystal. To observe the complete scattering pattern in ABI would necessitate the use of at least hundreds of different analyzer positions. Because the angular position of the most interesting changes are known, it is possible to optimize the imaging so that the signal is recorded only at angular settings close to the most interesting regions. When measured in this way, we showed that a small change in the position of an isolated peak is visible in ABI for a reasonable dose of a few dozen mGy, even for quite small amounts of scattering.

Even when the changes in scattering pattern appear at large angles, the scattering fraction can be estimated based on ABI measurements near the central peak, i.e. using scatter rejection. The scattering patterns from different areas in the breast tissue samples contain significant changes in the scattering fraction, and therefore this serves as a useful source of contrast. The recording of the central peak can thus be considered an essential part of ABI imaging, because in addition to refraction it contains information also about the total amount of scattering.

The possibility for mapping the position of the collagen peak in ABI imaging for a reasonable dose makes it also worthwhile to consider whether the measurements could be done in CT mode to provide a three dimensional mapping of the peak position. Although in the clinical use of mammography the dose may then be prohibitively high considering the possible benefits, such experiments could be done for in vitro samples. This could offer a unique view on the morphology of the structural changes related to breast cancer, which might bring new light into how the cancer spreads.

Currently the limiting factor in ABI imaging is the intensity of the source, which makes *in vivo* imaging impractical. It seems however that from the point of view of imaging dose, at least some applications involving the analysis of scattered radiation could be used in a clinical setting as well. Especially the differences in scattering fraction may provide enough contrast with a reasonably low dose for structures whose densities are almost identical. As the compact x-ray sources improve, such methods might become available even at hospitals.

References

[1] M.O. Hasnah, Z. Zhong, O. Oltulu, E. Pisano, R.E. Johnston, D. Sayers, W. Thomlinson, and D. Chapman. Diffraction enhanced imaging contrast mechanisms in breast cancer specimens. *Med. Phys.*, 29:2216–2221, 2002.

[2] Miklos Z Kiss, Dale E Sayers, Zhong Zhong, Christopher Parham, and Etta D Pisano. Improved image contrast of calcifications in breast tissue specimens using diffraction enhanced imaging. *Physics in Medicine and Biology*, 49:3427–3439, 2004.

[3] Elodie Pagot, Stefan Fiedler, Peter Cloetens, Alberto Bravin, Paola Coan, Kamel Fezzaa, José Baruchel, and Jürgen Härtwig. Quantitative comparison between two phase contrast techniques: diffraction enhanced imaging and phase propagation imaging. *Physics in Medicine and Biology*, 50:709–724, 2005.

[4] Manuel Fernández, Jani Keyriläinen, Ritva Serimaa, Mika Torkkeli, Marja-Liisa Karjalainen-Lindsberg, Marjut Leidenius, Karl von Smitten, Mikko Tenhunen, Stefan Fiedler, Alberto Bravin, Thomas M Weiss, and Pekka Suortti. Human breast cancer in vitro: matching histo-pathology with small-angle x-ray scattering and diffraction enhanced x-ray imaging. *Physics in Medicine and Biology*, 50:2991–3006, 2005.

[5] Jani Keyriläinen. *Diffraction-Enhanced X-Ray Imaging Of In Vitro Breast Tumours*. PhD thesis, University of Helsinki, 2004.

[6] Manuel Fernández. *X-ray scattering and diffraction enhanced imaging studies of in vitro breast tissues*. PhD thesis, University of Helsinki, 2006.

[7] William R. Hendee. X rays in medicine. *Physics Today*, 48:51–56, 1995.

[8] G. N. Hounsfield. Computerized transverse axial scanning (tomography). 1. description of system. *Br J Radiol*, 46:1016–1022, 1973.

[9] Peter Toft. *The Radon Transform Theory and Implementation*. PhD thesis, Technical University of Denmark, 1996.

[10] Peter Herzog and Christina Rieger. Risk of cancer from diagnostic x-rays. *The Lancet*, 363:340–341, 2004.

[11] Charles A. Mistretta, Andrew B. Crummy, and Charles M. Strother. Digital angiography: A perspective. *Radiology*, 139:273–276, 1981.

[12] P Baldelli, A Bravin, C Di Maggio, G Gennaro, A Sarnelli, A Taibi, and M Gambaccini. Evaluation of the minimum iodine concentration for contrast-enhanced subtraction mammography. *Physics in Medicine and Biology*, 51:4233–4251, 2006.

[13] S Bayat, G Le Duc, L Porra, G Berruyer, C Nemoz, S Monfraix, S Fiedler, W Thomlinson, P Suortti, C G Standertskjöld-Nordenstam, and A R A Sovijärvi. Quantitative functional lung imaging with synchrotron radiation using inhaled xenon as contrast agent. *Physics in Medicine and Biology*, 46:3287–3299, 2001.

[14] H Suhonen, L Porra, S Bayat, A R A Sovijärvi, and P Suortti. Simultaneous in vivo synchrotron radiation computed tomography of regional ventilation and blood volume in rabbit lung using combined K-edge and temporal subtraction. *Phys. Med. Biol.*, 53:775–791, 2007.

[15] R.W. James. *The Optical Principles of Diffraction of X-Rays*. G. Bell and Sons Ltd, 1958.

[16] Arthur Compton. The spectrum of scattered x-rays. *Physical Review*, 22:409–413, 1923.

[17] B. Lengeler. Coherence in x-ray physics. *Naturwissenschaften*, 88:249–260, 2001.

[18] Max Born and Emil Wolf. *Principles of Optics*. Cambridge University Press, seventh edition, 1999.

[19] H. H. Hopkins. The concept of partial coherence in optics. *Proc. Roy. Soc. Lond. A*, 208:263–277, 1951.

[20] Friso van der Veen and Franz Pfeiffer. Coherent x-ray scattering. *Journal of Physics: Condensed Matter*, 16:5003–5030, 2004.

[21] M.J. Berger, J.H. Hubbell, S.M. Seltzer, J. Chang, J.S. Coursey, R. Sukumar, and D.S. Zucker. Xcom: Photon cross sections database. Technical report, National Institute of Standards and Technology (NIST), 1998. Available from: http://www.physics.nist.gov/PhysRefData/Xcom/Text/XCOM.html.

[22] J.H. Hubbell, Wm. J. Veigele, E.A. Briggs, R.T. Brown, D.T. Cromer, and R.J. Howertom. Atomic form factors, incoherent scattering functions, and photon scattering cross sections. *J. Phys. Chem. Ref. Data*, 4:471–538, 1975.

[23] Dale E. Sayers, Edward A. Stern, and Farrell W. Lytle. New technique for investigating noncrystalline structures: Fourier analysis of the extended x-ray–absorption fine structure. *Phys. Rev. Lett.*, 27:1204–1207, 1971.

[24] David H. Templeton. Anomalous scattering. In G.S. Brown and D.E. Moncton, editors, *Handbook on Synchrotron Radiation*, volume 3, pages 201–220. Elsevier Science Publishers B.V., 1991.

[25] H.B. Stuhrmann, G. Goerigk, and B. Munk. Anomalous x-ray scattering. In S. Ebashi, M. Koch, and E. Rubenstein, editors, *Handbook on Synchrotron Radiation*, volume 4, pages 555–580. Elsevier Science Publishers B.V., 1991.

[26] H Elleaume, S Fiedler, F Estéve, B Bertrand, A M Charvet, P Berkvens, G Berruyer, T Brochard, G Le Duc, C Nemoz, M Renier, P Suortti, W Thomlinson, and J F Le Bas. First human transvenous coronary angiography at the European Synchrotron Radiation Facility. *Physics in Medicine and Biology*, 45:L39–L43, 2000.

[27] Leif Gerward. X-ray attenuation coefficients: current state of knowledge and availability. *Radiation Physics and Chemistry*, 41:783–789, 1993.

[28] J. J. DeMarco and P. Suortti. Effect of scattering on the attenuation of x rays. *Physical Review B*, 4:1028–1033, 1971.

[29] J. H. Hubbell and S. M. Seltzer. Tables of x-ray mass attenuation coefficients and mass energy-absorption coefficients. Technical report, National Institute of Standards and Technology (NIST), 1996. Available from: http://physics.nist.gov/PhysRefData/XrayMassCoef.

[30] A. Guinier. *X-Ray Diffraction In Crystals, Imperfect Crystals, and Amorphous Bodies*. Dover Publications, Inc., 1994.

[31] D. C. Creagh. X-ray dispersion corrections. In A.J.C. Wilson and E. Prince, editors, *International Tables for Crystallography*, volume C, pages 242–258. Kluwer Academic Publishers, second edition, 1999.

[32] C. T. Chantler. Theoretical form factor, attenuation and scattering tabulation for Z=1-92 from E=1-10 eV to E = 0.4-1.0 MeV. *J. Phys. Chem. Ref. Data*, 24:71–643, 1995.

[33] A. H. Compton and S. K. Allison. *X-rays in theory and experiment*. D. van Nostrand Company, Inc., second edition, 1935.

[34] M. J. Cooper. Compton scattering and electron momentum determination. *Rep. Prog. Phys.*, 48:415–481, 1985.

[35] O. Klein and Y. Nishina. Über die streuung von strahlung durch freie elektronen nach der neuen relativistischen quantendynamik von Dirac. *Zeitschrift für Physik A Hadrons and Nuclei*, 52:853–868, 1929.

[36] W. Brefeld and B.Gürtler. Synchrotron radiation sources. In S. Ebashi, M. Koch, and E. Rubenstein, editors, *Handbook on Synchrotron Radiation*, volume 4. Elsevier Science Publishers B.V., 1991.

[37] S. Krinsky, M.L. Perlman, and R.E. Watson. Characteristics of synchrotron radiation and its sources. In Ernst-Eckhard Koch, editor, *Handbook on Synchrotron Radiation*, volume 1, pages 65–132. Elsevier Science Publishers B.V., 1983.

[38] Eric W. Weisstein. Modified bessel function of the second kind. From MathWorld–A Wolfram Web Resource. http://mathworld.wolfram.com/ModifiedBesselFunctionoftheSecondKind.html.

[39] H. Elleaume, A.M. Charvet, P. Berkvens, G. Berruyer, T. Brochard, Y. Dabin, M.C. Dominguez, A. Draperi, S. Fiedler, G. Goujon, G. Le Duc, M. Mattenet, C. Nemoz, M. Perez, M. Renier, C. Schulze, P. Spanne, P. Suortti, W. Thomlinson, F. Esteve, B. Bertrand, and J.F. Le Bas. Instrumentation of the ESRF medical imaging facility. *Nuclear Instruments & Methods in Physics Research A*, 428:513–527, 1999.

[40] F. Arfelli et al. Digital mammography with synchrotron radiation. *Review of Scientific Instruments*, 66:1325–1328, 1995.

[41] A. Abrami et al. Medical applications of synchrotron radiation at the SYRMEP beamline of ELETTRA. *Nuclear Instruments & Methods in Physics Research A*, 548:221–227, 2005.

[42] M. Ando et al. Clinical step onward with X-ray dark-field imaging and perspective view of medical applications of synchrotron radiation in Japan. *Nuclear Instruments & Methods in Physics Research A*, 548:1–16, 2005.

[43] H. E. Johns and J. R. Cunningham. *The Physics of Radiology*. Charles C. Thomas, fourth edition, 1983.

[44] O. Hemberg, M. Otendal, and H. M. Hertz. Liquid-metal-jet anode electron-impact x-ray source. *Applied Physics Letters*, 83:1483–1485, 2003.

[45] H. Yamada. Novel x-ray source based on a tabletop synchrotron and its unique features. *Nuclear Instruments & Methods in Physics Research B*, 199:509–516, 2003.

[46] Toru Hirai, Hironari Yamada, Makoto Sasaki, Daisuke Hasegawa, Masaki Morita, Yasuhito Oda, Jyunya Takaku, Takayasu Hanashima, Norihisa Nitta, Masashi Takahashi, and Kiyoshi Murata. Refraction contrast 11x-magnified x-ray imaging of large objects by MIRRORCLE-type table-top synchrotron. *Journal of Synchrotron Radiation*, 13:397–402, 2006.

[47] Frank E. Carroll. Tunable monochromatic x rays: A new paradigm in medicine. *American Journal of Roentgenology*, 179:583–590, 2002.

[48] Frank E. Carroll, Marcus H. Mendenhall, Robert H. Traeger, Charles Brau, and James W. Waters. Pulsed tunable monochromatic x-ray beams from a compact source: New opportunities. *American Journal of Roentgenology*, 181:1197–1202, 2003.

[49] B. Lengeler et al. A microscope for hard x rays based on parabolic compound refractive lenses. *Applied Physics Letters*, 74:3924–3926, 1999.

[50] T. Matsushita and H. Hashizume. X-ray monochromators. In Ernst-Eckhard Koch, editor, *Handbook on Synchrotron Radiation*, volume 1, pages 261–314. Elsevier Science Publishers B.V., 1983.

[51] B. E. Warren. *X-Ray Diffraction*. Addison-Wesley Publishing Company, 1969.

[52] André Authier. *Dynamical Theory of X-Ray Diffraction*. Oxford University Press, 2001.

[53] E. Erola, V. Eteläniemi, P. Suortti, P. Pattison, and W. Thomlinson. X-ray reflectivity of bent perfect crystals in Bragg and Laue geometry. *Journal of Applied Crystallography*, 1990.

[54] H Elleaume, A M Charvet, S Corde, F Estève, and J F Le Bas. Performance of computed tomography for contrast agent concentration measurements with monochromatic x-ray beams: comparison of K-edge versus temporal subtraction. *Physics in Medicine and Biology*, 47:3369–3385, 2002.

[55] B.W. Batterman and D.H. Bilderback. X-ray monochromators and mirrors. In G.S. Brown and D.E. Moncton, editors, *Handbook on Synchrotron Radiation*, volume 3. Elsevier Science Publishers B.V., 1991.

[56] M.B. Williams et al. Noise power spectra of images from digital mammography detectors. *Med. Phys.*, 26:1279–1293, 1999.

[57] Diego Pontoni, T. Narayanan, and Adrian R. Rennie. High-dynamic range SAXS data acquisition with an x-ray image intensifier. *Journal of Applied Crystallography*, 2002.

[58] A. Bravin, S. Fiedler, P. Coan, J.-C. Labiche, C. Ponchuta, A. Peterzolc, and W. Thomlinson. Comparison between a position sensitive germanium detector and a taper optics CCD "FRELON" camera for diffraction enhanced imaging. *Nuclear Instruments & Methods in Physics Research A*, 510:35–40, 2003.

[59] Paola Coan, Angela Peterzol, Stefan Fiedler, Cyril Ponchut amd Jean Claude Labiche, and Alberto Bravin. Evaluation of imaging performance of a taper optics CCD 'FReLoN' camera designed for medical imaging. *Journal of Synchrotron Radiation*, 2006.

[60] Paola Coan. *Development and Application of the Analyzer-Based Imaging technique with Hard Synchrotron Radiation.* PhD thesis, l'Universite Joseph Fourier, 2006.

[61] D Chapman, W Thomlinson, R E Johnston, D Washburn, E Pisano, N Gmür, Z Zhong, R Menk, F Arfelli, and D Sayers. Diffraction enhanced x-ray imaging. *Physics in Medicine and Biology*, 42:2015–2025, 1997.

[62] K M Pavlov, C M Kewish, J R Davis, and M J Morgan. A variant on the geometrical optics approximation in diffraction enhanced tomography. *Journal of Physics D: Applied Physics*, 34:A168–A172, 2001.

[63] Ya I Nesterets, T E Gureyev, D Paganin, K M Pavlov, and S W Wilkins. Quantitative diffraction-enhanced x-ray imaging of weak objects. *Journal of Physics D: Applied Physics*, 37:1262–1274, 2004.

[64] H. Zhang, D. Chapman, Z. Zhong, C. Parham, and M. Gupta. Crystal tilt error and its correction in diffraction enhanced imaging system. *Nuclear Instruments & Methods in Physics Research A*, 572:961–970, 2007.

[65] Zhi-Feng Huang, Ke-Jun Kang, Pei ping Zhu, Wan-Xia Huang, Qing-Xi Yuan, and Jun-Yue Wang. Strategy of extraction methods and reconstruction algorithms in computed tomography of diffraction enhanced imaging. *Physics in Medicine and Biology*, 52:1–12, 2007.

[66] Miles N Wernick, Oliver Wirjadi, Dean Chapman, Zhong Zhong, Nikolas P Galatsanos, Yongyi Yang, Jovan G Brankov, Oral Oltulu, Mark A Anastasio, and Carol Muehleman. Multiple-image radiography. *Physics in Medicine and Biology*, 48:3875–3895, 2003.

[67] Gocha Khelashvili, Jovan G Brankov, Dean Chapman, Mark A Anastasio, Yongyi Yang, Zhong Zhong, and Miles N Wernick. A physical model of multiple-image radiography. *Physics in Medicine and Biology*, 51:221–236, 2006.

[68] Carol Muehleman, Jun Li, Zhong Zhong, Jovan G. Brankov, and Miles N. Wernick. Multiple-image radiography for human soft tissue. *J. Anat.*, 208:115–124, 2006.

[69] Cheng-Ying Chou, Mark A Anastasio, Jovan G Brankov, Miles N Wernick, Eric M Brey, Dean M Connor Jr, and Zhong Zhong. An extended diffraction-enhanced imaging method for implementing multiple-image radiography. *Physics in Medicine and Biology*, 52:1923–1945, 2007.

[70] Glen Gowan. *Statistical Data Analysis*. Oxford University Press, 1998.

[71] T.M. Buzug, J. Weese, and K.C. Strasters. Motion detection and motion compensation for digital subtraction angiography image enhancement. *Philips J. Res.*, 51:203–229, 1998.

[72] Erik H.W. Meijering, Karel J. Zuiderveld, and Max A. Viergever. A fast technique for motion correction in DSA using a feature-based, irregular grid. In W.M. Wells, A. Colchester, and S. Delp, editors, *Lecture Notes in Computer Science*, volume 1496, pages 590–597, 1998.

[73] Erik H. W. Meijering, Wiro J. Niessen, and Max A. Viergever. Retrospective motion correction in digital subtraction angiography: A review. *IEEE Transactions on Medical Imaging*, 18:2–21, 1999.

[74] Sébastien Roux, Laurent Desbat, Anne Koenig, and Pierre Grangeat. Exact reconstruction in 2D dynamic CT: compensation of time-dependent affine deformations. *Physics in Medicine and Biology*, 49:2169–2182, 2004.

[75] Shinichiro Mori, Masahiro Endo, and Hiroshi Asakura. Improvement in banding artefacts in four-dimensional computed tomography for radiotherapy planning. *Physics in Medicine and Biology*, 51:5231–5244, 2006.

[76] Albert Rose. *Vision: Human and Electronic*. Plenum Press, 1973.

[77] L.A. Shepp and J.B. Kruskal. Computerized tomography: The new medical x-ray technology. *The American Mathematical Monthly*, 85:420–439, 1978.

[78] Anil K. Jain. *Fundamentals of Digital Image Processing.* Prentice Hall, 1989.

[79] Richard Gordon. A tutorial on ART (algebraic reconstruction techniques). *IEEE Transactions on Nuclear Science*, 21:78–93, 1974.

[80] A Filiz Baytaş and Melih Geçkinli. An alternative approach to direct Fourier reconstruction in parallel-beam tomography. *Meas. Sci. Technol.*, 7:556–563, 1996.

[81] Alexander H. Delaney. A fast and accurate fourier algorithm for iterative parallel-beam tomography. *IEEE Transactions on Image Processing*, 5:740–753, 1996.

[82] S. Iwasaki, S. Odanaka, Y. Shintoku, M. Kitamura, M. Haruyama, M. Takase, and K. Ara. New CT image reconstruction algorithm based on the bayes estimation. *Nuclear Instruments & Methods in Physics Research A*, 422:683–687, 1999.

[83] Yair Censor, Dan Gordon, and Rachel Gordon. BICAV: A block-iterative parallel algorithm for sparse systems with pixel-related weighting. *IEEE Transactions on Medical Imaging*, 20:1050–1060, 2001.

[84] S Siltanen, V Kolehmainen, S Järvenpaa, J P Kaipio, P Koistinen, M Lassas, J Pirttilä, and E Somersalo. Statistical inversion for medical x-ray tomography with few radiographs: I. general theory. *Physics in Medicine and Biology*, 48:1437–1463, 2003.

[85] U. Bonse and M. Hart. Small angle x-ray scattering by spherical particles of polystyrene and polyvinyltoluene. *Zeitschrift für Physik*, 189:151–162, 1966.

[86] Jovan G. Brankov, Alejandro Sáiz-Herranz, and Miles N. Wernick. Noise analysis for diffraction enhanced imaging. In *Proceedings of the 2004 IEEE International Symposium on Biomedical Imaging: From Nano to Macro*, pages 1428–1431, 2004.

[87] Luigi Rigon, Hans-Juergen Besch, Fulvia Arfelli, Ralf-Hendrik Menk, Gabriele Heitner, and Hartmute Plothow-Besch. A new DEI algorithm capable of investigating sub-pixel structures. *Journal of Physics D: Applied Physics*, 36:A107–A112, 2003.

[88] Luigi Rigon, Fulvia Arfelli, and Ralf-Hendrik Menk. Three-image diffraction enhanced imaging algorithm to extract absorption, refraction, and ultrasmall-angle scattering. *Applied Physics Letters*, 90:113102–113104, 2007.

[89] E. Pagot, P. Cloetens, S. Fiedler, A. Bravin, P. Coan, J. Baruchel, J. Hartwig, and W. Thomlinson. A method to extract quantitative information in analyzer-based x-ray phase contrast imaging. *Applied Physics Letters*, 82:3421–3423, 2003.

[90] H Suhonen, M Fernández, A Bravin, J Keyriläinen, and P Suortti. Refraction and scattering of x-rays in analyzer-based imaging. *Journal of Synchrotron Radiation*, 14:512–521, 2007.

[91] U Kleuker, P Suortti, W Weyrich, and P Spanne. Feasibility study of x-ray diffraction computed tomography for medical imaging. *Physics in Medicine and Biology*, 43:2911–2923, 1998.

[92] John M. Stone. *Radiation and Optics*. McGraw-Hill Book Company, Inc., 1963.

[93] Jan Skov Pedersen. Analysis of small-angle scattering data from colloids and polymer solutions: modeling and least-squares fitting. *Advances in Colloid and Interface Science*, 70:171–210, 1997.

[94] Qun Shen, Ivan Bazarovc, and Pierre Thibault. Diffractive imaging of nonperiodic materials with future coherent x-ray sources. *Journal of Synchrotron Radiation*, 11:432–438, 2004.

[95] J. M. Rodenburg, A. C. Hurst, A. G. Cullis, B. R. Dobson, F. Pfeiffer, O. Bunk, C. David, K. Jefimovs, and I. Johnson. Hard-x-ray lensless imaging of extended objects. *Physical Review Letters*, 98:034801(4), 2007.

[96] K. J. Gaffney and H. N. Chapman. Imaging atomic structure and dynamics with ultrafast x-ray scattering. *Science*, 316:1444–1448, 2007.

[97] George B. Arfken and Hans J. Weber. *Mathematical Methods for Physicists*. Academic Press, fourth edition, 1995.

[98] H.H. Hopkins. On the diffraction theory of optical images. *Proc. Roy. Soc. Lond. A*, 217:408–432, 1953.

[99] H.H. Hopkins. Applications of coherence theory in microscopy and interferometry. *J. Opt. Soc. Am.*, 47:508–526, 1957.

[100] P. Debye. Zerstreuung von röntgenstrahlen. *Ann. Phys.*, 351:809–823, 1915.

[101] O. Glatter and O. Kratky, editors. *Small Angle X-ray Scattering*. Academic Press, 1982.

[102] Emmanuel Pantos, Harold F. van Garderen, Peter A.J. Hilbers, Theo P.M. Beelen, and Rutger A. van Santen. Simulation of small-angle scattering from large assemblies of multi-type scatterer particles. *Journal of Molecular Structure*, 383:303–308, 1996.

[103] Gerald Oster and D. P. Riley. Scattering from cylindrically symmetric systems. *Acta Cryst.*, 5:272–276, 1952.

[104] Akira Ishimaru. *Wave Propagation and Scattering in Random Media: Multiple Scattering, Turbulence, Rough Surfaces and Remote Sensing*, volume 2. Academic Press, 1978.

[105] George H. Vineyard. Geometrical optics and the theory of multiple small angle scattering. *Physical Review*, 85:633–636, 1952.

[106] Eric W. Weisstein. Rayleigh distribution. Mathworld – A Wolfram Web Resource.

[107] Eckhard Limpert, Werner A. Stahel, and Markus Abbt. Log-normal distributions across the sciences: Keys and clues. *BioScience*, 51:341–352, 2001.

[108] Heikki Suhonen, Manuel Fernández, Ritva Serimaa, and Pekka Suortti. Simulation of small-angle x-ray scattering from collagen fibrils and comparison with experimental patterns. *Physics in Medicine and Biology*, 50:5401–5416, 2005.

[109] R. A. Lewis, K. D. Rogers, C. J. Hall, E. Towns-Andrews, S. Slawson, A. Evans, S. E. Pinder, I. O. Ellis, C. R. M. Boggis, A. P. Hufton, and D. R. Dance. Breast cancer diagnosis using scattered x-rays. *Journal of Synchrotron Radiation*, 7:348–352, 2000.

[110] M E Poletti, O D Goncalves, and I Mazzaro. X-ray scattering from human breast tissues and breast-equivalent materials. *Physics in Medicine and Biology*, 47:47–63, 2002.

[111] G Falzon, S Pearson, R Murison, C Hall, K Siu, A Evans, K Rogers, and R Lewis. Wavelet-based feature extraction applied to small-angle x-ray scattering patterns from breast tissue: a tool for differentiating between tissue types. *Physics in Medicine and Biology*, 51:2465–2477, 2006.

[112] Elaine A Ryan and Michael J Farquharson. Breast tissue classification using x-ray scattering measurements and multivariate data analysis. *Physics in Medicine and Biology*, 52:6679–6696, 2007.

[113] J A Griffiths, G J Royle, A M Hanby, J A Horrocks, S E Bohndiek, and R D Speller. Correlation of energy dispersive diffraction signatures

and microCT of small breast tissue samples with pathological analysis. *Physics in Medicine and Biology*, 52:6151–6164, 2007.

[114] T Narayanan, O. Diat, and B. Bösecke. SAXS and USAXS on the high briliance beamline at the ESRF. *Nuclear Instruments & Methods in Physics Research A*, 467–468:1005–1009, 2001.

[115] M. Fernańdez, J. Keyriläinen, M.-L. Karjalainen-Lindsberg, M. Leidenius, K. von Smitten, S. Fiedler, and P. Suortti. Human breast tissue characterisatiton with small-angle X-ray scattering. *Spectroscopy*, 18:167–176, 2004.

[116] M Fernández, J Keyriläinen, R Serimaa, M Torkkeli, M-L Karjalainen-Lindsberg, M Tenhunen, W Thomlinson, V Urban, and P Suortti. Small-angle x-ray scattering studies of human breast tissue samples. *Physics in Medicine and Biology*, 47:577–592, 2002.

[117] Miklos Z Kiss, Dale E Sayers, and Zhong Zhong. Measurement of image contrast using diffraction enhanced imaging. *Physics in Medicine and Biology*, 48:325–340, 2003.

[118] K M Pavlov, T E Gureyev, D Paganin, Ya I Nesterets, M J Morgan, and R A Lewis. Linear systems with slowly varying transfer functions and their application to x-ray phase-contrast imaging. *Journal of Physics D: Applied Physics*, 37:2746–2750, 2004.

[119] K.M. Pavlov, T.E. Gureyev, D. Paganin, Y.I. Nesterets, M.J. Kitchen, K.K.W. Siu, J.E. Gillam, K. Uesugi, N. Yagi, M.J. Morgan, and R.A. Lewis. Unification of analyser-based and propagation-based x-ray phase-contrast imaging. *Nuclear Instruments & Methods in Physics Research A*, 548:163–168, 2005.

[120] A. Bravin, V. Mocella, P. Coan, A. Astolfo, and C. Ferrero. A numerical wave-optical approach for the simulation of analyzer-based x-ray imaging. *Optics Express*, 15:5641–5648, 2007.

[121] Ya. I. Nesterets, P. Coan, T. E. Gureyev, A. Bravin, P. Cloetens, and S. W. Wilkins. On qualitative and quantitative analysis in analyser-based imaging. *Acta Cryst.*, A62:296–308, 2006.

[122] Michael Sandborg, Graham McVey, David R. Dance, and Gudrun Alm Carlsson. Schemes for the optimization of chest radiography using a computer model of the patient and x-ray imaging system. *Med. Phys.*, 28:2007–2019, 2001.

[123] D. Lazos, K. Bliznakova, Z. Kolitsi, and N. Pallikarakis. An integrated research tool for x-ray imaging simulation. *Computer Methods and Programs in Biomedicine*, 70:241–251, 2003.

[124] I-Y Son, M Winslow, B Yazici, and X G Xu. X-ray imaging optimization using virtual phantoms and computerized observer modelling. *Physics in Medicine and Biology*, 51:4289–4310, 2006.

[125] Gustaf Ullman, Michael Sandborg, David R Dance, Roger A Hunt, and Gudrun Alm Carlsson. Towards optimization in digital chest radiography using Monte Carlo modelling. *Physics in Medicine and Biology*, 51:2729–2743, 2006.

[126] A. Tartari, C. Bonifazzi, J.E. Fernandez, M. Bastiano, E. Casnati, C. Baraldi, and G. Di Domenico. Molecular coherent scattering data for tissue in photon transport Monte Carlo codes. *Applied Radiation and Isotopes*, 53:901–906, 2000.

[127] A. Tartari, C. Baraldi, and C Bonifazzi. A model for Monte Carlo simulation of low angle photon scattering in biological tissues. *Radiation Physics and Chemistry*, 61:631–632, 2001.

[128] Oral Oltulu, Zhong Zhong, Moumen Hasnah, Miles N Wernick, and Dean Chapman. Extraction of extinction, refraction and absorption properties in diffraction enhanced imaging. *Journal of Physics D: Applied Physics*, 36:2152–2156, 2003.

[129] Alan Watt. *3D Computer Graphics*. Addison-Wesley, third edition, 2000.

[130] Marcelo Gonçalves Hönnicke, Luigi Rigon, Ralf-H. Menk, and Cesar Cusatis. Quantitative and qualitative studies on high- contrast x-ray radiography with an asymmetrical crystal set-up at Elettra. *Journal of Synchrotron Radiation*, 12:701–706, 2004.

[131] Yu Zou, Xiaochuan Pan, and Emil Y Sidky. Image reconstruction in regions-of-interest from truncated projections in a reduced fan-beam scan. *Physics in Medicine and Biology*, 50:13–27, 2005.

[132] G Jarry, J J DeMarco, U Beifuss, C H Cagnon, and M F McNitt-Gray. A Monte Carlo-based method to estimate radiation dose from spiral CT: from phantom testing to patient-specific models. *Physics in Medicine and Biology*, 48:2645–2663, 2003.

[133] Nan Guang Chen and Jing Bai. Estimation of quasi-straightforward propagating light in tissues. *Physics in Medicine and Biology*, 44:1669–1676, 1999.

[134] M. N. Cinti, R. Pellegrini R. Pani and, F. Garibaldi, M. Betti, N. Lanconelli, A. Riccardi, R. Campanini, G. Zavattini, G. Di Domenico, A. Del Guerra, N. Belcari, W. Bencivelli, A. Motta, A. Vaiano, and

I. N. Weinberg. Custom breast phantom for an accurate tumor SNR analysis. *IEEE Transactions on Nuclear Science*, 51:198–204, 2004.

[135] B Grosswendt. Dependence of the photon backscatter factor for water on source-to-phantom distance and irradiation field size. *Physics in Medicine and Biology*, 35:1233–1245, 1990.

[136] E.A. Siegbahn, E. Bräuer-Krisch, J. Stepanek, H. Blattmann, J.A. Laissue, and A. Bravin. Dosimetric studies of microbeam radiation therapy (MRT) with Monte Carlo simulations. *Nuclear Instruments & Methods in Physics Research A*, 548:54–58, 2005.

[137] Paola Coan, Elodie Pagot, Stefan Fiedler, Peter Cloetens, Jose Baruchel, and Alberto Bravin. Phase-contrast x-ray imaging combining free space propagation and Bragg diffraction. *Journal of Synchrotron Radiation*, 12:241–245, 2005.

[138] R. Foster, J. Worden, M. Costanza, and L. Solomon. Clinical breast examination and breast self-examination. *Cancer*, 69:S1992–S1998, 1992.

[139] F. Pfeiffer, M. Bech, O. Bunk, P. Kraft, E.F. Eikenberry, Ch. Nrönnimann, C. Grünzweig, and C. David. Hard-x-ray dark-field imaging using a grating interferometer. *Nature Materials*, 2008.

[140] L. A. Feigin and D. I. Svergun. *Structure Analysis by Small-Angle X-Ray and Neutron Scattering*. Plenum Press, 1987.

[141] Randell L. Kruger and Beth A. Schueler. A survey of clinical factors and patient dose in mammography. *Med. Phys.*, 28:1449–1454, 2001.

[142] D. Hart, M.C. Hillier, and B.F. Wall. Doses to patients from radiographic and fluoroscopic x-ray imaging procedures in the UK - 2005 review. Technical report, Health Protection Agency, 2007.